UNIVERSITAT POLITÈCNICA DE VALÈNCIA

ESCUELA TÉCNICA SUPERIOR DE INGENIERÍA DEL DISEÑO

DEPARTAMENTO DE MÁQUINAS Y MOTORES TÉRMICOS

MASTER THESIS:

"SPARK IGNITION ENGINE MODELLING FOR CONTROL PURPOSES"

Author: **José Israel Sánchez García**

Director: **Benjamín Plá Moreno**

Valencia, September 2019

Abstract

Spark ignited (SI) engines are becoming a significant part of the global market of the automotive sector as Diesel engines are being restricted by new restringent legislations. One of the main drawbacks of this type of combustion, i.e. SI, is the cycle-to-cycle variability, which lowers the combustion efficiency and restricts the maximum spark advance due to knock limitations. Cycle-to-cycle dispersion is caused by unobservable phenomena at the ignition, such as initial kernel size or turbulence around the spark and is a topic of interest in engine modelling research.

The work presented in this project aims to develop a control-oriented model which is able to reproduce, not only the average combustion development, but also the cycle-to-cycle variability. The combustion model has been designed by adapting previously published models based on the entrained fuel mass on during the flame propagation. The main calibration constants have been identified and look-up tables have been implemented to improve the precision of the model. The cycle-to-cycle dispersion has been reproduced by assuming an initial probability distribution on the laminar speed and turbulence, which is propagated during the combustion development.

Experimental tests have been collected in an state of the art commercial engine. A training and a validation dataset with variations of the main actuators, namely the spark advance, the intake pressure, and the engine speed, have been used. Results shown the capability of the model to characterise with precision the combustion evolution and to reproduce the expected cycle-to-cycle variability.

I

Contents

List of Figures

List of Tables

X

1 Introduction

1.1 Preamble

Ignited combustion engines (IC engines) play today an important role in transport, regardless terrestrial, maritime or aerial applications. There are two main groups of IC engines depending on how combustion occurs: spark ignition engines (SI engines) where combustion is caused by a spark, and compression ignition engines (CI engines) if combustion is caused by high in-cylinder pressures.

Throughout a century of research in IC engines, many technology developments have taken place. Some of them, due to their nature, have been exclusive to a specific family of engines, while others have been applied indistinctly to both. Among the new technologies employed, we can highlight supercharging, electronic control, the increasing of the number of valves, the improvement of manufacturing systems and materials, and the incessant boom of new developments for the control of polluting emissions. From the beginning of IC engine history, all these advances have happened through research and testing. In this context, engine system modelling made appearance as a key tool for researchers in order to simplify, understand and emulate engine physic phenomena.

Nowadays, the advantages of modelling are well known, independently of the system that it is being modelled. A proper model can be useful to evaluate different design options, analyse physic phenomena, identify parameters for control purposes, study tendencies, predict engine systems performance and limitations or analyse output variables sensibilities.

Research on the engine combustion process is a good example of the usage of these models. From the fast and simple zero-dimensional combustion models to the current and complex chemical models or fluid dynamic ones, there exist in between a wide range of models. These models depend on aspects such as the space resolution, the physic phenomena taken into account or the hypothesis made to simplify the problem.

FIGURE 1: CMT Building at the UPV Campus.

This master thesis is focused on the modelling of the combustion process, more concretely on the SI engines combustion through a quasi-dimensional physic based model. The thesis has been made in the research and educational center CMT – Motores Térmicos belonging to the Polytechnic University of Valencia. Figure 1 shows the departmental building in which the whole project has been developed.

1.2   Motivation

SI engine combustion models are a fundamental part of the engine design process since they allow to make an initial, fast and cost-efficient parametric study to approach an optimum design. Besides, once the geometrical engine design is complete, combustion models are very useful to predict engine combustion performance and parameters that are difficult to measure. Therefore, they are also used for optimizing and tuning the combustion process.

However, these models usually have sub-models which include some constants that need to be fitted and calibrated from engine tests. Thus, it is necessary to obtain some experimental data from a test bench in order to adjust and later validate the model.

An important characteristic of SI engine combustion is the cycle-to-cycle dispersion. This is an undesirable phenomenon whereby combustion does not happen in the same way despite of maintaining the input parameters. From the stability point of view, it is recommended to move away from operation points where this variability is higher. This variability introduces greater irregularities both in the engine power and in the polluting emissions, affecting negatively the engine performance and vehicle comfort. This phenomenon has been analysed from a large set of experimental data in order to be included in the model.

In view of the reasons mentioned above, combustion modelling has become a key tool for engine design and control. Therefore, a proper model calibration is required to carry out this task. This is the framework where this master thesis belongs.

1.3   Background

CMT – Motores Térmicos has tested and worked previously with both diesel and gasoline engines. However, the implementation of the new European emission standard for diesel vehicles (EURO VI) has introduced higher limitations in polluting emissions and has added more severe restrictions at the municipal and regional level. This has caused a complicated scenario for these vehicles and a consequent drop in the use of diesel engines.

For this reason, in recent years the research line focused in gasoline engines has been enhanced. One of the drawbacks of these engines, in comparison with the diesel ones, is their low efficiency. This value varies in a Diesel cycle between 30-45% while in a gasoline engine cycle (Otto cycle) this value stays between 20-30%.

Cycle-to-cycle dispersion is an undesired stochastic characteristic of the gasoline engine that damages this efficiency. Its behaviour has been studied and modelled before with more or less success.

Now that gasoline engines are rising in detriment of diesel ones, it is interesting to focus the research on the study and improvement of dispersion for combustion control.

1.4 Objectives

This project aims to analyse and model the combustion process of a SI engine for control purposes. This main objective can be split into several more specific ones:

- Combustion analysis for mean value from experimental data obtained at the test bench. This objective is the first step of the project, where information from the engine is extracted and analysed for its use in followings steps.

- Combustion model development in a reasonable operation range. With the previous data analysis, a quasi-stationary two-zone physic-based turbulent entrainment combustion model is developed, calibrated and validated. Both the mean value of the in-cylinder pressure evolution and the mass fraction burned at each operation point are estimated without a piezoresistive sensor inside the combustion chamber.

- Combustion dispersion study for a representative number of cycles at each operation point. At this point, all the data extracted is analysed individually, focusing on the dispersion found for each operation point.

- Combustion dispersion model development to complement the previous combustion model. A dispersion model is calibrated with the data previously analysed and it is developed by means of statistical tools.

2 Combustion Modelling in SI Gasoline Engines

2.1 Combustion in SI Gasoline Engines

In traditional gasoline engines, a process of **premixed combustion** is produced. It starts with an homogeneous mixture of fuel and air. Both the mixing and combustion processes are enough separated in time to assure homogeneity.

SI Gasoline Engines are **provoked ignited engines** in which an electric arc, produced by a sparkplug, initiates the combustion process by means of a local input of energy. After this, the combustion process is developed supported by a flame front whose propagation transforms non-burned products into burned ones. This is an exothermic reaction at a speed of the order of the lineal mean piston velocity. This speed is very low compared with that of the sound, so the combustion in these engines is a deflagration. Depending on the Reynolds number of the flow, the combustion process can be developed in laminar or turbulent conditions.

In a **laminar premixed combustion** three different zones are defined inside the cylinder: **preheating zone, reaction zone and recombination zone**. In the first one, the air-fuel mixture raises its temperature due to mass and thermal diffusion from the flame front. Then, chemical activity began to occur but, from the energetic point of view, this is not very relevant. In the reaction zone, the conversion to the finals products takes place. Finally, at the end of the zone the burned product temperature is reached. This temperature will match the adiabatic flame temperature if heat losses through the walls were negligible or zero. The recombination zone is not significant either from the energetic point of view. Here, the composition of the gases may change either if thermodynamic conditions vary or if the reaction is controlled by kinetics.
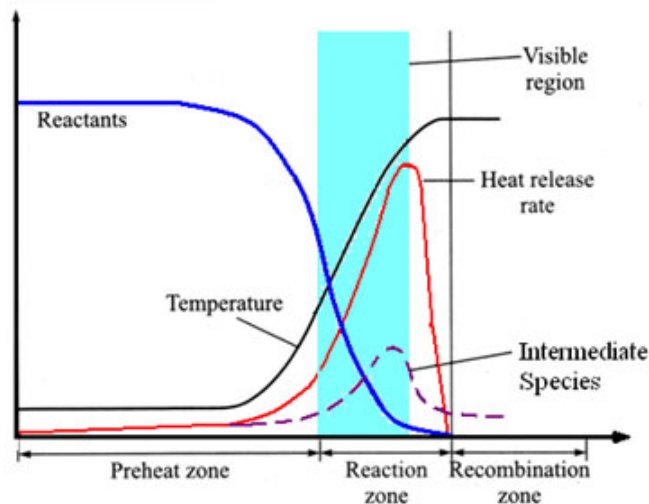
FIGURE 2: Laminar premixed combustion diagram [1].

In a **turbulent premixed combustion**, mass and thermal diffusion phenomena are faster. Attending to the turbulence intensity and to its spatial scale, two different situations must be taken into account. The first one is the **distributed flame**, when there is a high turbulent intensity (I) as well as the turbulent spatial integrate scale (L_{Int}) is of the same

magnitude order of the flame front thickness (δ). This one does not distort with respect to the laminar case, but the combustion velocity is higher. The other one is the **distorted flame**, when the turbulence intensity (I) is small and the turbulent spatial integrate scale (L_{Int}) is higher than the flame front thickness (δ). The flame distorts inducing a raising of the effective flame front area and, therefore, the diffusion phenomena [1].
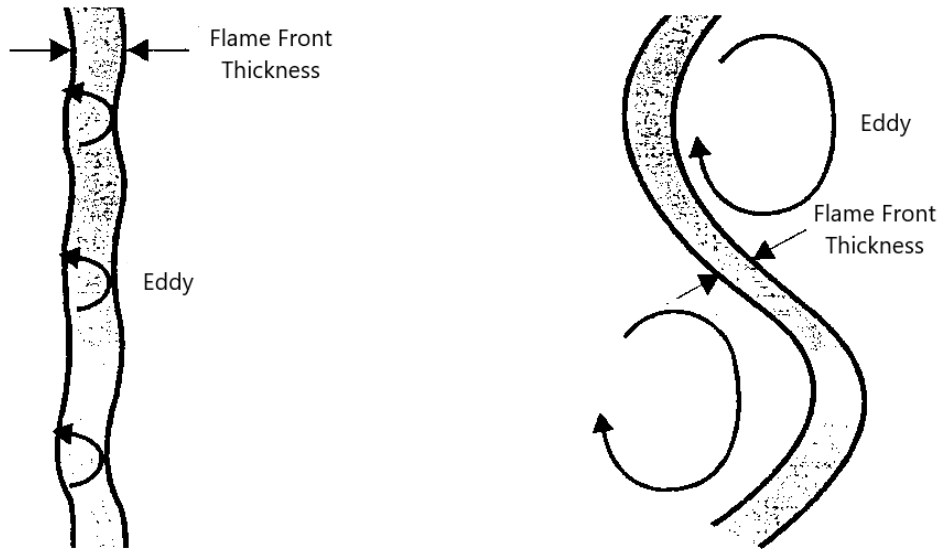
FIGURE 3: Distributed and distorted flame front thickness [1].

2.2   Regular Gasoline Combustion Process Analysis

An interesting parameter from the control point of view is the instant burned mass fraction along each cycle. This magnitude is proportional to the instant heat released. However, a direct measure of these parameters is not possible so they must be indirectly obtained from other measurable parameters.

Temperature and **pressure** are the two intensive magnitudes that characterise the working fluid state inside the cylinder. Only the second one can be assumed as an uniform parameter along the combustion chamber and, as a result, it can be **more easily measured**.

Once these experimental data have been obtained, both by applying the energy conservation principle and by quantifying the wall heat losses, we get the total amount of heat released in the combustion chamber. The heat released comes from the combustion of the fuel, thus, by knowing the calorific value of the fuel, the **instant burned mass can be calculated**. This methodology has been used for this project in order to analyse the combustion process. This is developed in Chapter 4 together with the equations and the hypothesis made to simplify the calculations.

In a **regular combustion process**, the ignition must be originated by an external agent, typically a spark from a sparkplug. The fuel must be resistant to auto-inflammation for avoiding spontaneous ignition of the mixture during combustion. **Three stages** can be differentiated. In the first one, the burned volume generated by the electric spark starts
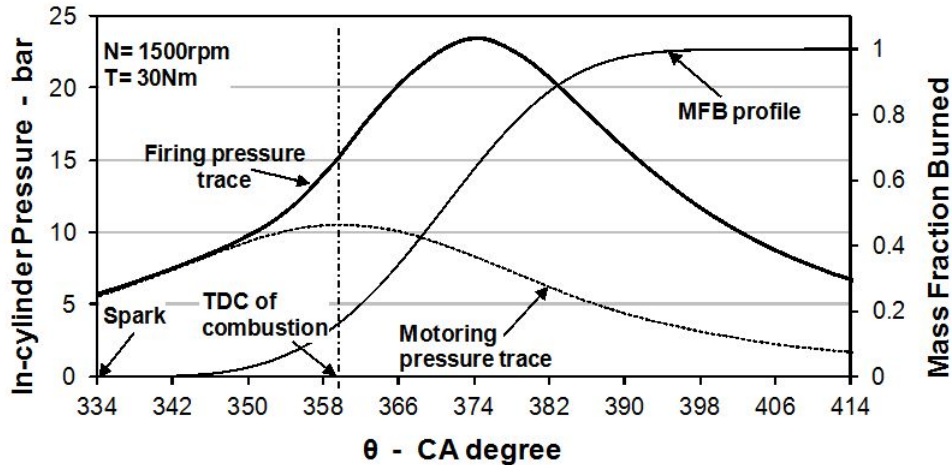
FIGURE 4: In-cylinder pressure and mass fraction burned profiles [1].

spreading slowly through the non-burned mass and its effect begins to be perceived in the combustion chamber pressure. This stage constitutes around 10% of the total combustion. At this point, a second stage is initiated. The combustion in this stage is faster than in the first one due to aspects such as a larger flame front area, higher unburned mass temperature and higher combustion velocity. Furthermore, pressure increases noticeably and the majority of the mixture is burned (usually the 85% of the combustion). Finally, once the flame front approaches to the combustion chamber wall, its propagation slows down initiating the last stage that ends when all the mass is burned.
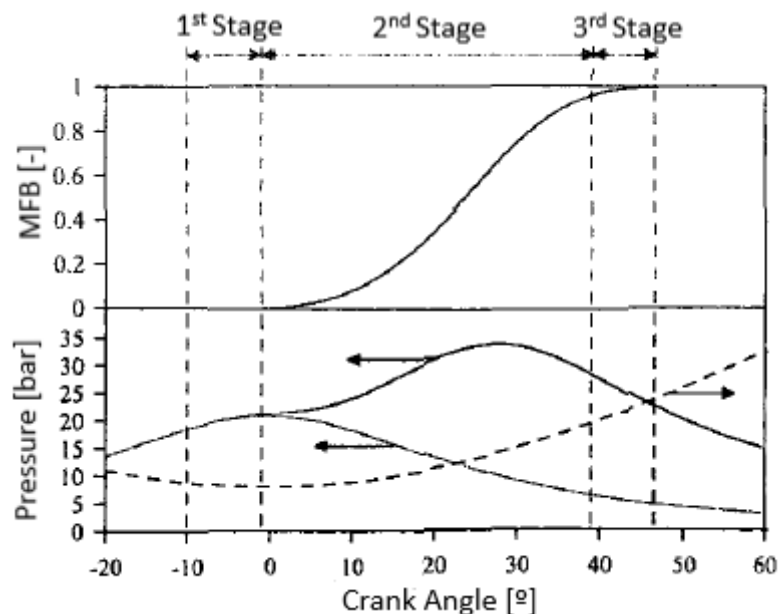
FIGURE 5: Combustion stages [1].

The propagation of the flame front can be explained in terms of three factors: the laminar combustion velocity (or **laminar flame speed**), the turbulent combustion velocity (or **turbulence intensity**) and **the drag flame front speed in enclosed spaces**.

In laminar conditions (low turbulence and zero or small mixture velocity), the flame front spreads to the fresh mixture and its temperature diffuses, raising the reaction velocity. **For a given fuel (gasoline in this case), two main parameters** affect the laminar combustion velocity (S_l): **pressure (p) and temperature (T)**. As pressure increases, velocity decreases. Besides, temperature is important since it directly affects both the reaction and the diffusion characteristics. While the unburned gas temperature mainly depends on the intake temperature, the burned gas temperature depends on several factors. Among these factors, it can be highlighted the initial temperature, the residual gas fraction (RGF), the humidity and the air-to-fuel ratio (λ).

An experimental correlation was made taking into account the influence of both parameters shown in Equation 1. For the case of gasoline as fuel, the values of the constants can be found in Table 1:

$$S_l = S_{l_0} \cdot \left(\frac{T}{T_0}\right)^\alpha \cdot \left(\frac{p}{p_0}\right)^\beta \tag{1}$$

$$S_{l_0} = B_m + B_\lambda \cdot (\lambda - \lambda_m)^2$$

Fuel	$\boldsymbol{\lambda_m}$ [-]	$\boldsymbol{B_m}$ [$\frac{cm}{s}$]	$\boldsymbol{B_\lambda}$ [$\frac{cm}{s}$]	$\boldsymbol{\alpha}$ [-]	$\boldsymbol{\beta}$ [-]
Gasoline	1.21	30.5	-54.9	$2.4 - 0.271 \cdot \lambda^{3.51}$	$-0.357 + 0.14 \cdot \lambda^{2.77}$

TABLE 1: Gasoline parameter values for laminar combustion velocity experimental correlation [1].

In SI engines the flow is clearly turbulent, increasing significantly the propagation velocity of the flame front. It has traditionally been quantified as the ratio between the turbulent combustion velocity (u_{CT}) and the laminar one (S_l), a magnitude called flame speed ratio (FSR). The **main parameters** that characterize the turbulent flow are: turbulence intensity (u'), spatial (L_{Int}) and temporal (τ_{Int}) integral scales. The two latter represent the characteristic time and size of the biggest eddies, and the spatial (λ_K) and temporal (τ_K) Kolmogorov scales represent the characteristic time and size of the smallest eddies where turbulence is dissipated.

During combustion, there is an interaction between turbulence and combustion themselves. This interaction will be different depending on the characteristic time and size of the turbulence with respect to both the flame front thickness and the characteristic reaction time (τ_R), respectively. Two dimensionless numbers are used to study this phenomenon. On the one hand, the Damköhler number (Da) or ratio between the temporal integral scale and the characteristic reaction time (Equation 2). On the other hand, the Karlovitz number (Ka) or ratio between the characteristic reaction time and the temporal Kolmogorov scale (Equation 3).

$$\text{Da} = \frac{\tau_{Int}}{\tau_R} = \frac{L_{Int}/u'}{\delta/S_l} \tag{2}$$

$$\text{Ka} = \frac{\tau_R}{\tau_K} = \frac{\delta/S_l}{\lambda_K/u'} \tag{3}$$

Comparing the characteristic size and time of both the turbulence and the reaction, different scenarios can be set in which the turbulent combustion is developed. This is represented in Figure 6. Typically, **SI engines operate in the corrugated flamelet range**, where both the integral space scale (L_{Int}) is higher than the flame front thickness (δ) and the turbulence intensity (u') is higher than the laminar combustion velocity (S_l).
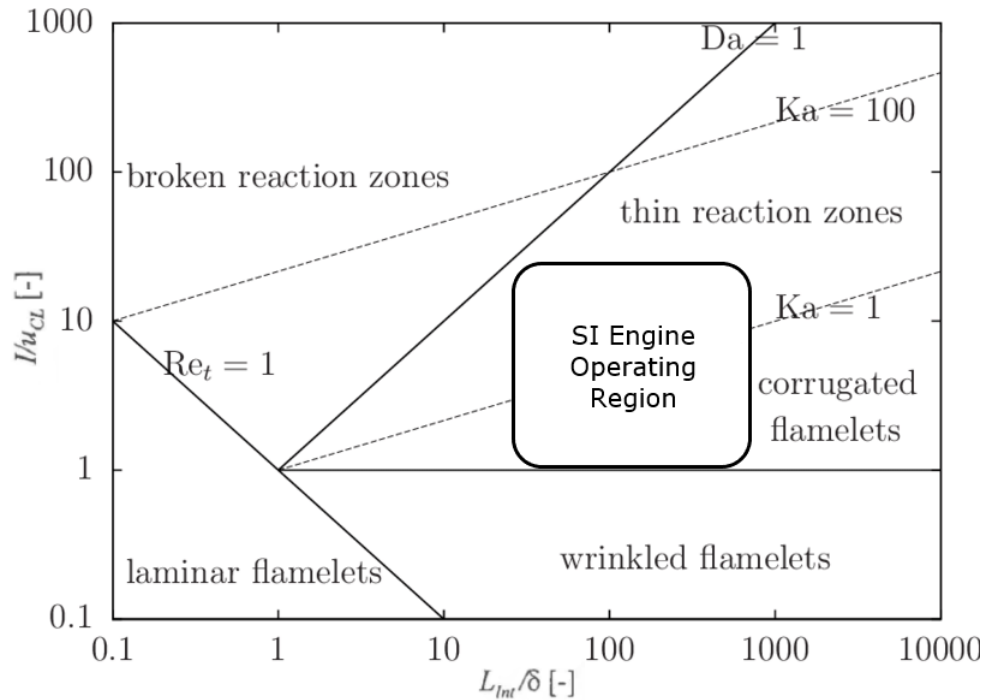
FIGURE 6: Turbulent Premixed Combustion Diagram [1].

These levels of turbulence translate into the formation of flamelets in the flame front (Figure 7) increasing its area and, thus, the combustion velocity. In this region, it has been proved that the turbulent combustion velocity can be scaled by using the turbulence intensity, which is proportional to the engine speed or the mean piston speed.

FIGURE 7: Corrugated Flame [1].

Another phenomenon that increases the combustion velocity appears due to the **development of the combustion in an enclosed space**. The increase in temperature in the burned gas zone leads to an expansion that pushes the flame front towards the unburned gas region, **adding a drag velocity u_A to the own flame front speed**. This velocity can be found if both the instant values of the flame front area and pressure chamber are known.

In Figure 8, the qualitative evolution of these speeds inside of a spherical chamber of radius R_{max} is shown together with the magnitude orders that typically appear in SI engines. Both the turbulence and the drag front effects can be seen here. In this figure, u_F represents the sum of the turbulent and drag velocities, while u_{CL} indicates the laminar combustion velocity. Due to these phenomena, the conversion of fresh mixture into burned gas is fast enough to assure an acceptable performance of the engine cycle [1].
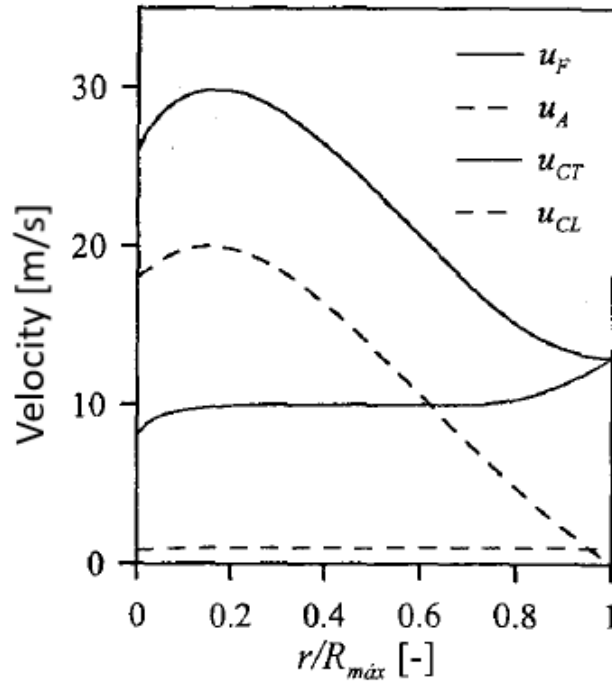
FIGURE 8: Combustion velocities evolution [1].

2.3   Factors affecting Combustion Process and Cyclic Dispersion

There are several parameters that influence the combustion process. They can be classified in two groups: **design and operation factors**. Examples of the first group are, among others, the geometry of the combustion chamber, the location and number of sparkplugs and so on. Once the engine is designed, only the parameters from the second group affect the combustion process. These parameters are introduced below alongside the effects that they cause.

- **Spark Advance (SA).** The spark timing characterises the combustion phasing and hence has a significant influence in the work that the cycle develops. As the ignition

advances two things happen. On the one hand, the combustion is advanced, therefore the maximum chamber temperature and pressure tend to raise. On the other hand, the heat transferred to the walls increases generating the opposite effect.

In what refers to the mean effective pressure, when the spark settings are retarded, the combustion might not be completed by the end of the expansion stroke. However, if the ignition is produced far before the top dead center, most of the energy will be delivered at the compression stroke, thus, opposing the normal movement of the piston. Between both situations, there is one case that maximizes the combustion efficiency. In this case, the combustion is centered and the spark advance is optimum.

- **Engine Speed (n).** Increasing the engine speed while keeping the rest of the magnitudes constant, increases the duration of the combustion and it is necessary to advance the ignition for keeping a centered combustion. The increase in engine speed produces a rise in the turbulence. In current engines, the variation of spark advance with respect to the engine speed is controlled by an electronic control unit (ECU).

- **Load Level.** As the engine load decreases, the in-cylinder residual gas fraction increases as it can be seen in Figure 9. The higher the inert gas content is in-cylinder, the slower the flame front propagation speed (both laminar and turbulent).
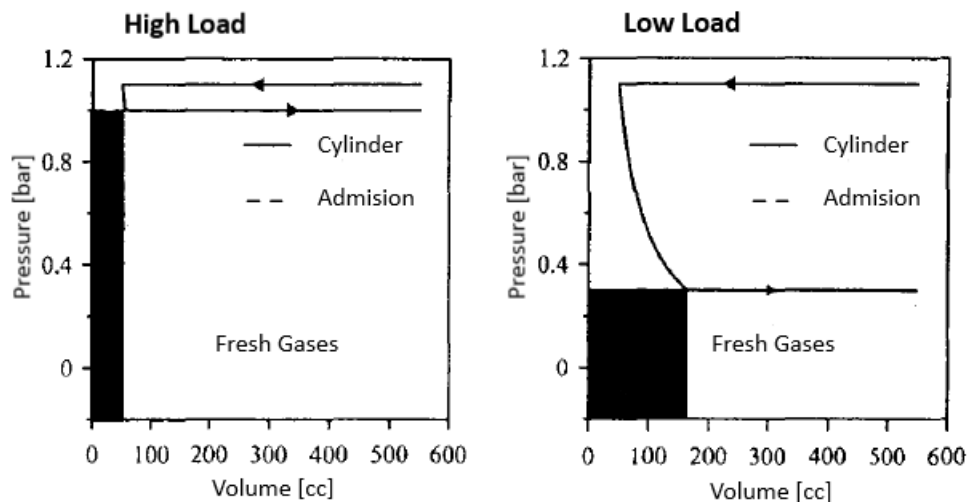
FIGURE 9: RGF vs Engine load [1].

- **Environmental conditions.** If the outside pressure is reduced, the enclosed in-cylinder mass will decrease and the heat loss fraction will become more relevant. Hence, the cooling will be higher and the reduction of temperature will produce a decrease of the combustion velocity. Then, a reduction on the outside pressure or temperature translates into a longer combustion. On the other hand, humidity increases the inert mass fraction in the mixture, decreasing combustion temperature and velocity and increasing the combustion duration. However, the effect of the envi-

ronmental conditions is not very significant.

Cycle-to-cycle dispersion is in SI engines an important feature when analysing pressure evolution. The main argument explaining this behaviour is the differences in the combustion evolution in the first stage. This stage has laminar character and its combustion velocity strongly depends on the local conditions (air-to-fuel ratio and turbulence) existing between the electrodes of the sparkplug. These conditions can easily change between cycles due to the chaotic nature of the mixture movement inside the chamber. For example, if a turbulent vortex is centered in the space between the electrodes of the sparkplug, the flame front propagation will be slower than in the case where the vortex is centered below, thus adding an extra velocity to the flame front spread.
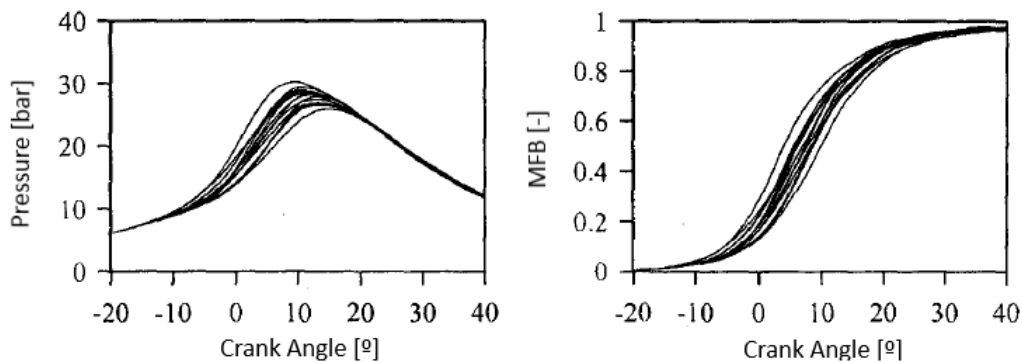
FIGURE 10: Example of Cyclic Dispersion [1].

The more pronounced the cyclic dispersion is, the lower the laminar combustion velocity will be. For this reason, cyclic dispersion is higher the more diluted the mixture is. This fact happens either in the case where the exhaust gas recirculation (EGR) is used or when the engine operates far from the stoichiometric air-to-fuel ratio. This dispersion can be seen as a variation of the combustion location in the cycle, just as if the ignition instant would have changed [1].

2.4   Aim and Basic Principles of Modelling

It is understood by **engine modelling** as the calculation of engine systems using mathematical models which are implemented in the form of computer programs. These mathematical models solve the equations of a physical model that intends to represent the most relevant phenomena in the engine system. The fidelity of the model with respect to the physic phenomena will be determined by the hypothesis that have been made.

Models are used for a wide range of applications. Some of them are evaluating different design options, predicting engine performance and limitations, analysing physic phenomena, identifying parameters that control processes, predicting tendencies and analysing output variables sensibility. Modelling has become a key tool for engine design since it allows to evaluate several design options with a low cost and in a reasonable period of time.

In the majority of the system, a **combination between testing and modelling** is the best strategy for the engine system analysis and synthesis. This combination must be understood as two complementary activities for the engine design process. On the one hand, experimental tests are closer to reality, however, they are more expensive and may be affected by measurement uncertainty. On the other hand, models are faster and cheaper, but they have to be validated with some experimental tests.

Currently, models have become another part of the engine in the form of implemented control strategies in the electronic control unit (ECU). These strategies allow the engine performing diagnosis, estimating specific magnitudes or optimizing the operation point in real time. The trend to cheapening of the computational capacity will increase the usage of models in the engine control.

The **process of modelling** can be summed up in the next four steps:

1. **Physical phenomena analysis.** It is important to determine the model range as well as which physic phenomena are more important and which ones can be neglected.

2. **Physical model elaboration.** At this point, simplifying assumptions are made. Furthermore, the input and output magnitudes are chosen.

3. **Mathematical model elaboration.** Depending on the established hypothesis, the equations that represented the physical phenomenon are obtained and their resolution methods set.

4. **Computational model elaboration.** Programming the mathematical model resolution, and also the integration of the program in an environment that allows to enter data (pre-process) and exploit results (post-process) [1].

2.5   Combustion Modelling and Types

Combustion modelling is one of the most important aspects to consider for a global engine simulation. Besides, it is one of the most complex processes to model due to its transient, heterogeneous, multiphasic and turbulent nature. Combustion cannot be analysed using mean values since time is a fundamental parameter. Taking this into account, **combustion models can be classified into three groups**.

1. **0-dimensional or Thermodynamic Models.** Based mainly in the energy conservation law, assuming spatial homogeneity in the involved variables. Depending on the unknown term of the energy conservation law (Equation 4), the model to be used can be either predictive or diagnostic.

$$m \cdot c_v \cdot \frac{\mathrm{d}T}{\mathrm{d}t} \;=\; \frac{\mathrm{d}Q_R}{\mathrm{d}t} + \sum_w \frac{\mathrm{d}Q_w}{\mathrm{d}t} - p \cdot \frac{\mathrm{d}V}{\mathrm{d}t} \tag{4}$$

where m is the total mass, c_v the specific heat at constant volume, Q_R the reaction heat and Q_w the wall transfer heat.

Predictive models evaluate engine performance from their operation conditions, geometric configuration and instant pressure evolution. Their interest lies in the wider parametric studies that can be done respect to the experimental way. These models require a previous knowledge of the heat released law.

Diagnostic models use instant in-cylinder pressure evolution obtained experimentally in order to calculate the heat released law.

The use of thermodynamic models have a special interest to both ease the interpretation of the variables measured experimentally and to calculate hard to measure variables. Therefore, its usage is recommended for the engine fine-tuning and optimization. As more sophisticated the incorporated sub-models are (for example, to calculate the wall heat transfer) the more accurate the instant thermodynamic properties will be. Figure 11 shows a diagram of the described models.
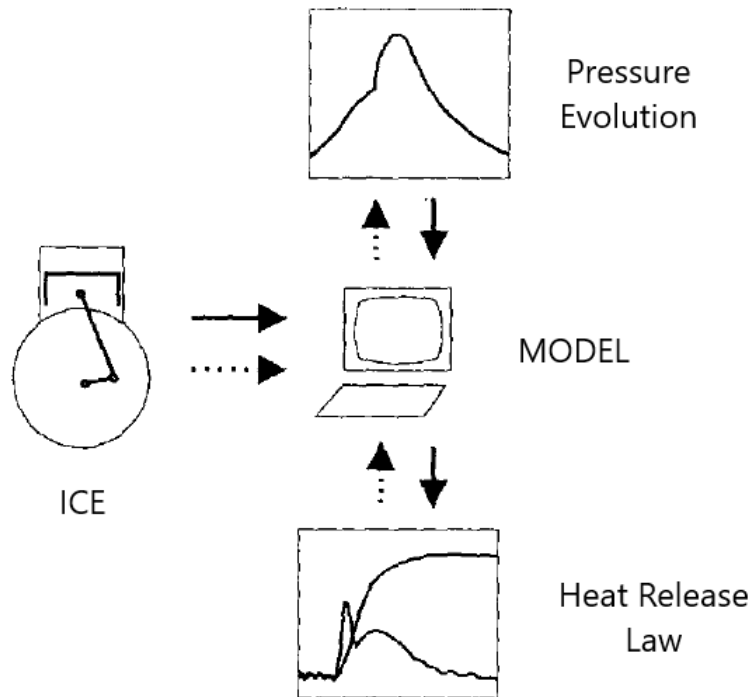
FIGURE 11: Predictive and diagnostic model diagram [1].

The usual **hypothesis** considered to simplify Equation 4 are:

- **Uniform pressure** inside the combustion chamber. This hypothesis provides good results as the flame propagation speed is lower than the sound speed.

- The flow inside the combustion chamber is a **homogeneous mixture** of air and fuel burned in stoichiometric conditions.

- The in-cylinder mixture behaves as an **ideal gas**. The existing thermodynamic conditions in the combustion chamber are not the ones required for the saturation of the mixture components.

- To get an **estimation of the wall heat transfer** it is usually employed the expression of the instant film coefficient proposed by **Woschni**, including in just one term the combined effect of convection and radiation.

2. **Quasi-dimensional or Phenomenological Models**. Quasi-dimensional models are those which, together with the basic thermodynamic approach, include some **geometrical aspects of the combustion process** and/or additional details for some of the involved combustion phenomena. These models include the **concept of space**. They usually divide the combustion chamber in several zones with homogeneous properties in each one, being necessary the resolution of the mass and energy conservation equation for each zone to solve the problem.

These models allow to estimate qualitatively either the formation or destruction of the polluting emissions since they keep a physic part of the problem. Besides, the calculation time required is reasonable compared to multidimensional ones making possible to establish cause-effect relationships. However, some coefficients need to be fitted with experimental results due to the great number of required simplifications. Since the combustion structure is different in SI engines and CI engines, a differentiation in phenomenological type models is made depending on its application. The focus will be put on those used for SI engines.

Two zone models are suitable to analyse the combustion in SI engines. There are two main zones in the combustion chamber separated by the flame front (Figure 12), being the conditions in each zone homogeneous. The first one is the unburned gas region which contains a homogeneous mixture of air, fuel, residual gas and EGR. The other zone is the burned gas region filled of the resultant species from combustion.

In order to accurately approach the real process, the physical separation between zones it is modelled assuming that the **front flame has spherical geometry**, with its center at the sparkplug and its radius estimated from the instant position of the flame front mean section. Thus, the area will be the one corresponding to the sphere fraction bounded by the combustion chamber walls. As these hypothesis are made, the combustion process evolution, in energetic terms, mainly depends on both the flame front speed and its area. Hence, there are two methods for modelling this process accurately.
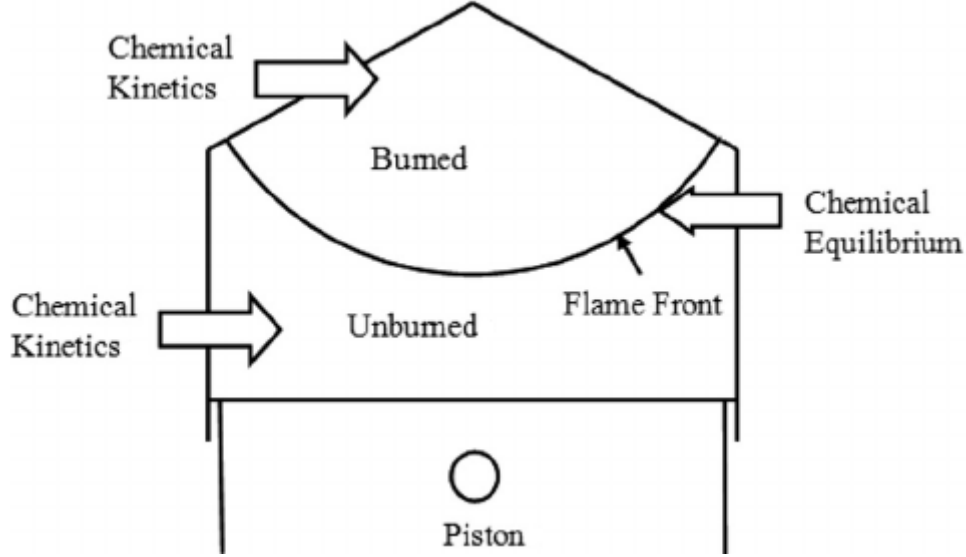
FIGURE 12: Two zones combustion chamber [1].

- **Turbulent combustion speed based models.** For an specific chamber geometry, the mass fraction burned (MFB) is determined from Equation 5 using the burned mixture density (ρ_{ub}), the flame front area (A_f) and the turbulent speed (u_{CT}) as inputs.

$$\frac{\mathrm{d}m_b}{\mathrm{d}t} = \rho_{ub} \cdot A_f \cdot u_{CT} \tag{5}$$

Turbulence effect remains implicit only in the turbulent speed term, which have to be conveniently modelled. This parameter is usually estimated using $k - \epsilon$ type turbulence models, by means of the kinetic turbulent energy (k) or the turbulence intensity (u') and its dissipation rate (ϵ).

- **Flame front effective area based models.** If both the flame front thickness is negligible and the combustion process is developed in the premixed corrugated flamelet region, as expected for a SI engine (Figure 6), then the increase of the flame front area due to turbulence will be the main cause of the combustion rate increase with respect to the one that would take place in laminar flow conditions. With all this, the mass fraction burned is expressed on Equation 6, where the turbulence effect is included in the turbulent flame front area term (A_{ef}), which have to be properly modelled.

$$\frac{\mathrm{d}m_b}{\mathrm{d}t} = \rho_{ub} \cdot A_{ef} \cdot S_l \tag{6}$$

Typically, this turbulent flame front area is related to the laminar one multiplied by the flame speed ratio (FSR). It can be estimated with models based on the fractal geometry concept. In this approach, a similarity between turbulence scales of different sizes is assumed, so that the flame front, deformed by its interaction with the turbulence, presents the nature of a fractal object. In order to apply this combustion model, a proper turbulence model should be couple to obtain the values of the involved space scales, usually a $k - K$ type (turbulent kinetic energy – mean flow kinetic energy).

3. **Fluid Dynamic Models (CFD).** The utility of these type of models lies in the limitations and constraints of the zero-dimensional and quasi-dimensional models. Fluid dynamic models **retain the physics of the problem** without assuming important simplifications. **They give back detailed information** of the combustion morphological characteristics (good spatial resolution) and, besides, allow to model the effect of the combustion chamber walls.

Currently, these multidimensional models **are widespread** in the engine scope. However, the combustion process modelling in CFD is **highly complex** due to some physical-chemical problems that have to be properly approached. The most relevants are: get to know the fluid mechanical properties of the combustion system, properly model turbulence characteristics, trace a detailed scheme of chemical evolution during combustion, and measure the energy loss due to convection and radiation wall heat transfer phenomena. Moreover, it is convenient to differentiate between CFD modelling in SI engines and in CI engines, since the combustion characteristics are essentially different [1].

3   Experimental System Description

3.1   Renault HR13 Engine

The engine studied and analysed for this master thesis has been the HR13 engine from Groupe Renault (Figure 13). This is a **new 1.3 direct-injection turbocharged petrol engine**, result of a collaboration between the Alliance and Daimler. It can be found under the bonnets of Renault Scénic and Grand Scénic models.

FIGURE 13: Renault HR13 engine [2].

In particular, this model is a **4 cylinder** engine with a capacity of **1330 cm³**. It has a **power of 140 hp** (103 kW) that can produce a maximum **torque of 270 Nm** from 1500 rpm to 3500 rpm. Some innovations that this engine incorporates are:

- **Bore spray coating technology** to improve the efficiency by both reducing friction and optimising heat conduction.

- **Direct injection** boosting fuel pressure to **250 bar**.

- **Special combustion chamber** to optimise the air-fuel mixture.

- **Dual variable valve timing camshaft technology** that controls the intake and exhaust valves. This leads to both higher torque at low revolutions and more consistent torque at higher speeds.

- **Turbocharger** equipped with a motor-driven **recirculating safety valve**.

Some **geometric parameters** from the HR13 engine are collected below in Table 2. These parameters will be necessary to calculate the instantaneous combustion chamber volume, among other magnitudes [2].

Parameter	Value	Units
Number of cylinders	4	-
Bore diameter	72.2	mm
Bore area	163.8	cm^2
Stroke	81.2	mm
Connecting rod length	128	mm
Crank length	40.6	mm
Compression ratio	10.6	-

TABLE 2: HR13 engine geometric parameters [2].

3.2   Experimental Facilities

Experimental data are necessary in order to calibrate, compare and validate the combustion model. These experimental data were obtained at the **CMT facilities**. Besides the main building (Figure 1), CMT also dispose of the Center for the Improvement of the Efficiency and Environmental Impact of Transport Systems (CiMeT) shown below in Figure 14. This center has fully equipped test benches prepared for the installation of wired engines along with the sensors and the data acquisition systems.

CMT experimental facilities for engine tests consist of 14 engine test cells. Each one has different characteristics and capacities, and are fitted out with a control room (Figure 15)and the necessary equipment and instrumentation. Eight of them are dedicated to multi-cylinder engines (Figure 16). These test cells are equipped with asynchronous machines to perform steady and transient tests for vehicle dynamic cycles. Among others, it has been used:

FIGURE 14: CiMeT building [3].

- **Electrical brakes** for test automation.

- **Piezo-electric and piezo-resistive sensors** for intake/exhaust manifolds and in-cylinder pressure. measurements with high accuracy and wide dynamic range.

- **Hot plate anemometers** for intake air mass flow measurements.

- **Gravimetric sensors** for fuel consumption measurements.

- **High speed data acquisition and engine control system.**

- **Systems for exhaust and particulate emissions measurements** [2].

Figure 15: Test cell control room [2].
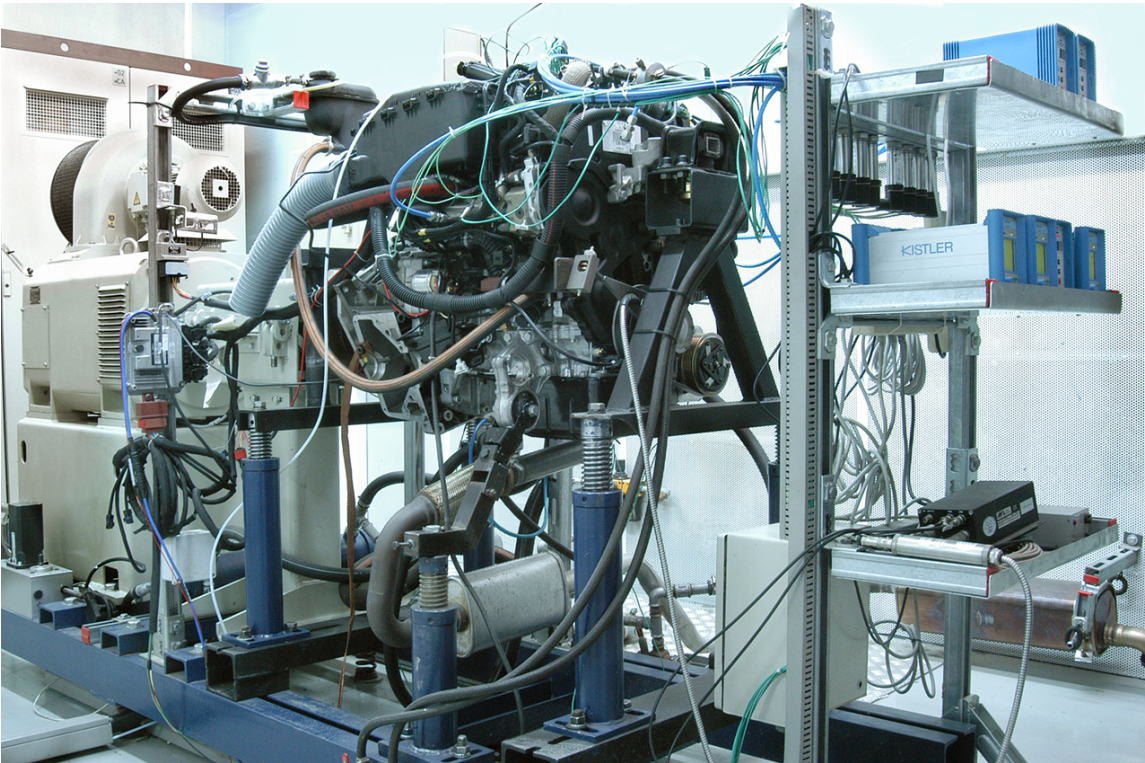
Figure 16: Multi-cylinder engine test cell [2].

3.3 Data Acquisition Systems

Three different acquisition systems were used for the data extraction during the tests: AVL PUMA, INCA and Labview. They will be described below.

AVL PUMA control system is an effective tool to do engine tests on the test bench. Among other parameters, it controls engine speed, load level, torque and fuel balance filling. Besides, pressure and temperature limits of each critical part are established in order to redirect operating conditions to safe ones when these limits are overcome preventing components from breaking. For this purpose, several temperature and pressure sensors (admission, escape, fuel, oil or water) are connected to AVL PUMA. Figure 17 shows the control screen. At the left top part, the engine speed, load level and torque indicators can be found. AVL PUMA saves the parameters mean values measured by the sensors in each cycle.

FIGURE 17: PUMA's control screen.

INCA is an engine control system that reads and modifies parameters defined at the Engine Control Unit (ECU). The most relevant parameters have been collected in Table 3, relating the variable name with its description. From the main screen of INCA (Figure 18), logical switches can be activated or deactivated and a specific point of operation can be set by modifying engine parameters. As AVL PUMA does, the INCA control system also saves the parameters mean values in each cycle.

The third acquisition system is **Labview**, a program employed for analysing and obtaining data that the ECU cannot. These data come from high frequency sensors which collect 3600 samples per cycle (one each 0.2 crank angle degree). With these sensors, it has been measured the instantaneous intake/exhaust manifold pressure, instantaneous in-cylinder pressure and the knocking percentage on each cylinder. These parameters can be seen in real time in the main screen of the program (Figure 19). The heat released law on each cylinder can also be found at the right part [5].
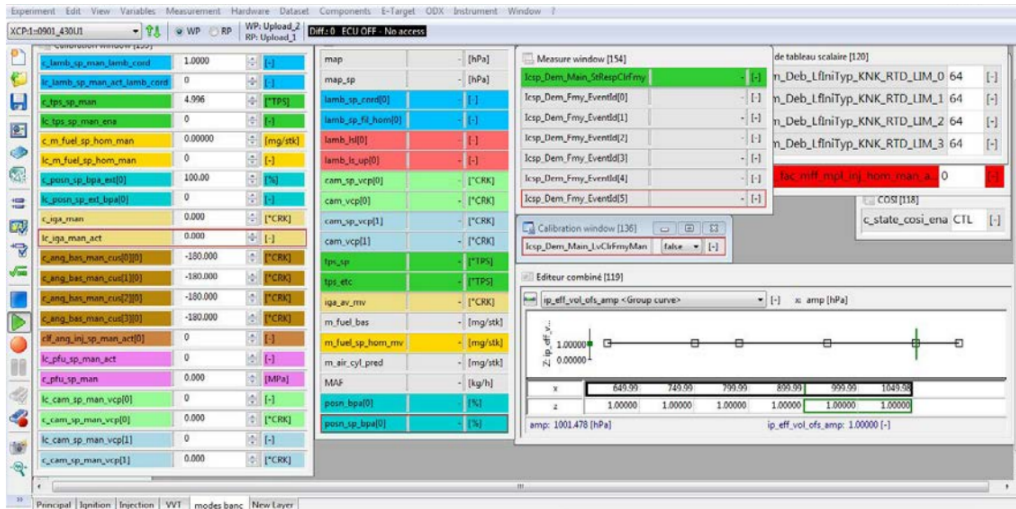
FIGURE 18: INCA's control screen.

INCA's Variable Name	Description
c_lamb_sp_man_lamb_coord	Lambda control value
lc_lamb_sp_man_act_lamb_coord	Lambda logic control switch
c_n_fuel_sp_hom_man	Injected fuel control value in mg/stk per cylinder
lc_n_fuel_sp_hom_man	Injected fuel logic control switch
c_iga_man	Ignition advance control value
lc_iga_man_act	Ignition advance logic control switch
c_cam_sp_man_vcp[0]	Admission valve position control value
lc_cam_sp_man_vcp[0]	Admission valve position logic control switch
c_cam_sp_man_vcp[1]	Exhaust valve position control value
lc_cam_sp_man_vcp[1]	Exhaust valve position logic control switch
map	Admission pressure value in hPa
MAF	Mass air flow value in kg/h

TABLE 3: INCA's variables description.
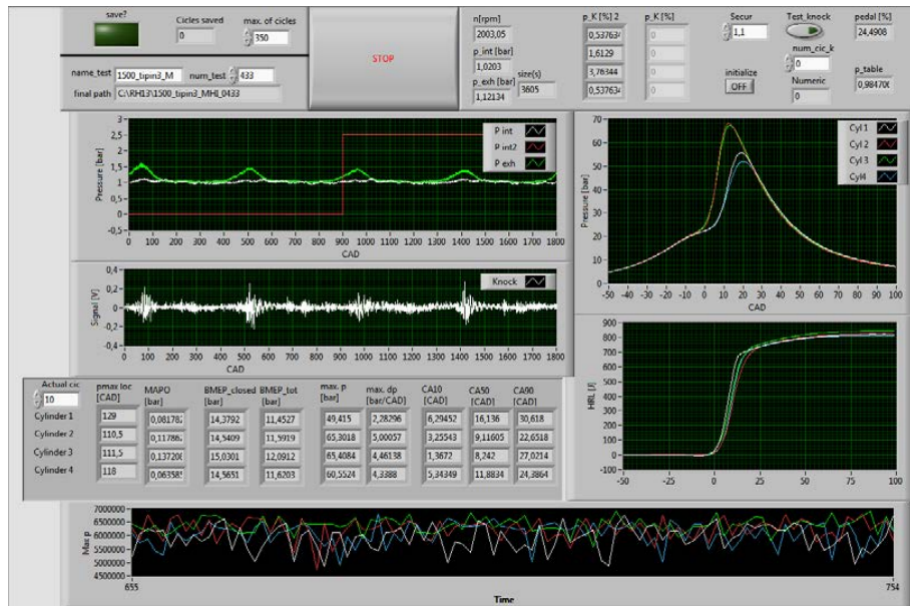
FIGURE 19: Labview's control screen.

3.4 Sensors

In this section, the **different type of sensors** used by the three acquisition system mentioned above will be briefly detailed.

To measure temperature, two types of sensors have been used: thermocouple and thermal resistance.

- **Thermocouples** consist of two conductive metal filaments attached at the ends, so when one end is heated a potential difference is generated proportional to the temperature. This means that thermocouples measure relative temperatures between the heated end and the cold one. There are different types depending on the metal. The most common are the K type, composed of nickel-chrome at the hot end and nickel-aluminium at the cold end. Thermocouples have been placed in the engine to measure temperatures at the intake/exhaust manifolds, compressor, turbine, intercooler, oil, coolant, particle filter and at each cylinder admission.

FIGURE 20: K type thermocouple.

- **Thermal resistances** consist of two metallic filaments (usually made of platinum, nickel or copper) whose electrical resistance varies due to temperature variation. They are often used for measuring liquid temperatures. Therefore, they are encapsulated to isolate filaments from moisture. Thermal resistances have been placed to measure coolant, oil and fuel temperatures.
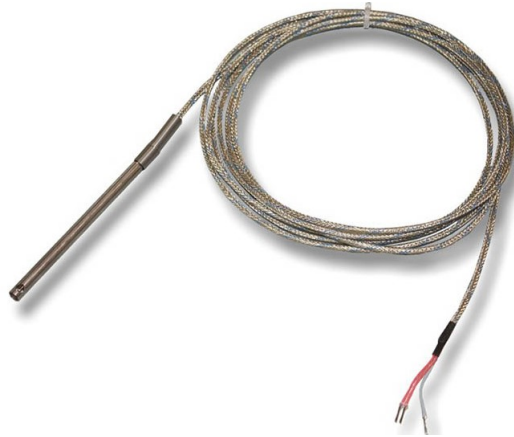
Figure 21: Thermal resistance.

To measure pressure, three types of sensors have been used: mean pressure sensors, instantaneous pressure sensors and the instrumented sparkplug.

- **Mean pressure sensors** are used to measure pressure at points where it is constant. They have a piezoresistive behaviour so the electrical resistance of the material varies in function of the mechanical stress. There have been placed to measure pressure at the air filter, compressor, intake/exhaust manifolds, turbine, coolant, oil and fuel.
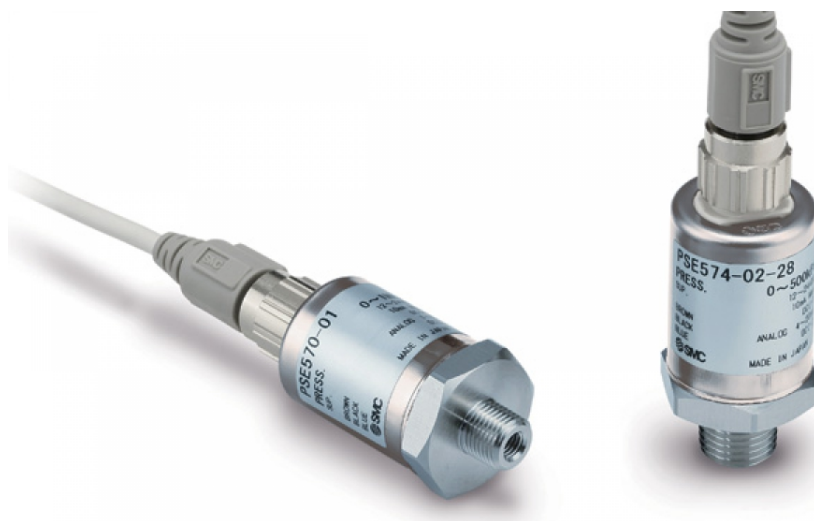
Figure 22: Mean pressure sensor.

- **Instantaneous pressure sensors** have a higher sampling frequency than mean pressure sensors. This allows to acquire a greater number of data to analyse pressure changes. They are placed at the intake and exhaust manifolds, and the one on the exhaust has to be cooled due to higher temperatures.

FIGURE 23: Instantaneous pressure sensors KISTLER 4049A y 4045A.

- **The instrumented sparkplug** is an instantaneous pressure sensor integrated in the sparkplug. It allows to register both pressure variation inside the combustion chamber and the knocking phenomena (autoignition in combustion chamber).

FIGURE 24: Instrumented sparkplug AVL ZI33.

To measure air-fuel mass and control its ratio, three types of sensors have been used: the caudalimeter, the fuel balance and the lambda probe.

- **The caudalimeter** determines the air mass flow by means of two ultrasound sensors (Figure 25). Flow velocity can be obtained through the time delay in the sound signal due to air mass flow. By knowing both air density and section area, the air mass flow can be calculated.
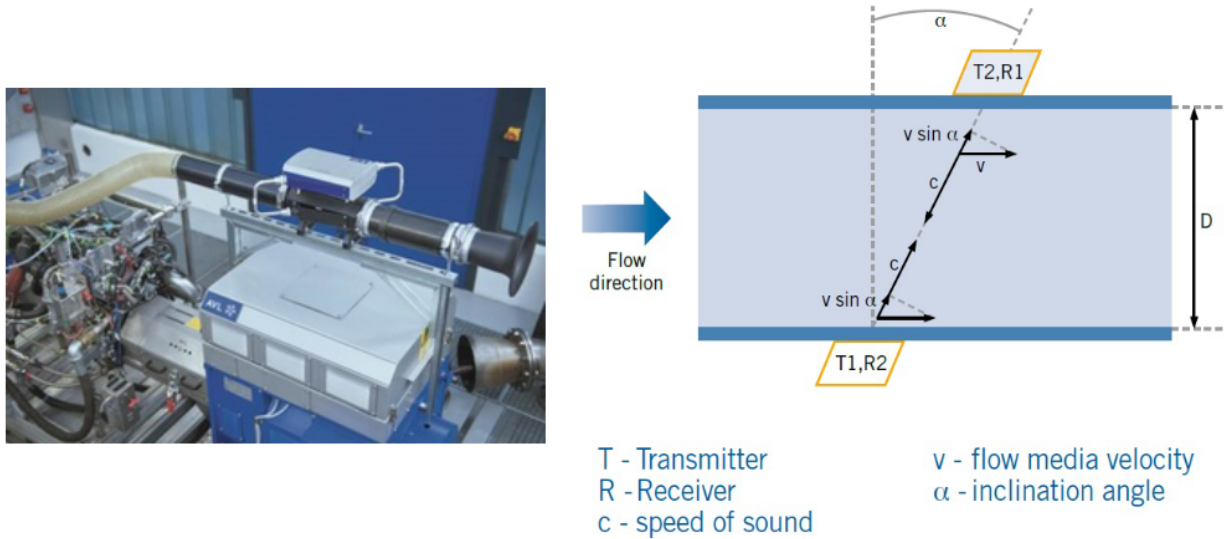
Figure 25: Caudalimeter and its operation.

- **The fuel balance** is a measure tool for the fuel mass flow. It consists of a simple balance with a fuel deposit on one side and calibrated weights with a load cell on the other. This way, when the deposit is emptying, the weights push the load cell harder. It is a simple and accurate sensor shown in Figure 26.
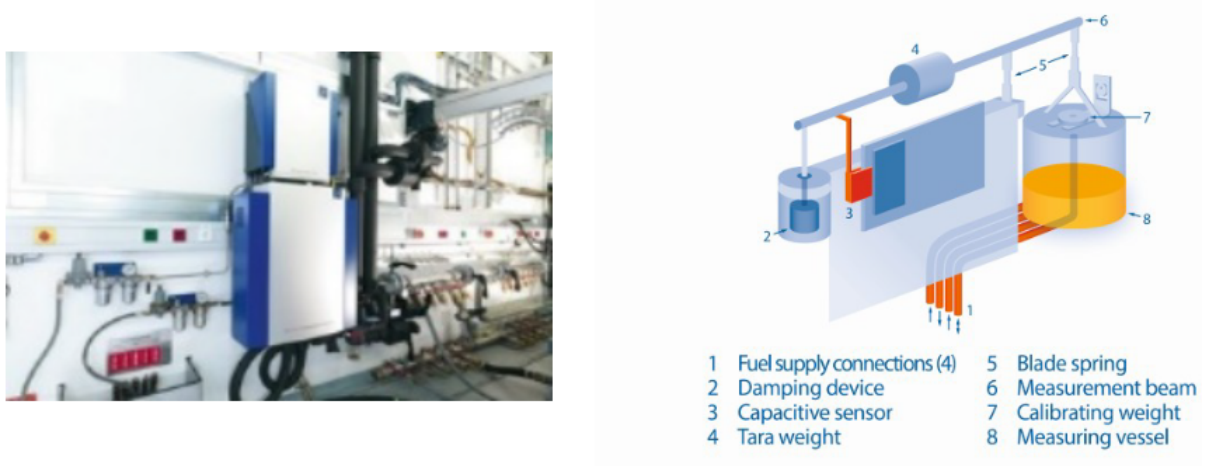
Figure 26: Fuel balance and its operation.

- **The lambda probe** controls the stoichiometry of the air-fuel mixture. This sensor calculate in real time the air-to-fuel ratio (λ), keeping it constant by adjusting other

parameters.

Figure 27: Lambda probe.

To determine the instant angular position of the crank, an **angular encoder** is used. This sensor contains a cogwheel attached to either the crank or other rotating element, and an optic sensor. This optic sensor varies its output tension every time a cog pass through it, so that each pulse equals to a certain angle.

Figure 28: KISTLER crank angle encoder.

Finally, a **torquemeter** is used **to measure the torque generated** by the engine. Its functioning is based on the deformation that a normalized test piece experiments, which is measured by two angular encoders. Each encoder measures the angular difference between two cogwheels united by a material of known mechanical characteristics. From this deformation, the produced torque can be calculated. For the test, an asynchronous dynamometer model AFA 200/4-8EU from AVL has been used [5].

Figure 29: Torquemeter.

3.5 Experimental Data Collected and Phasing

From all the sensors mentioned above, **experimental data have been collected** after carrying out tests at the CMT facilities. The relevant data to build the model are highlighted below.

As **model input variables**, **the engine speed, intake manifold pressure, spark advance angle and the air and fuel mass flow** are required in each cycle. Note that either air or fuel mass flow can be replaced by the λ parameter. Some of these values can be taken from either PUMA or INCA (except if the variable only appears in one of them). However, for accuracy reasons, they have been all taken from the INCA control system.

Besides these parameters, the **instant in-cylinder pressure evolution** is required to obtain the heat released during combustion. These data can only be extracted from Labview, which has an acquisition frequency of 100 Hz and collects 3600 samples per cycle (depending on the engine speed).

Once all data are collected, it is necessary to phase the data from the three acquisition systems. **Phasing is mandatory since the three systems don't start recording data at the same time**. By means of a signal called the pedal signal (which is got by the three systems) the three data groups should be phased in order to make working with them easier.

4 Experimental Data Analysis

The experimental data **analysis is divided in two parts**. First, the average values of each constant inputs set will be used for a **mean value combustion analysis**. Then, in Chapter 6, a **cycle-by-cycle analysis** will be done to study the combustion dispersion. In the following sections, the combustion analysis from the experimental data will be carried out in order to obtain the mass fraction burned (MFB).

4.1 Extracted Data

Two different types of data have been extracted from the engine. On the one hand, **the characterization data** (Table 4) used for both the combustion analysis and the development of the model. It **consists of 54 sets** of **300 cycles each**, which can be divided into **3 big blocks of engine speeds of 1000, 2000 and 3000 rpm**. Each big block can be split into **3 small blocks of low, medium and high load**. In each of the resulting 9 small blocks, a **sweep of spark advances** has been made, getting as close as possible to the combustion auto-ignition point without damaging the engine.

	1	2	3	4	5	6	7	8	9	10	11
n [rpm]	1000	1000	1000	1000	1000	1000	1000	1000	1000	1000	1000
SA [°]	1.88	4.5	7.13	9.38	12	14.63	16.88	19.5	1.88	4.5	7.13
p_0 **[bar]**	0.53	0.5	0.49	0.49	0.49	0.49	0.49	0.49	0.82	0.82	0.82
m_f **[mg]**	10.13	9.62	9.22	9.24	9.22	9.3	9.35	9.26	15.81	15.78	15.86
λ **[-]**	1	1	1	1	1	1	1	1	1	1	1

	12	13	14	15	16	17	18	19	20	21	22
n [rpm]	1000	1000	1000	1000	1000	1000	1000	1000	1000	1000	2000
SA [°]	9.38	12	14.63	16.88	19.5	-3	-0.38	1.88	4.5	7.13	1.88
p_0 **[bar]**	0.82	0.82	0.82	0.82	0.82	0.97	0.97	0.97	0.97	0.97	0.83
m_f **[mg]**	15.8	15.83	15.9	15.84	15.84	22.85	22.8	22.8	22.8	22.9	17.37
λ **[-]**	1	1	1	1	1	1	1	1	1	1	1

	23	24	25	26	27	28	29	30	31	32	33
n [rpm]	2000	2000	2000	2000	2000	2000	2000	2000	2000	2000	2000
SA [°]	9.38	12	14.63	16.88	19.5	-3	-0.38	1.88	4.5	7.13	1.88
p_0 [bar]	0.82	0.79	0.77	0.75	0.76	0.76	0.76	1.26	1.2	1.19	1.15
m_f [mg]	17.17	16.1	15.65	14.93	15.07	14.93	15.15	32.9	31.46	30.86	29.95
λ [-]	1	1	1	1	1	1	1	1	1	1	1

	34	35	36	37	38	39	40	41	42	43	44
n [rpm]	2000	2000	2000	2000	2000	2000	2000	2000	3000	3000	3000
SA [°]	7.13	-5.63	-3	-0.38	1.13	4.5	7.13	9.38	12	14.63	16.88
p_0 [bar]	1.13	1.73	1.68	1.61	1.61	0.77	0.77	0.77	0.78	0.77	0.77
m_f [mg]	29.39	45.7	44.42	42.32	42.32	16.5	16.33	16.15	16.66	16.3	16.4
λ [-]	1	1	1	1	1	1	1	1	1	1	1

	45	46	47	48	49	50	51	52	53	54
n [rpm]	3000	3000	3000	3000	3000	3000	3000	3000	3000	3000
SA [°]	19.5	1.88	4.5	7.13	9.38	12	14.63	-0.38	1.88	4.5
p_0 [bar]	0.76	1.13	1.16	1.15	1.13	1.16	1.15	1.6	1.64	1.64
m_f [mg]	16.08	28.48	29.11	28.83	28.35	29.08	28.6	41.26	42.03	42.23
λ [-]	1	1	1	1	1	1	1	1	1	1

Table 4: Characterization data.

The validation data (Table 5) were also extracted to validate the model results. The **11 sets**, of **300 cycles** each, were taken from a previous test bench data used for another research on the same engine. As the range of the characterization data was wide enough, the validation sets have been **selected for in-between values of both engine speed and load**. The sets can be divided into 3 blocks of engine speeds of 2000, 2500 and 3000 rpm. The first block contains a spark advance sweep of 4 sets at medium-high engine load. The second block has 3 sets of medium-high engine speed with medium and medium-low engine load. Finally, the third block includes 4 sets of medium-low and medium-high engine load for different spark advances.

	1	2	3	4	5	6	7	8	9	10	11
n [rpm]	2000	2000	2000	2000	2500	2500	2500	3000	3000	3000	3000
SA [º]	4.13	7.5	8.63	9.75	13.13	6	10.5	13.88	7.88	12	13.88
p_0 **[bar]**	1.05	1.05	1.05	1.05	1.02	1.19	1.19	0.99	1.35	1.35	1.35
m_f **[mg]**	25.9	25.9	25.9	25.9	25.2	30.1	30.1	23.6	33.1	33.1	33.1
λ **[-]**	1	1	1	1	1	1	1	1	1	1	1

TABLE 5: Validation data.

Once the experimental data have been collected, discretized and phased from the three different data acquisition systems, the data processing follows with the combustion process analysis.

4.2   Combustion Analysis Hypothesis

For a given operation point, with constant input parameters (engine speed, spark advance, intake pressure and temperature, air and fuel mass), the instantaneous pressure evolution data is known. Then, **the heat released during combustion can be obtained through the energy conservation law** [6]. This law (Equation 7) exposes that the energy released during combustion (dQ_{comb}) must be equal to the gas internal energy variation (dU) plus the work transferred to the piston (dW) and the wall transfer heat (dQ_w).

$$\mathrm{d}Q = \mathrm{d}U + \mathrm{d}W$$

$$\mathrm{d}Q_{comb} = \mathrm{d}U + \mathrm{d}W + \mathrm{d}Q_w \tag{7}$$

In order to simplify the problem and solve the equation, some reasonable **hypothesis** are made:

- **Homogeneous air-fuel gas mixture** inside the combustion chamber.

- Air-fuel mixture can be considered as an **ideal gas**. Equation 8 shows the ideal gas law, being R the ideal gas constant.

$$p \cdot V = m \cdot R \cdot T \tag{8}$$

- To avoid quantifying the wall transfer heat, **the system will be considered adiabatic**. The adiabatic index (γ) will be replaced by a **polytropic coefficient** (κ) of a lower value in order to compensate the loss of energy.

Applying these assumptions, the work transferred to the piston and the internal energy variation can be written as Equations 9 and 10, respectively.

$$\mathrm{d}W = \frac{\kappa}{\kappa - 1} \cdot p \cdot \mathrm{d}V \tag{9}$$

$$\mathrm{d}U = \frac{1}{\kappa - 1} \cdot V \cdot \mathrm{d}p \tag{10}$$

Finally, the **energy released during combustion** (Equation 11) will be as it follows:

$$\mathrm{d}Q_{comb} = \frac{\kappa}{\kappa - 1} \cdot p \cdot \mathrm{d}V + \frac{1}{\kappa - 1} \cdot V \cdot \mathrm{d}p \tag{11}$$

As the experimental data is already discretized each 0.2 crank angle degrees, volume and pressure variations ($\mathrm{d}p$ & $\mathrm{d}V$) can be obtained from pressure and volume data. This is computed as the difference between one time-step and the next one. Thus, the instantaneous heat released can be calculated from Equation 11 and for **the total heat released it is enough to add up each instantaneous value**.

In Equation 11, pressure comes determined from the experimental data and the volume from the combustion chamber geometry. However, **the polytropic coefficient has to be determined** in order to obtain the heat released. In Figure 30, it can be seen the variation of the apparent heat released law with a variation of 0.03 in the polytropic coefficient.

This coefficient can be obtained from Equation 12, being points 1 and 2 different states of the non-adiabatic system.

$$\kappa = \frac{\log\left(p_1/p_2\right)}{\log\left(V_2/V_1\right)} \tag{12}$$
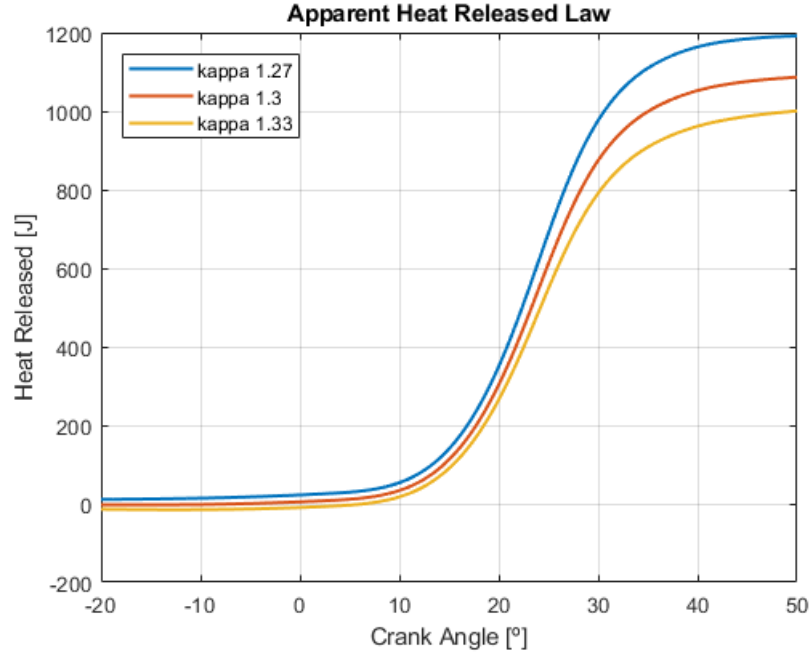
FIGURE 30: Apparent heat released law for different polytropic coefficients.

Nevertheless, this equation would not be useful for a model that aims to obtain the in-cylinder pressure evolution. Therefore, **a constant value of 1.3 was finally selected** for all cases and for the model, which is the common value used in these cases for simplicity [6].

This decision, along with the previous hypothesis made, introduces a certain error to the heat released calculated from the experimental data. The selection of the kappa value may change the curve obtained, as it can be seen in Figure 30. Due to this estimation, **the curve is typically called apparent heat released**.

4.3 Mass Fraction Burned

This section is focused on getting the **mass fraction burned from the apparent heat released curve**. To make this possible, the **time of combustion (TOC) must be established** by means of a start (SOC) and an end (EOC) of the combustion.

To find these two points **a least-squares adjustment is made between an auxiliary mass fraction burned** (Equation 13) **and a MFB from Wiebe's function** (Equation 14). The auxiliary mass fraction burned is obtained from the apparent heat released curve in which the EOC is located at the maximum heat released and the SOC at 30º before the 10% of the maximum heat released ($Q_{b\ aux}$) divided by its maximum ($Q_{b\ aux\ max}$). The criteria for the auxiliary SOC and EOC values selection were two: to include the whole heat released in the combustion and to select two recognizable points of the curve.

$$MFB_{aux} \;=\; \frac{Q_{b\ aux}}{Q_{b\ aux\ max}} \tag{13}$$

$$MFB_{wiebe} \;=\; 1 - \exp\left(-k_1 \cdot \left(\frac{\alpha - SOC}{TOC}\right)^{m+1}\right) \tag{14}$$

In Wiebe's function, SOC **and** TOC **are the variables to calibrate with the adjustment** whereas m and k_1 are Wiebe's function constants (Table 6) and α is the correspondent crank angle.

Parameter	Value
α [$^\circ$]	-180 $< \alpha <$ 540
k_1 [-]	6.9
m [-]	4

TABLE 6: Wiebe's equation data.

From this adjustment, the SOC and EOC points are extracted. After that, two possible choices can be made. On the one hand, the new mass fraction burned from Wiebe's function can be used. On the other hand, it can also be used the mass fraction burned (MFB) obtained from the apparent heat released curve with the extracted SOC and EOC (Eq. 15).

$$MFB \;=\; \frac{Q_b}{Q_{b\ max}} \tag{15}$$

In the first case, the new mass fraction burned from Wiebe's function has been fitted to the original one. Because of this, a certain error is already added to this curve (red curve in Figure 31). In the second case, the original curve is kept. However, at the EOC an abrupt change on the slope is produced, which is not typical in a regular combustion (Figure 32).

In both cases, the results obtained move away from reality. However, it was **decided to continue with the second option**, taking this fact into account for the later model calibration and results comparison.

Finally, the **burned mass evolution** (Equation 16) can be determined by multiplying the mass fraction burned by the total mass (Equation 17):

$$m_b \;=\; MFB \cdot m_{tot} \tag{16}$$

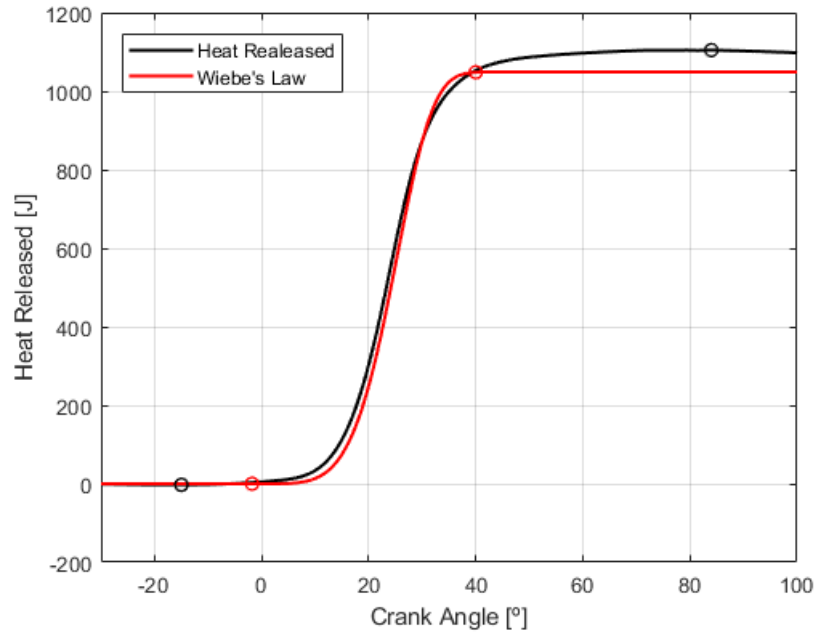$$m_{tot} \;=\; \frac{m_{air} + m_{fuel}}{1 - RGF} \tag{17}$$

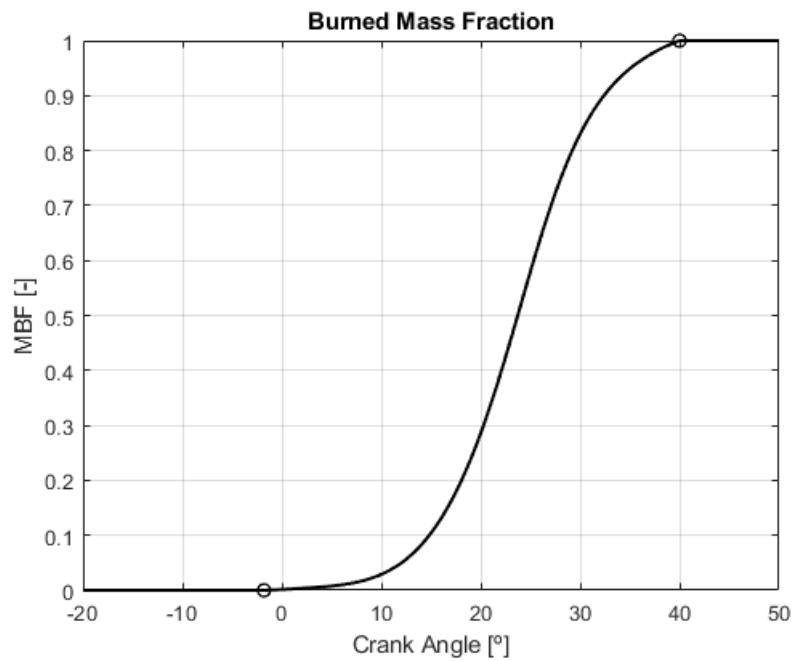FIGURE 31: SOC and EOC finding procedure.

FIGURE 32: Mass Fraction Burned.

The **residual gas fraction** (RGF) in Equation 17 is calculated by means of a polytropic process between the opening (EVO) and the closing (EVC) of the exhaust valves:

$$RGF = \left(\frac{p_{EVC}}{p_{EVO}}\right)^{1/\kappa} \cdot \frac{V_{EVC}}{V_{EVO}} \tag{18}$$

4.4   Correction Factor

Since the lower calorific value (LCV) for the fuel is known (46.6 MJ/kg), the ideal energy released (Equation 19) in the combustion can be calculated by multiplying this value by the fuel mass burned. Dividing the total heat released by the ideal one, a **correction factor is estimated** (Equation 20):

$$Q_{bi} = m_{fuel} \cdot LCV \tag{19}$$

$$c_e = \frac{Q_{b\ max}}{Q_{bi}} \tag{20}$$

This **correction factor collects all the differences between the ideal case and the real one**. Mainly, this difference relies on the apparent heat released law that has been calculated. That law estimates the wall heat transfer through the polytropic index. However, the correction factor also includes other effects such as the non-ideally burned of the total mass, the leaks that can happen during the expansion and compression processes and the consideration of the mixture as an ideal gas with constant properties.

In Figure 33, the correction factor values obtained for each set of the characterization data are shown.
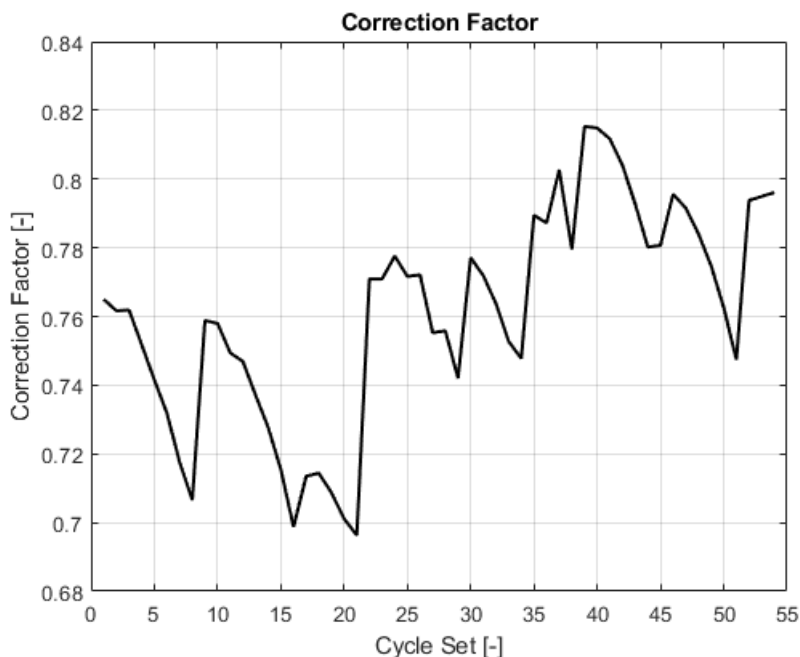

FIGURE 33: Correction factor values for each characterization data set.

The analysis made on this chapter is enough for a later calibration of both the model and the correction factor of the engine combustion. Besides, the experimental in-cylinder pressure and the mass fraction burned will be used to compare results and validate the model.

5   Combustion Model Description

The combustion model developed in this thesis consists of a **quasi-stationary two-zone physic-based turbulent entrainment combustion model** [7], in which the laminar flame speed (S_l) and the turbulence intensity (u') control the combustion and predict the mass fraction burned. In this chapter, different aspects of the model are discussed.

5.1   Turbulence Entrainment and Burn-up Model

The model proposes that the **unburned gas at the flame front is entrained into small eddies due to the turbulence intensity and the laminar flame speed, so they can be burned up inside the flame front in a characteristic time** (τ). Two differential equations are used to represent the entrained mass and the burned mass evolution:

$$\frac{\mathrm{d}m_e}{\mathrm{d}t} \;=\; \rho_{ub} \cdot A_f \cdot (u' + S_l) \tag{21}$$

$$\frac{\mathrm{d}m_b}{\mathrm{d}t} \;=\; \frac{m_e - m_b}{\tau} + \rho_{ub} \cdot A_f \cdot S_l \tag{22}$$

The evolution of the entrainment and the burned mass ratio during combustion are shown in Figure 34.
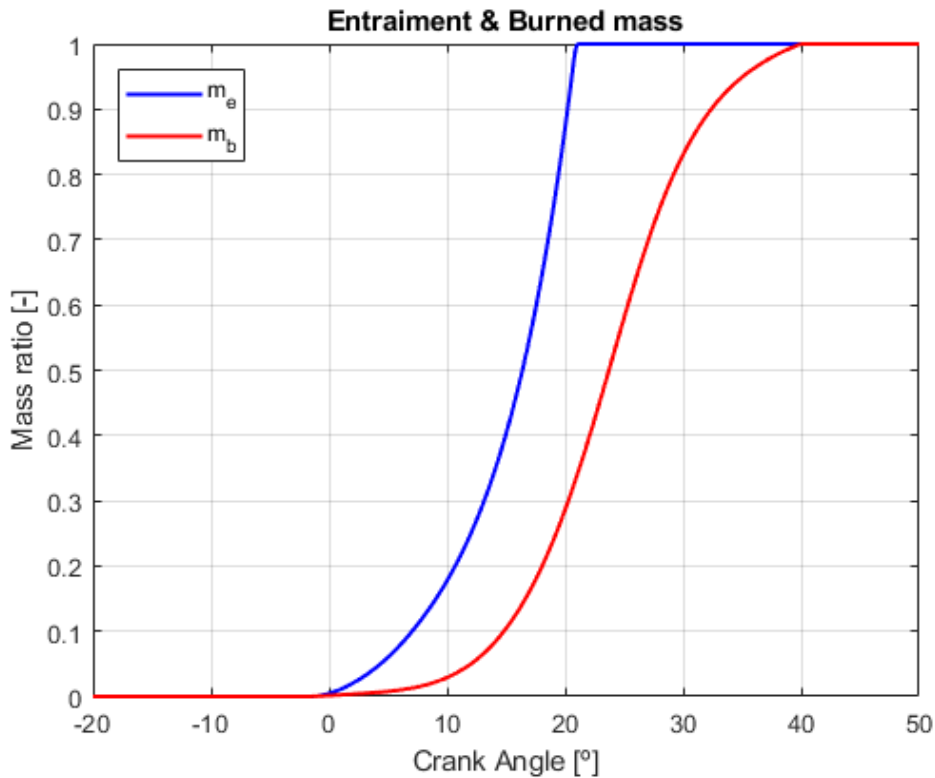
FIGURE 34: Entrainment and burned mass ratio evolution.

The entrainment mass ratio equation (Eq. 21) is governed by two terms. The first one includes the turbulence intensity (u'). The other one deals with the laminar speed (S_l). Both of them are multiplied by the unburned gas density (ρ_{ub}) and by the flame front area (A_f).

In Figure 35, it can be seen that the **laminar flame speed** value (blue line) is relatively high at the SOC and it increases to the maximum value at around the top dead center while it decreases during the expansion stroke. **Turbulence intensity** (red line) begins with a relatively low value and it increases with combustion progress. Nevertheless, **turbulence intensity is one order of magnitude higher than the laminar flame speed**. These results suggest that the turbulence intensity influences the MFB curve slope mainly during rapid burning while the laminar flame speed influences the early combustion stage.
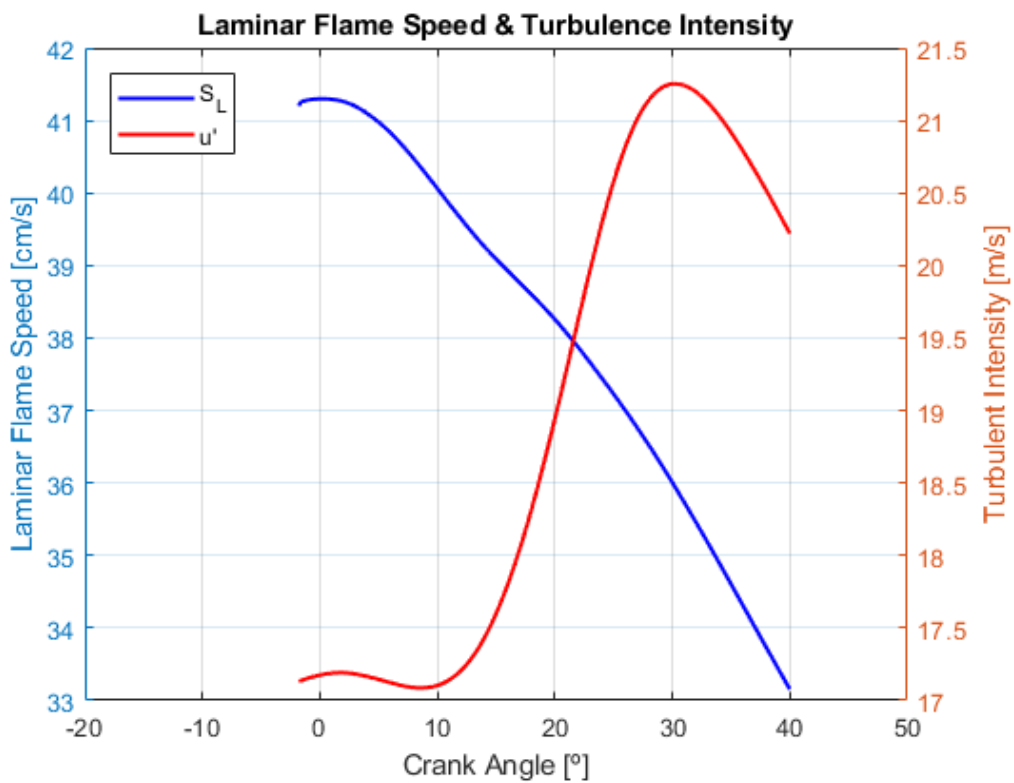
FIGURE 35: Laminar flame speed and turbulence intensity evolution.

The burned mass rate equation (Eq. 22) has also two terms. The first one is a ratio between the mass that has already been entrained into the flame front but has not been burned yet, and the characteristic time (τ) that takes to burn-up an eddy at a laminar flame speed. The second term includes the laminar flame speed multiplied by the unburned gas density and by the flame front area.

In Figure 36, both terms are shown. The first one is the **characteristic time term** (blue line) which has higher importance as long as the difference between the entrained mass and the burned mass increases (first and second combustion stages). The other one is the **laminar flame speed term** (red line) which has more importance at the final stage of the combustion. Thus, despite the laminar flame speed decreases at this point, both the flame

front area and the unburned gas density have greater values compared to the ones at the beginning of the combustion [4].
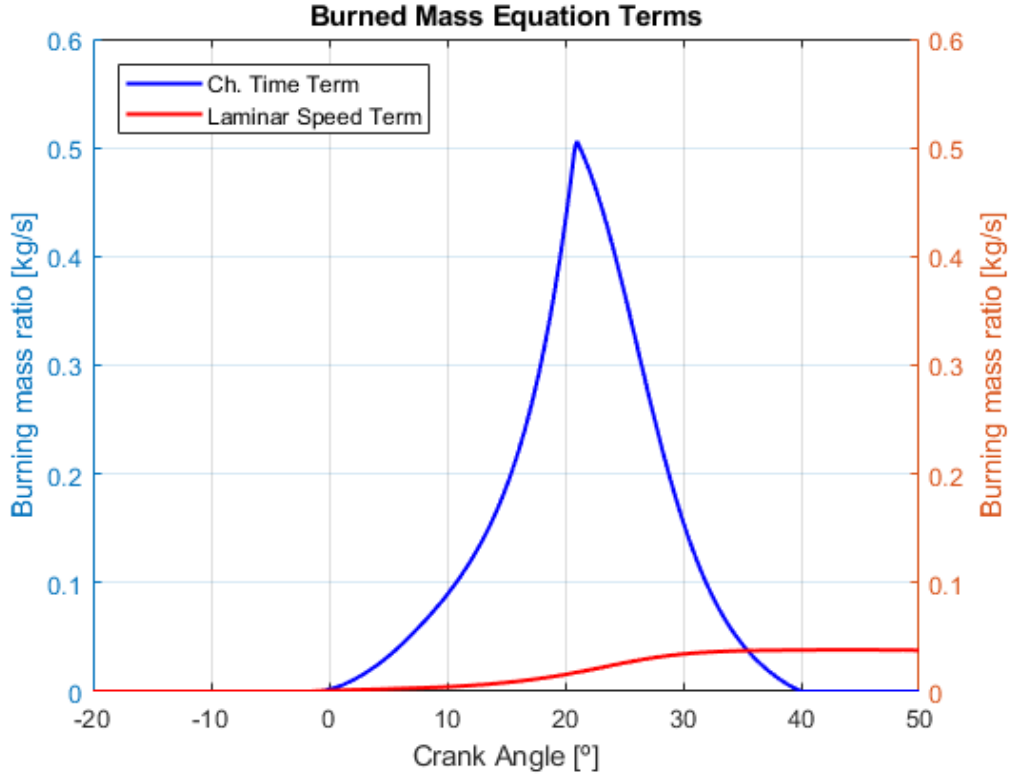

FIGURE 36: Characteristic time and laminar flame speed terms evolution.

5.2   Main Combustion Variables

There are **three parameters that have a significant influence in this model**. All of them have a calibration constant that needs to be fitted. These parameters are the following:

- **The laminar flame speed** (S_l) is defined as the relative velocity with which the unburned gas moves perpendicularly into the flame front. It is a function of thermo-dynamic properties (pressure and temperature), the air-to-fuel ratio (λ), the residual gas fraction (RGF) and fuel properties. In this model, the semi-physics-based Equation 23 has been used:

$$S_l \; = \; C_1 \cdot S_{l0} \cdot \left(\frac{T_{ub}}{T_0}\right)^{\alpha} \cdot \left(\frac{p}{p_0}\right)^{\beta} \cdot (1 - 2.06 \cdot RGF^{0.77}) \tag{23}$$

where p_0 and T_0 are the **intake pressure and temperature** and C_1 is an **adjustable constant**. The **initial flame speed** (S_{l0}) and the coefficients α and β are shown in Equation 24. These parameters depend on fuel properties. For gasoline, its values

have been collected in Table 7.

$$
\begin{aligned}
S_{l0} &= B_m + B_\lambda \cdot (\lambda - \lambda_m)^2 \\
\alpha &= 2.4 - 0.271 \cdot \lambda^{3.51} \\
\beta &= -0.357 + 0.14 \cdot \lambda^{2.77}
\end{aligned}
\tag{24}
$$

Fuel Parameter	B_m [cm/s]	B_λ [cm/s]	λ_m [-]
Gasoline Value	30.5	-54.9	1.21

TABLE 7: Parameter values for gasoline as fuel.

As it has been shown before, this parameter is important at the first and last stages of the combustion. At the final stage, it is specially relevant since the laminar flame speed term is higher than the characteristic time term.

- **The turbulence intensity** (u') is defined as the in-cylinder root-mean-squared velocity fluctuation. It is considered the main component of flame propagation speed with a significant influence on the gas entrainment. Therefore, it is the main component of the rapid burning through the rise of the combustion characteristic time term.

The turbulent flow is assumed to be isotropic in the engine combustion chamber and depends on the unburned mass density after ignition. Equation 26 is derived from the conservation of angular momentum (Equation 25) where the integral length scale (L_{int}) is expressed as function of the unburned mass density (ρ_{ub}).

$$
L_{int} = L_{int_0} \cdot \left(\frac{\rho_{ub}}{\rho_{ub_0}} \right)^{1/3}
\tag{25}
$$

$$
u' = u'_0 \cdot \left(\frac{\rho_{ub}}{\rho_{ub_0}} \right)^{1/3}
\tag{26}
$$

The **turbulent intensity at the beginning of the combustion** (u'_0) is assumed to be proportional to the **mean piston speed** (u_p) and the ratio between the unburned mass density at the beginning of the combustion (ρ_{ub0}) and the mass density of the inlet gas after intake valve closing (IVC). To provide flexibility, the **parameter C_2 is adjustable** for model calibration:

$$
u'_0 = C_2 \cdot u_p \cdot \left(\frac{\rho_{ub0}}{\rho_{in}} \right)^{1/2}
\tag{27}
$$

- **The characteristic burn-up time** (τ) is defined as the time taken to burn-up an eddy at the laminar flame speed (Equation 28). The eddy size is assumed to be the **Taylor microscale** (l_m), which is calculated in Equation 29:

$$\tau = \frac{l_m}{S_l} \tag{28}$$

$$l_m = C_3 \cdot \sqrt{\frac{\mu \cdot L_{int}}{u' \cdot \rho_{ub}}} \tag{29}$$

where C_3 is an **adjustable constant**, μ the **dynamic viscosity** that can be calculated from Equation 30 and L_{int} represents the **integral length scale** during the burn-up process. Before ignition, this length is typically taken as the instantaneous chamber height (h_c). However, during combustion this parameter has to be modified with density ratios between the start and its value during combustion. This caused by the unburned gas compression induced by the burned zone expansion that affects both the turbulence and the integral length scale (Equation 31).

$$\mu = 3.3 \cdot 10^{-7} \cdot T_{ub}{}^{0.7} \tag{30}$$

$$L_{int} = h_c \cdot \left(\frac{\rho_{ub0}}{\rho_{ub}} \right)^{1/3} \tag{31}$$

The influence of this parameter is also found in the characteristic time term of the combustion. The larger the eddy size gets, the lower the burning ratio term will be, giving more importance to the laminar flame speed term [4].

5.3   Flame Geometry

This section is focused on how the flame evolution inside the combustion chamber is modelled after ignition. It is assumed that **the flame spreads spherically from the spark-plug located at the combustion chamber top center**. Burned radius (r_b) and flame front area (A_f), Equations 32 and 33, can be calculated from the semi-sphere volume (V_b) equation:

$$r_b = \left(\frac{3}{2} \cdot V_b \cdot \pi \right)^{1/3} \tag{32}$$

$$A_f = 2 \cdot \pi \cdot r_b^2 \tag{33}$$

At the point where the burned semi-sphere contact the cylinder walls and/or the piston and is cut (Figure 37), burned radius and flame front area are calculated from Equations 34 and 35. The instantaneous chamber height (h_c) is used to adapt the Equations 32 and 33 [4]:

$$r_b = \sqrt{\frac{V_b + \pi \cdot \dfrac{h_c^{\,3}}{3}}{\pi \cdot h_c}} \tag{34}$$

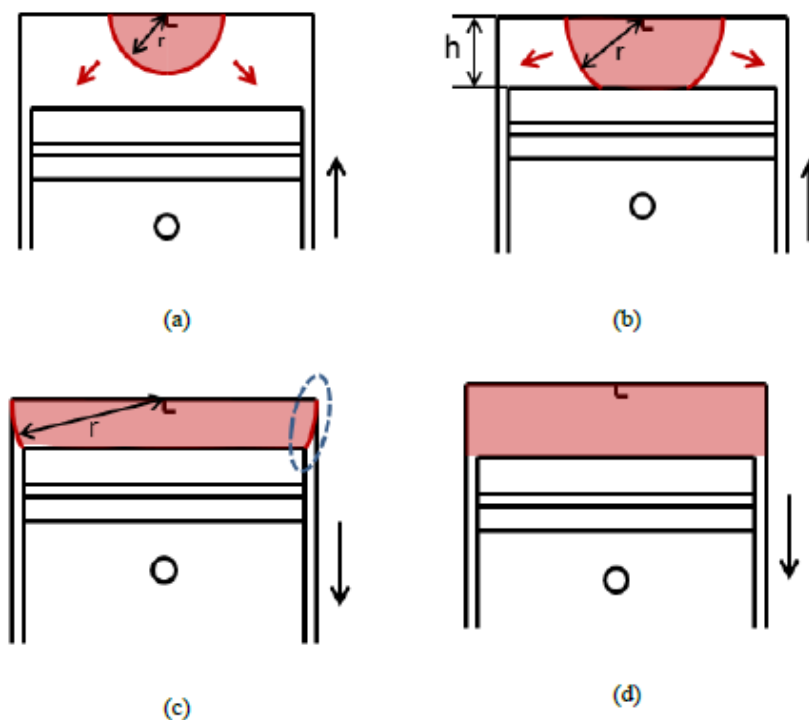$$A_f = 2 \cdot \pi \cdot r_b \cdot h_c \tag{35}$$

FIGURE 37: Flame evolution from combustion chamber top center [4].

5.4   Model Implementation

Thermodynamic variables in the two zones of the combustion chamber need to be determined in order to implement the model. For each crank angle, from the start of combustion to the end, **all variables are required in order to calculate next time step**.

Combustion model inputs needed are: air/fuel mass (m_{air}/m_{fuel}), air-to-fuel ratio (λ), engine speed (n), cylinder intake pressure (p_0) and spark advance (SA). **From intake valve closing to ignition, thermodynamic variables are obtained from the adiabatic process of an enclosed ideal gas** (Equations 36 to 41).

$$p = p_0 \cdot \left(\frac{V_0}{V} \right)^{\kappa} \tag{36}$$

$$\rho = \frac{m}{V} \tag{37}$$

$$T = \frac{p}{\rho \cdot R} \tag{38}$$

$$\lambda = \frac{1/14.6}{m_{fuel}/m_{air}} \tag{39}$$

$$V = V_{cc} + V_{cyl} \tag{40}$$

$$m_{tot} = \frac{m_{air} + m_{fuel}}{1 - RGF} = m_{fuel} \cdot \frac{1 + 14.6 \cdot \lambda}{1 - RGF} \tag{41}$$

where p_0 and V_0 are the **intake pressure and volume**, V is the **instantaneous chamber volume as a function of the crank angle**, R is the **ideal gas constant** (287 J/kg) and m_{tot} is the **total mass inside the cylinder**. The residual gas fraction (RGF) estimation will be discussed in section 5.8.

5.5   Ignition

First, **the ignition point must be established**. It is known that it exists a delay since the spark goes off until the combustion begins. However, for the combustion model, the lack of information hinders the estimation of the ignition point. Therefore and for simplicity, **the spark advance input value will be considered as the start of combustion**.

Nevertheless, the initial burned radio (r_{b_0}) is ignored and must be determined. This value influences significantly the flame front evolution. The bigger the initial value, the shorter the first combustion stage (as well as the total combustion duration).

Besides, the initial burned radio depends on both the local air-to-fuel ratio at the sparkplug and the local turbulence. Therefore, its value varies from cycle-to-cycle and is hard to estimate. After an experimental data study, **the initial burned radio was taken as a constant of value 0.5 mm for the model implementation**.

Once the initial burned radio is selected, **burned (V_b) and unburned (V_{ub}) volumes** can be calculated from Equations 42 and 43:

$$V_b = \frac{2}{3} \cdot \pi \cdot r_b^{\;3} \tag{42}$$

$$V_{ub} = V - V_b \tag{43}$$

Burned mass (m_b), unburned mass (m_{ub}) and unburned density (ρ_{ub}) values are obtained by solving the linear equation system formed by Equations 44, 45 and 46. Equation 44, according to Heywood, determines that the unburned gas density is approximately four time that of the burned gas [8]:

$$\rho_{ub} = \frac{m_{tot} + 3 \cdot m_b}{V} \tag{44}$$

$$m_{ub} = m - m_b \tag{45}$$

$$m_{ub} = \frac{\rho_{ub}}{V_{ub}} \tag{46}$$

The **instantaneous heat released** (Q_b) is obtained from the instantaneous fuel burned mass (m_b) and its lower calorific value (46.6 MJ/kg) multiplied by the combustion corrector factor (Equation 47). The determination of the combustion correction factor value for the model is discussed in section 5.7.

$$Q_b(t) = (m_{b\ fuel}(t) - m_{b\ fuel}(t-1)) \cdot 46 \cdot 10^6 \cdot c_e \tag{47}$$

The fuel burned mass can be written as a function of the total burned mass through Equation 41. Finally, the instantaneous heat released expression is found in Equation 48:

$$Q_b(t) = \frac{m_b(t) - m_b(t-1)}{1 + 14.6 \cdot \lambda} \cdot (1 - RGF) \cdot 46 \cdot 10^6 \cdot c_e \tag{48}$$

At ignition time, **pressure** can be obtained discretizing and solving Equation 11. The resulting pressure equation is shown in Equation 49.

$$p(t) = p(t-1) + \frac{Q_b(t) - p(t-1) \cdot (V(t) - V(t-1)) \cdot \frac{\kappa}{\kappa - 1}}{V(t-1)} \cdot (\kappa - 1) \tag{49}$$

The unburned gas temperature is extracted from the ideal gas law (Equation 38). **The flame front area** and **the dynamic viscosity** are found from Equations 32 and 30, respectively.

With all the previous parameters, **the laminar flame speed** (Equation 23), **the turbulence intensity** (Equation 26) and **the Taylor microscale** (Equation 29) are calculated at ignition time.

Finally, all variables and parameters are calculated at the ignition point. From this values, the combustion process can be solved at each time step.

5.6   Combustion Process

After all combustion parameters at ignition point are determined, the **combustion process can be solved discretizing the model differential equations for each time-step** (Equations 21 and 22). Hence, the instantaneous entrained and burned mass values are calculated for each 0.2 crank angle degrees.

Once the burned mass values has been computed, the **instantaneous heat released** is obtained from Equation 48. Then, from Equation 49, **pressure** is also calculated.

The unburned mass value is extracted from Equation 45. After that, **unburned gas density** is obtained, according to Heywood, from Equation 44 and **unburned gas volume** from Equation 46. At this point, the **burned gas volume** is calculated from Equation 43.

Once the burned volume has been calculated, **the burned radio value** and the **flame front area** are obtained as it is exposed in section 5.3.

Unburned gas temperature is obtained from the ideal gas law (Equation 38) and then, **dynamic viscosity** is calculated from Equation 30.

Finally, **laminar flame speed** (Equation 23), **turbulence intensity** (Equation 26) and **Taylor microscale** (Equation 29) are required for next combustion time step.

This combustion process ends up when the burned mass equals the total mass. After this point, **the rest of the engine cycle can be solved again by means of the adiabatic process of an enclosed ideal gas**. This process has been deeply explained in section 5.4.

5.7   Correction Factor

As it has been seen in section 4.4, the **correction factor collects the effects of different physic phenomena and hypothesis**. These effects produce a difference in each cycle between the ideal energy released by the fuel burning and the real heat released at the combustion.

This correction factor has been **modelled as a function of the engine speed, intake pressure and spark advance** by means of programmed charts. These charts return acceptable correction factor values for each set. In Figure 38, the comparison between the model values and the experimental ones is shown.

However, some differences are observed in Figure 38 between the experimental and model correction factor values. These differences introduced by the correction factor model will lead to an error in the combustion model results (both the in-cylinder pressure evolution and the mass fraction burned).
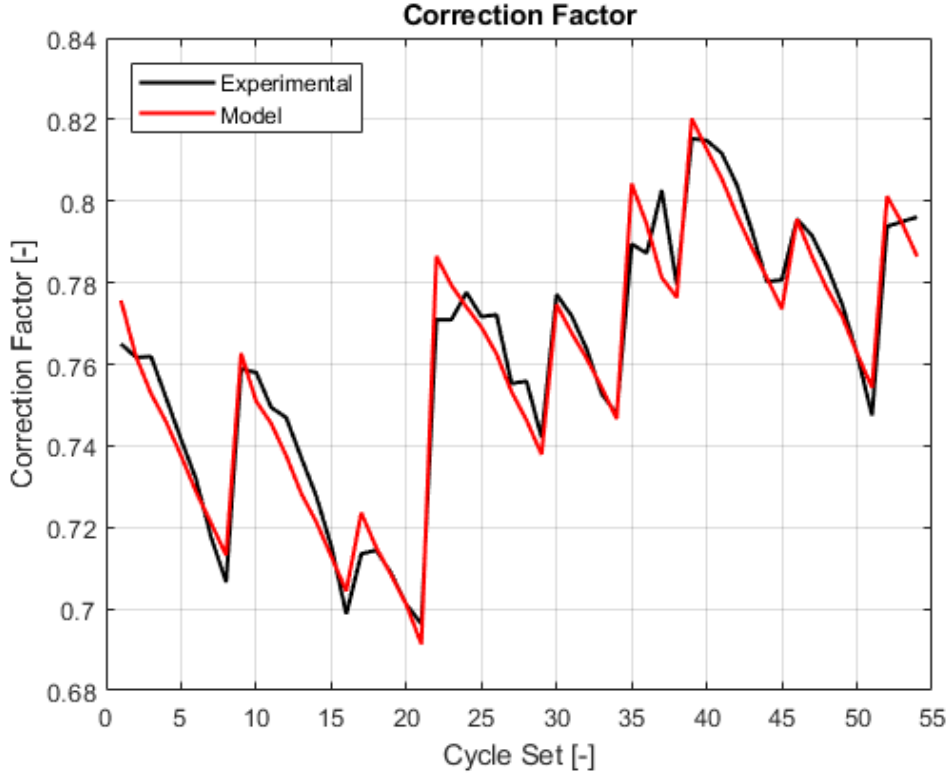
FIGURE 38: Experimental and modelled correction factor.

5.8   Residual Gas Fraction

Once the in-cylinder pressure evolution is obtained, the correspondent residual gas fraction (RGF) is calculated via Equation 18. This RGF value is used in order to calculate in-cylinder pressure evolution on next cycle and so on.

However, for the first cycle of a set, the residual gas fraction is unknown and has to be determined. After a research from experimental data, **a reasonable value of 0.04 was taken** for each set, regardless of the input parameters.

5.9   Constants Calibration

Constants C_1, C_2 and C_3 need to be calibrated in order to secure a proper value for the laminar flame speed, turbulence intensity and Taylor microscale.

The fitting process is made by means of a least-squares adjustment of the error between the experimental heat released curve and the model heat released one. Model C_1, C_2 and C_3 constants are the variables to fit. **Then, these constant values are attempted to be modelled with the input parameters** (speed engine, intake pressure, spark advance, lambda and fuel mass).

Firstly, the three constants were introduced as variables in the least-squares adjustment. Figure 39 shows the value of the three constant for each set.
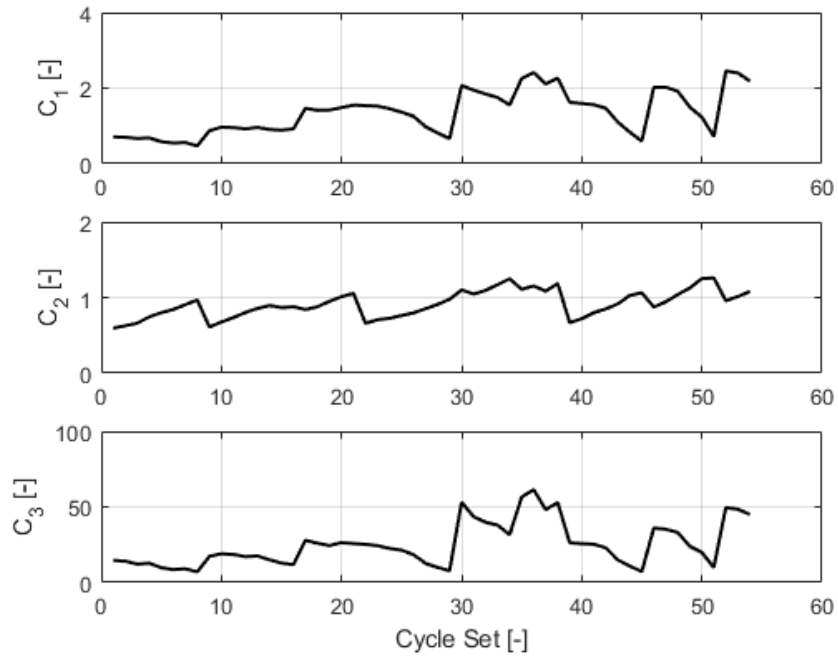
FIGURE 39: Adjusted C_1 C_2 & C_3 values for each set.

In Figure 40, both the experimental data (black line) and model (red line) results corresponding to the MFB (top plots) and in-cylinder pressure curves (bottom plots) are shown. Sets 35 to 38 are selected as example.
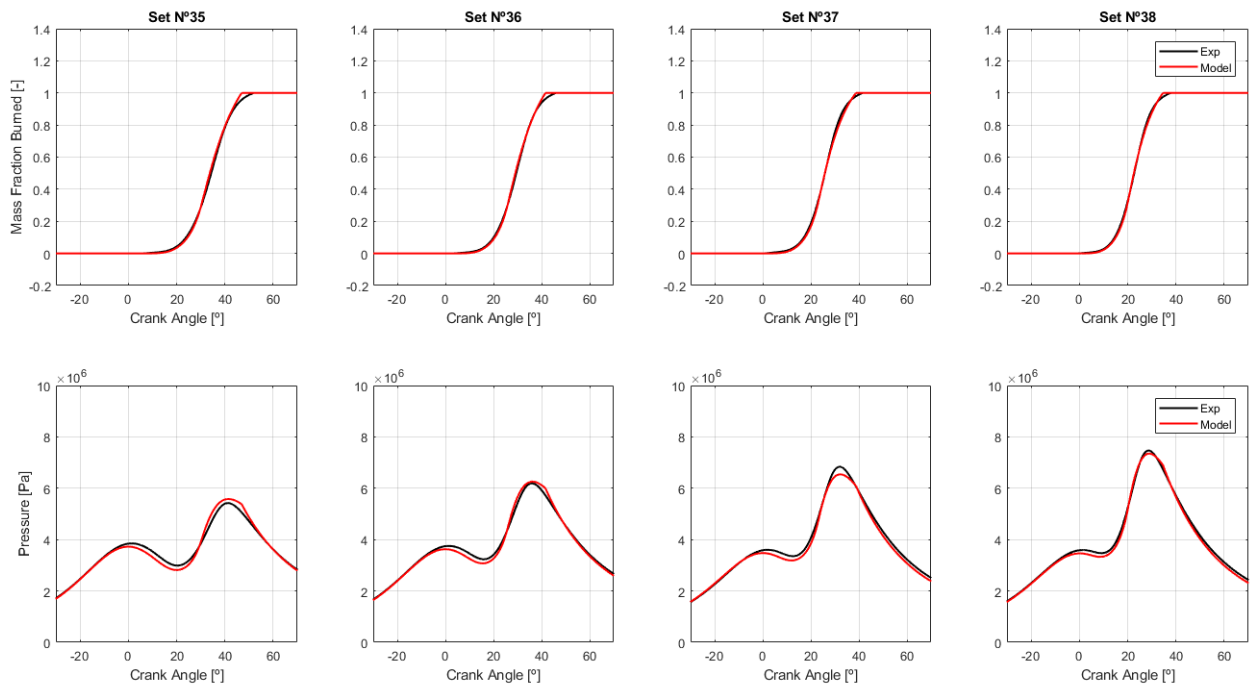
FIGURE 40: MFB and in-cylinder pressure results after C_1, C_2 & C_3 adjustment for sets 35 to 38.

After analysing the results, **two conclusions were extracted**. First, that **at the final part** of the combustion the mass burned ratio is too high and introduces an **abrupt change on the MFB slope**. Second, that the constants C_1 and C_3 have a similar fitted profile and the **system may be overfitted**.

In order to improve this first adjustment, the constants effect on the MFB curve was brought up. Each one of them are directly proportional to the laminar flame speed, turbulence intensity and Taylor microscale, respectively. These three parameters were presented at section 5.2 where their influences in the combustion were described. These influences can be extrapolated to their respective constants. Summing up which it was exposed:

- C_1 **influences the beginning of the MFB curve and also the final stage**. At this final stage the laminar flame speed term of the mass burned ratio is higher than the characteristic time term.

- C_2 **has a significant influence** on the gas entrainment. Therefore, it is the main component of the rapid burning due to the increase of the characteristic time term. This influence corresponds to the **first and second stage of the MFB curve**.

- C_3 influence it is also found on the characteristic time term of the combustion. The larger the eddy size gets, the lower the burning ratio term will be and vice versa. This gives more (or less) importance to the laminar flame speed term. Therefore, C_3 **affects both the second and third stage of the MFB curve**.

After this study, it seems reasonable to fix the value of C_3 constant for every set, letting that the C_1 and C_2 fitting compensates the effects on the MFB and in-cylinder pressure curves.

The value selected for the C_3 constant is 10. This value is low enough to give less importance to the laminar flame speed term at the end of the combustion, avoiding the abrupt slope change in the MFB curve. However, the value is high enough to keep a good adjustment for the rest of the curve.

Figure 41 shows the three constant values after the new least-squares adjustment. In Figure 42, both the experimental data (black line) and model (red line) results corresponding to the MFB (top plots) and in-cylinder pressure curves (bottom plots) are shown. Sets 35 to 38 are selected as example.

With this fitting process acceptable results were obtained. Next step consists on finding a correlation between the input parameters and the constants adjusted value for each set.

For the C_2 constant case, it was observed that it could be modelled with the engine speed, intake pressure and spark advance by means of programmed charts.
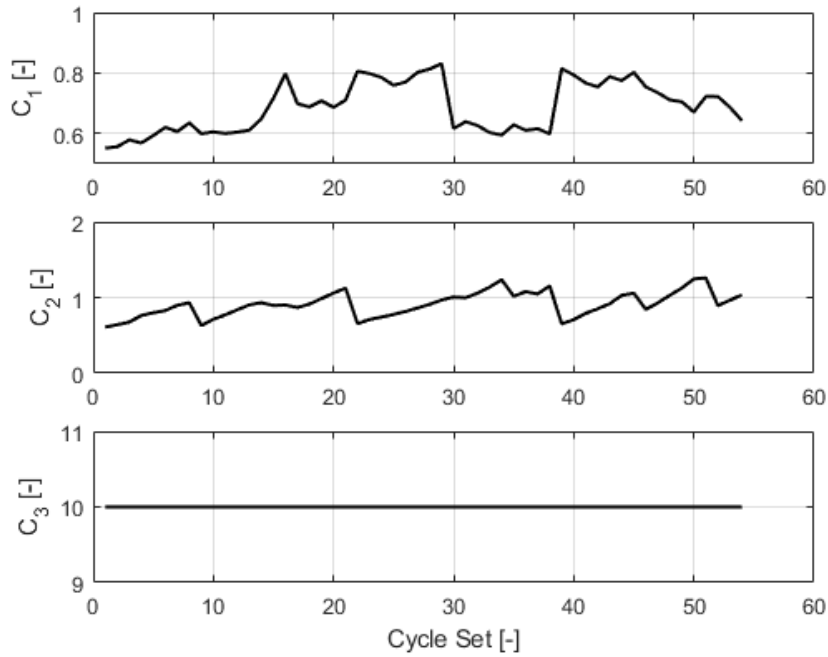
FIGURE 41: C_3 and adjusted C_1 & C_2 values for each set.
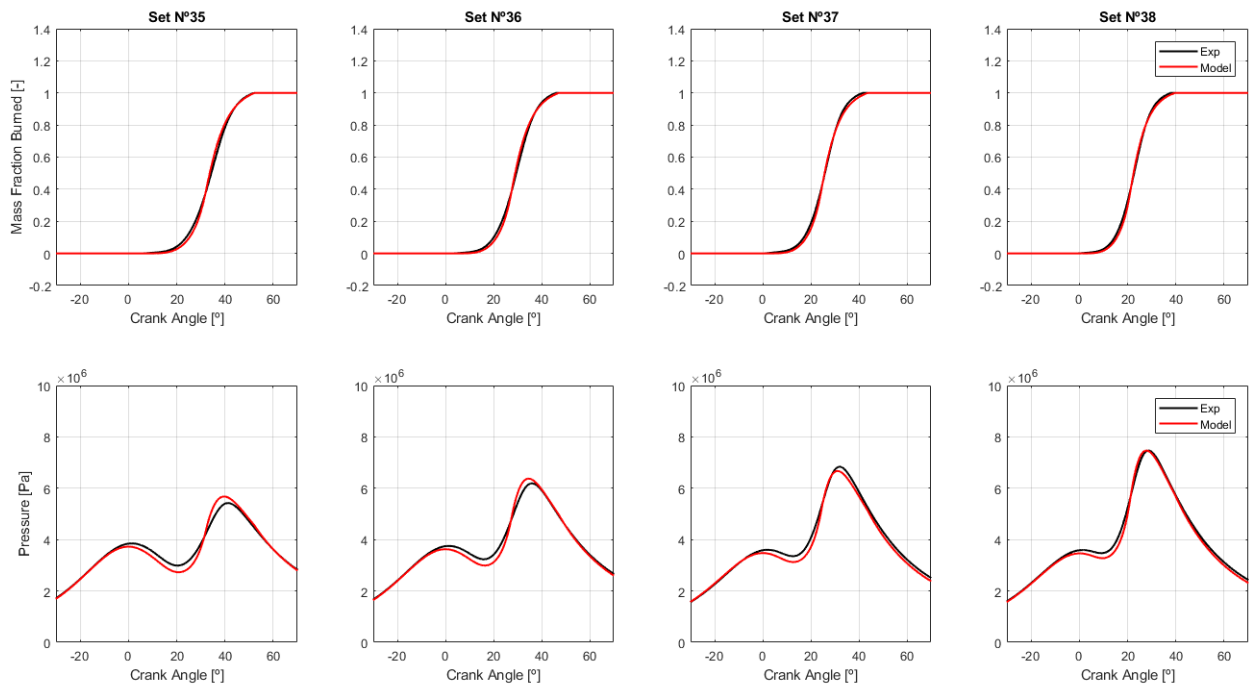
FIGURE 42: MFB and in-cylinder pressure results after C_1 & C_2 adjustment for sets 35 to 38.

However, C_1 constant seems not to depend on either the spark advance or intake pressure. Therefore, it was decided to model C_1 directly proportional to only the engine speed. After that,it is proceeded again with the least-squares adjustment for only C_2.

Figure 43 shows the three constant values after the third least-squares adjustment. In Figure 44, both the experimental data (black line) and model (red line) results corresponding to the MFB (top plots) and in-cylinder pressure curves (bottom plots) are shown. Sets 35 to 38 are selected as example.
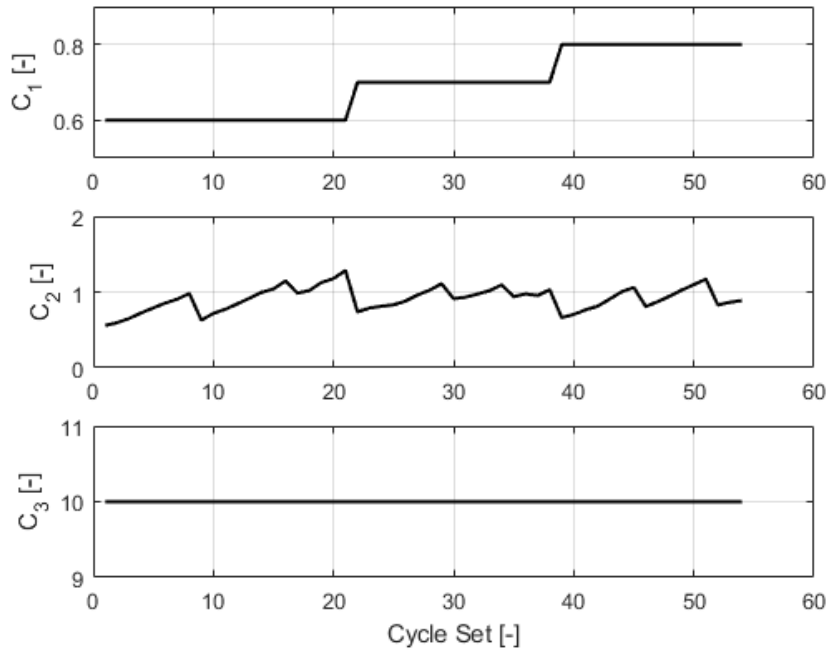

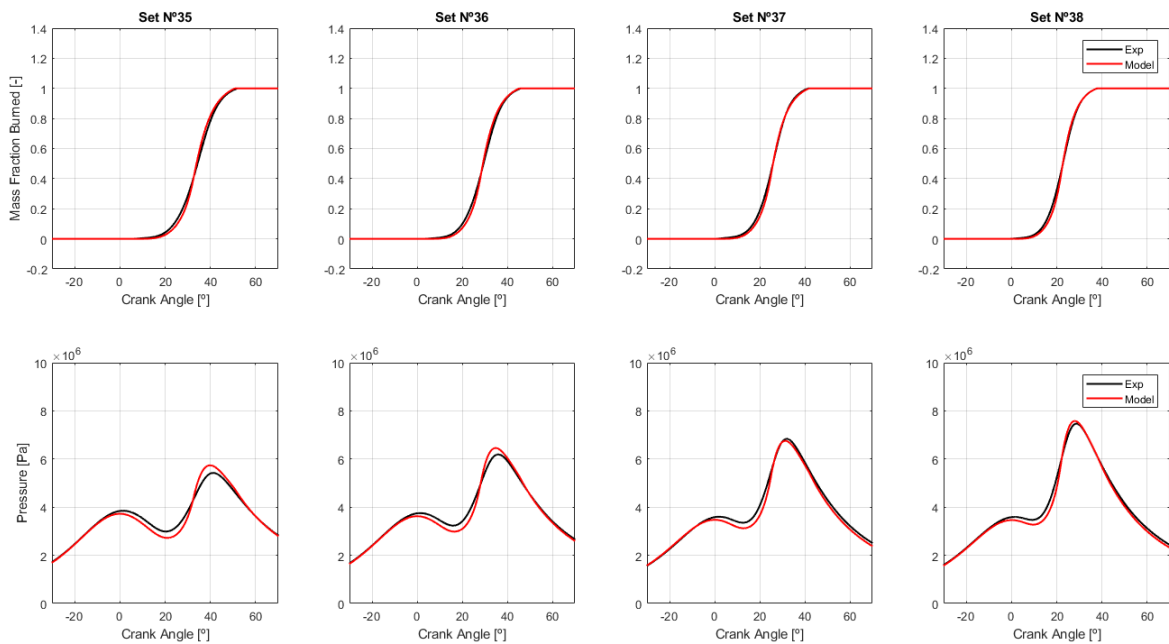FIGURE 43: C_1, C_3 and adjusted C_2 values for each set.

FIGURE 44: MFB and in-cylinder pressure results after C_2 adjustment for sets 35 to 38.

Finally, last step consists on modelling C_2 with the input parameter for each set. As it was observed before, C_2 constant can be modelled properly with the engine speed, intake pressure and spark advance through programmed charts.

The results of this process can be seen in Figure 45 where both the three constant values after the least-squares adjustment and the three modeled values are represented. The results corresponding to of the MFB and in-cylinder pressure curves will be shown in chapter 7.
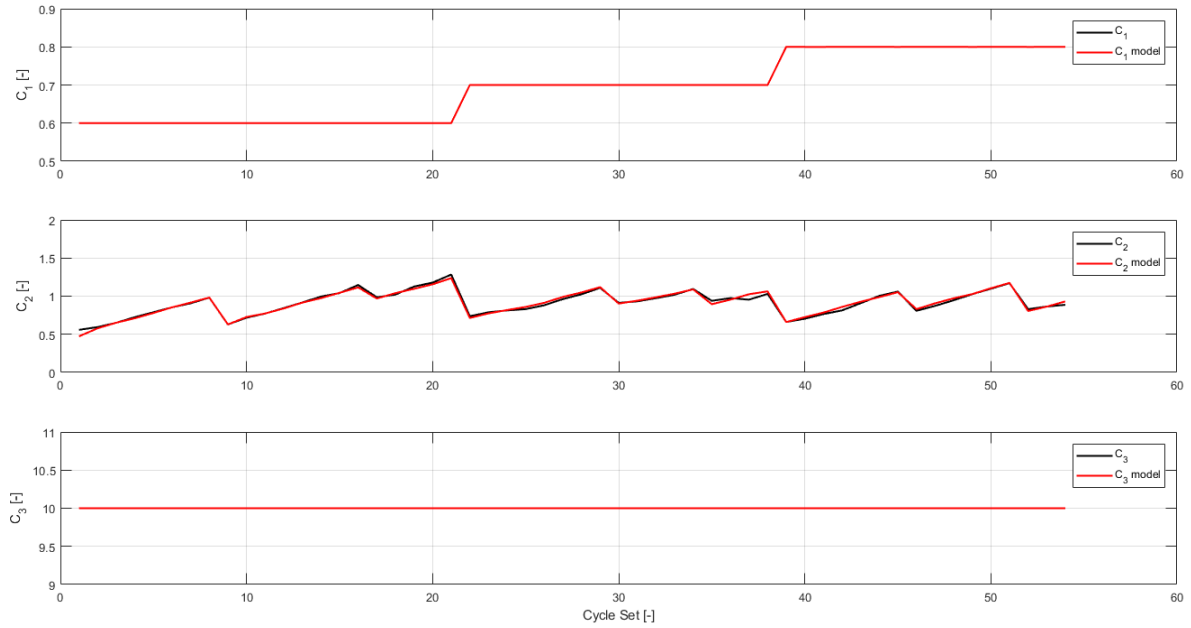

FIGURE 45: Adjusted and modelled constants values for each set.

54

6   Combustion Dispersion Model

An objective set for this master thesis is the **study and modelling of the combustion dispersion phenomenon**. This is a complex phenomenon that requires high amount of data and computational time to be studied [9–11]. Besides, the combustion dispersion modelling is also a devious process [12, 13] which is highlighted in following sections.

6.1   Experimental Data Dispersion Analysis

Combustion dispersion modelling requires a previous analysis from experimental data in order to extract information for the model. The first step consists on **analyzing experimental data** (as explained in chapter 4) **for each cycle** instead of for the mean value on each set. The mass fraction burned is obtained for a representative number of cycles of the dispersion phenomenon.

In Figure 46, both the **MFB** (left side) **and the in-cylinder pressure curve** (right side) dispersions are shown. In this chapter, set 32 will be taken as example for the graphics.
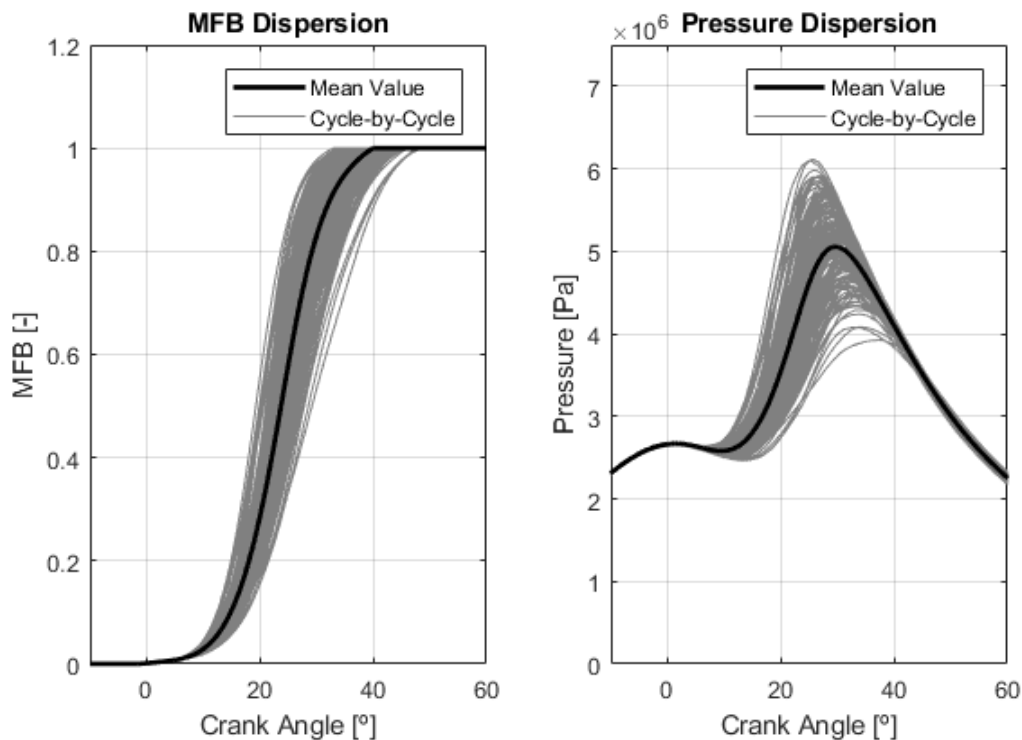

FIGURE 46: MFB and in-cylinder pressure cyclic dispersion for set 32.

From these data, **the crank angle values at 5%, 50% and 95% of the total MFB** were collected on each set for each cycle. These values were **represented on histograms** (Figure 47). Note that a **normal distribution**, defined by a mean and a standard deviation, **can be fitted** at each percentage.

The **procedure to analyse the dispersion is focused on obtaining the standard deviations** of the crank angle values at different percentages of the mass fraction burned
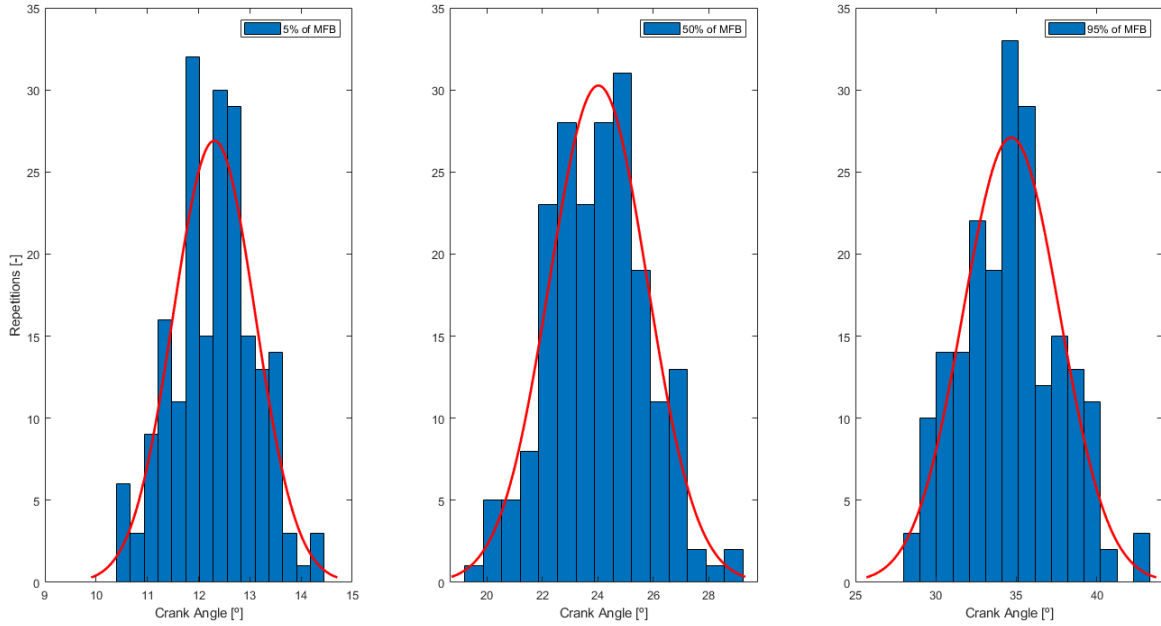
FIGURE 47: Crank angle histograms for 5%, 50% & 95% of the MFB for set 32.

($CAXX$, where XX represents the combustion percentage). The **MFB is divided every 5%** of the total burned mass. However, the from 0 to 5%, the MFB **is divided every 1%** for accuracy. After that, **the standard deviation at each percentage will be calculated**. In Figure 48, the variability curve is shown along the combustion percentage.
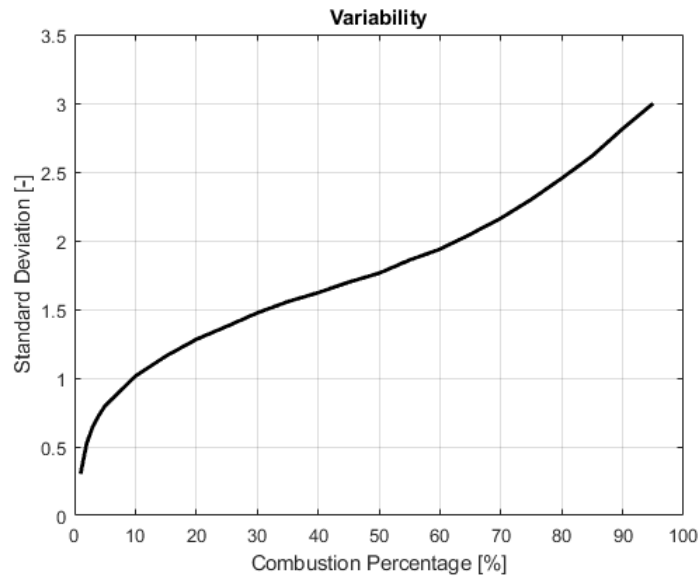

FIGURE 48: Standard deviation at each percentage of burned mass for set 32.

From this study it can be stood out four points. First, it has been observed that the **delay between the spark and the SOC introduces certain variability** as the combustion does not start always at the same point. This can be attributed to both the local turbulence and air-to-fuel ratio near the sparkplug.

Second, the **high variability increase between the SOC and the 15/20% of the combustion** (combustion first stage). This variability is attributed to several effects such as the size of the initial burning radio (flame front area), the flame front turbulence intensity and the entrained eddies size.

Third, between the **20% and the 75/80% of the MFB the dispersion increase is moderated. This corresponds to the fast combustion stage**. The variability increase is lower due to the high combustion dynamics.

Finally, **between the 75/80% and the end of the combustion, the dispersion curve slope increases again. This part corresponds to the final stage of the combustion**. At this stage, the burned mass rate depends mainly on the laminar flame speed that remains at the flame front area. The slow burning increases significantly the variability.

6.2   Combustion Dispersion Model Description

The **model aims to reproduce the behaviour of the combustion** process for a given input variables. That is, not only simulate the mean combustion value, but **also its cycle-to-cycle dispersion**. Due to the random nature of the process, this can't be done cycle-to-cycle strictly. However, the model has to be representative after a certain number of cycles.

The modelling process will be separated into **two different parts**. On the one hand, the **description of the dispersion model** itself by means of the error propagation theory. On the other hand, the **fitting and calibration of the constants standard deviation**.

A **normal distribution is applied for each constant**. The mean is taken from the **values selected in chapter 5** in each set. The standard deviation are the variables to fit. For simplicity, the normal distribution multiplies the constant value, therefore, the mean will be set in 1. The **constants standard deviation reflects a change on the original MFB and in-cylinder pressure curves**. This is how the cycle-by-cycle dispersion phenomenon is represented.

A **simple test on each constant separately was carried out**. In Figure 49, it can be seen the variability at each MFB percentage for a 0.08 standard deviation on each constant at a time. **All cases introduce a rising variability** but **with different slopes**.

Turbulence intensity constant (C_2) generates a linear grow with a higher slope at the first and last combustion stages. Both laminar flame speed and Taylor microscale constants (C_1 and C_3) have similar variability curve slopes with a pronounced change at the last stage. As a conclusion from this study, it was **decided not to include C_3 constant to generate variability**. Only C_1 and C_2 are employed for the dispersion combustion modelling.

The **error propagation theory is applied** in order to model the combustion dispersion. This theory, when a determined standard deviation on each constant is applied, consists on calculate both the mean (μ) and the standard deviation (σ) of the crank angle value at a certain percentage of the combustion for each combination of constants values ($CAXX$) multiplied by the likelihood of this constant combination.
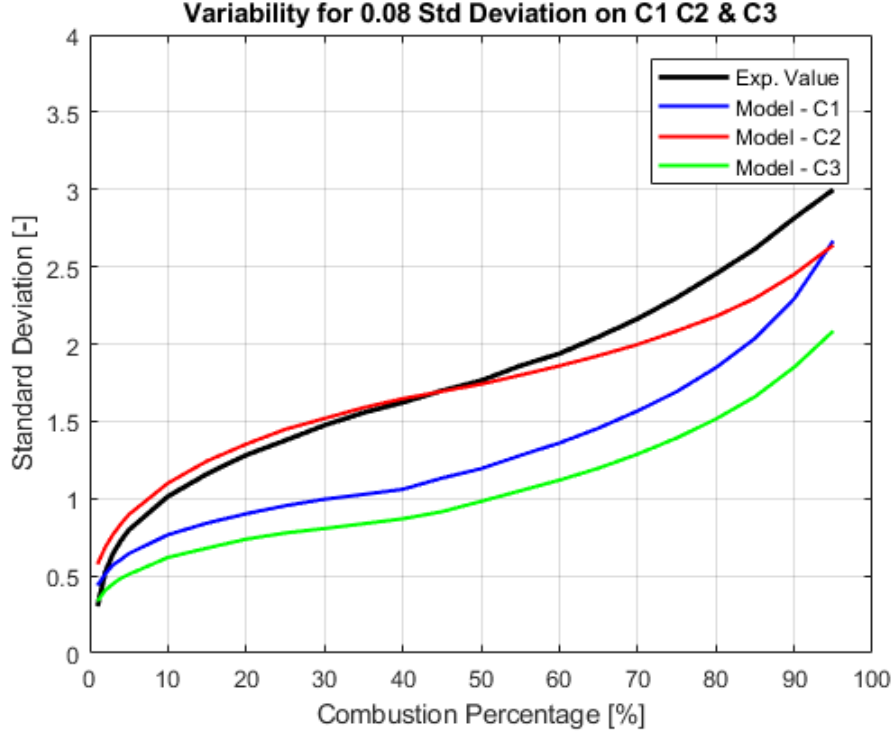
FIGURE 49: Model dispersion for a 0.08 standard deviation on each constant at a time.

The combustion model for each constant combination is ran. The value of the crank angle at each combustion percentage ($CAXX$) is multiplied by the constants combined probability density function ($CPDF$). Finally, for each MFB percentage, the mean and standard deviation of all cases is calculated from Equations 50 and 51, respectively.

$$\mu = \frac{1}{M} \cdot \frac{1}{N} \cdot \sum_{i=1}^{M} \left(\sum_{j=1}^{N} CAXX(i,j) \cdot CPDF(i,j) \right) \tag{50}$$

$$\sigma = \sqrt{\frac{1}{M} \cdot \frac{1}{N} \cdot \sum_{i=1}^{M} \left(\sum_{j=1}^{N} \left(CAXX(i,j) \cdot CPDF(i,j) - \mu \right)^2 \right)} \tag{51}$$

The **combined probability density function** ($CPDF$) gives the matching probability of two values of the constants C_1 and C_2. This is calculated as a combination of the probability density function (PDF) of each constant for given standard deviation, mean and a range of the constant variation.

This **probability density function** (PDF) of a normal distribution will return the likelihood of the constant taking a value from the sample space given. The function units are the inverse of the unit that measure the sample space (C_1 that has no dimension). However, in order to adimensionalize, the probability density function is multiplied by the constant range amplitude. In this case 0.8 since the range has been selected from 0.6 to 1.4.

In Figure 50, it can be seen, as a graphic example, two normalized probability density functions of a normal distribution with mean 1 and standard deviation 0.07 (left side) and 0.09 (right side), respectively. For the example, these are taken for C_1 and C_2 constants.
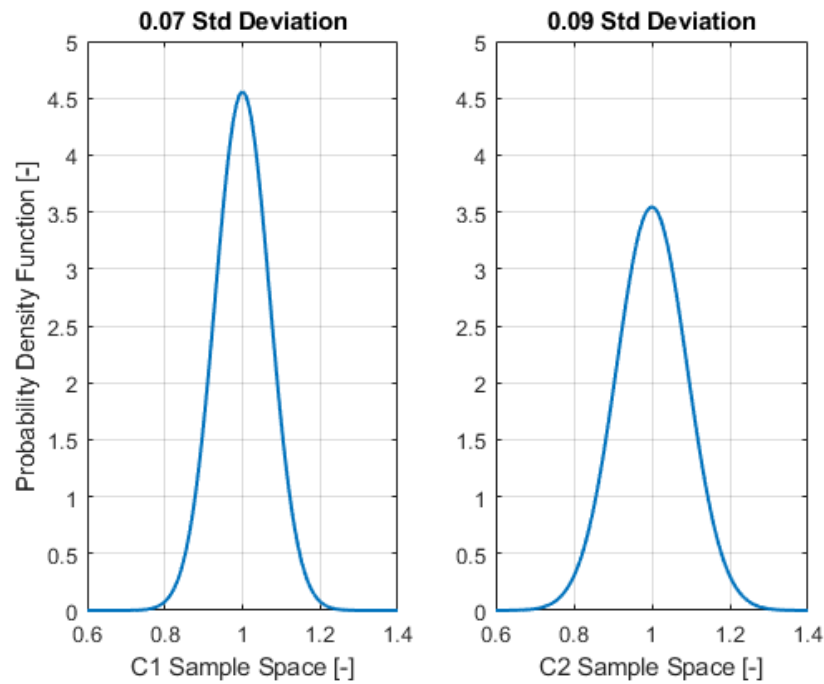

FIGURE 50: Normalized PDFs for 0.07 and 0.09 standard deviations respectively

The **combined probability density function ($CPDF$) is obtained by multiplying the two (PDF)s values in a matrix from**. The representation of the combined probability density function can be seen in Figure 51.
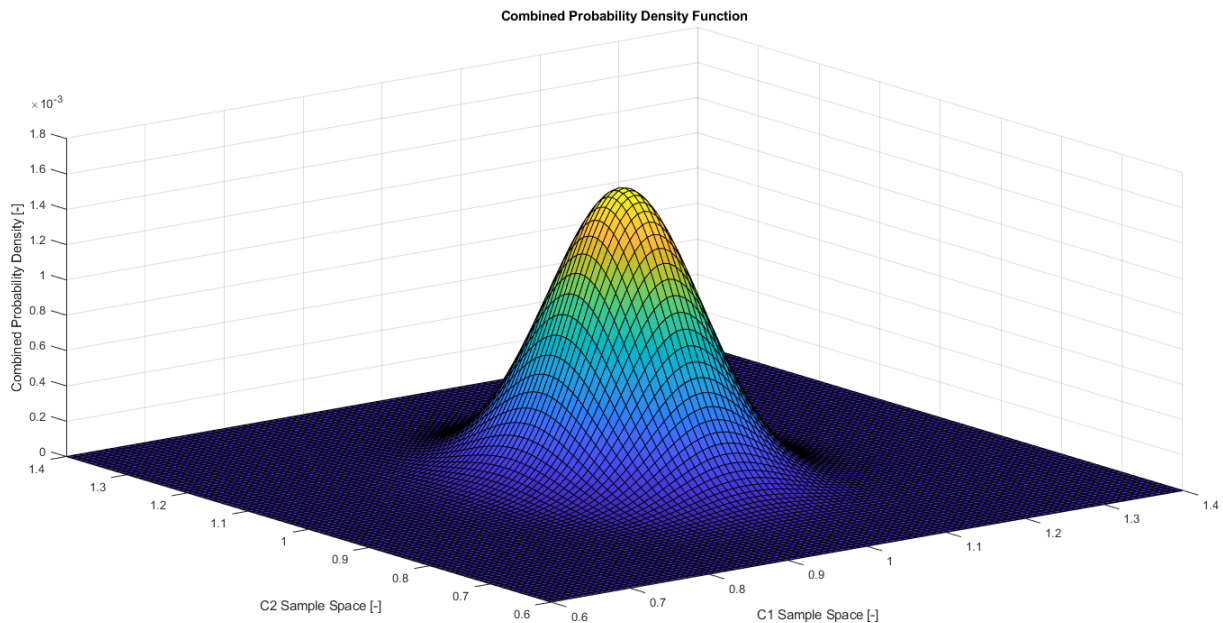

FIGURE 51: Combined PDF for 0.07 and 0.09 standard deviations on C_1 & C_2.

The **crank angle values for each combustion percentage ($CAXX$) at each constant combinations have to be also calculated**. There are 23 different combustion percentages. The sweep made for C_1 and C_2 constants goes from 0.6 to 1.4 with a discretization of 100 in-between values. Note that this generates a matrix of angles of 100x100x23 values. In Figure 52, it is shown, as an example, the angles matrix for the CA50.
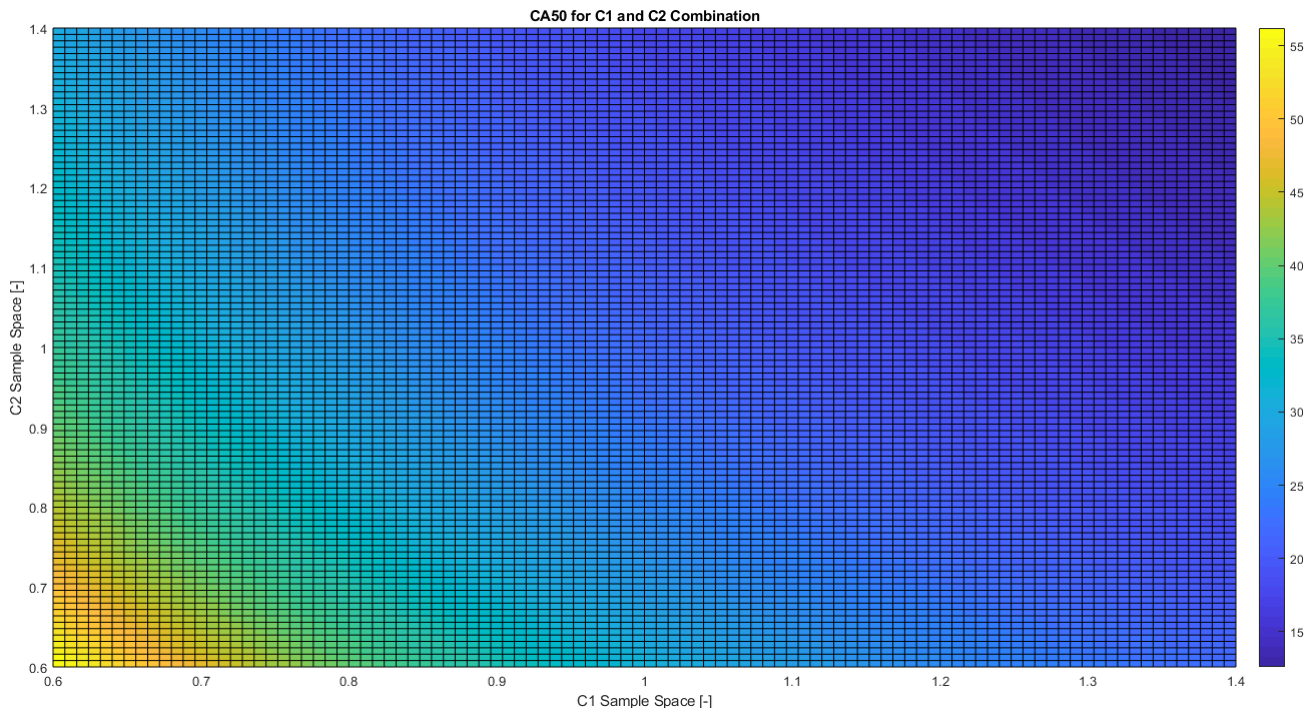

FIGURE 52: Angle matrix at CA50 for C_1 & C_2 combination.

Finally, after all these values are calculated, the standard deviation can be obtained from Equation 51 for each combustion percentage. The variability curve can be drawn and compared to the one get from experimental data. In Figure 53, it can be seen the variability curve obtained from the error theory propagation in set 32 compared to the variability curve obtained from the experimental data.

With this process programmed as a function it can be prepared a **least-squares adjustment between the experimental data variability curve and the dispersion model variability curve**, leaving the standard deviation of the normal distribution that multiplies C_1 and C_2 constant as the parameters to be adjusted.

However, the **computational time that it takes to carry out this process is very high due to the great number of values** of the angles matrix. In order to reduce the computational time, a **simplification for this process** was done.

The simplification is based on the **assumption** that each crank angle combustion percentage ($CAXX$) can be modelled as a quadratic function of the C_1 and C_2 constant variation. In mathematical terms, that **the second derivatives of the crank angle combustion percentage with respect to C_1 and C_2 variations are equal to a constant value** (equations 52 and 53).
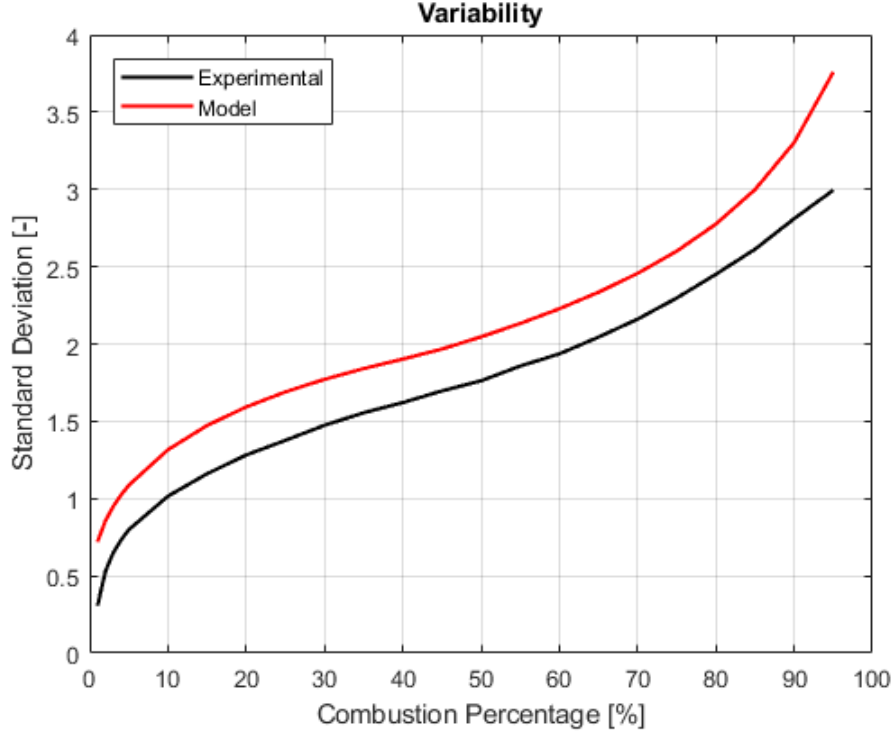
FIGURE 53: Experimental and modelled (0.07 & 0.09 standard deviations on C_1 & C_2) variability curves for set 32.

$$\frac{\mathrm{d}CAXX^2}{\mathrm{d}^2 \Delta C_1} = K_{12} \tag{52}$$

$$\frac{\mathrm{d}CAXX^2}{\mathrm{d}^2 \Delta C_2} = K_{22} \tag{53}$$

After this assumption, each constant sample space does not required to be divided into an equidistant vector of 100 values. **Only three values are needed, selected as 0.8, 1 and 1.2**, to obtain the quadratic equation which interpolates the rest of the crank angle values. Note that now, despite of the loss of information, the size of the matrix has been reduced from 100x100x23 to 3x3x23. In Figure 54, the scheme and notation of the **reduced angle matrix** for each crank angle combustion percentage is shown.

Finally, integrating and combining equations 52 and 53, the **quadratic crank angle expression** is extracted (Equation 54). In this expression K_1, K_{11}, K_{12}, K_{21} and K_{22} are the constants obtained from the integration that can be calculated with the values of $CAXX$ for C_1 and C_2 equal to 0.8, 1 and 1.2.

$$CAXX = K_{12} \cdot \frac{\Delta C_1^2}{2} + K_{11} \cdot \Delta C_1 + K_{22} \cdot \frac{\Delta C_2^2}{2} + K_{21} \cdot \Delta C_2 + K_1 \tag{54}$$
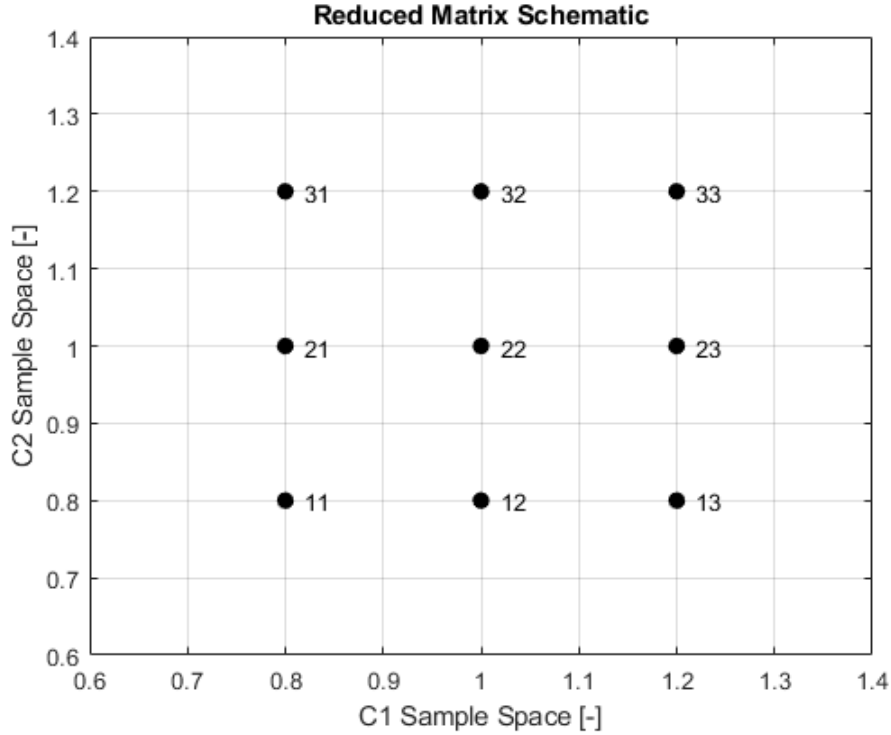
FIGURE 54: Reduced angle matrix scheme and notation for each CAXX.

The equation **variables** (ΔC_1 and ΔC_2) are the **difference between the constant value and the reference one, which have been taken as 1 for both constants**.

K_1 is the **value of CAXX at the reference point**, where both ΔC_1 and ΔC_2 become zero (Equation 55).

$$K_1 = CAXX_{22} \tag{55}$$

K_{11} and K_{21} are the **values of the first derivatives of CAXX with respect to the variation of C_1 and C_2 at the reference point** (Equations 56 and 57), respectively. For accuracy, it will be taken as the mean value between the slope at 0.9 $\left(\frac{\mathrm{d}CAXX}{\mathrm{d}\Delta C_x}\Big|_1\right)$ and the slope at 1.1 $\left(\frac{\mathrm{d}CAXX}{\mathrm{d}\Delta C_x}\Big|_2\right)$ for both constants. The slopes at 0.9 and 1.1 will be calculated from the known values of CAXX for C_1 and C_2 equal to 0.8, 1 and 1.2.

$$K_{11} = \frac{\mathrm{d}CAXX}{\mathrm{d}\Delta C_1}\Big|_{22} = \left(\frac{\mathrm{d}CAXX}{\mathrm{d}\Delta C_1}\Big|_1 + \frac{\mathrm{d}CAXX}{\mathrm{d}\Delta C_1}\Big|_2\right)/2 \tag{56}$$

$$\frac{\mathrm{d}CAXX}{\mathrm{d}\Delta C_1}\Big|_1 = \frac{CAXX_{22} - CAXX_{21}}{1 - 0.8}$$

$$\frac{\mathrm{d}CAXX}{\mathrm{d}\Delta C_1}\Big|_2 = \frac{CAXX_{23} - CAXX_{22}}{1.2 - 1}$$

$$K_{21} = \left.\frac{\mathrm{d}CAXX}{\mathrm{d}\Delta C_2}\right|_{22} = \left(\left.\frac{\mathrm{d}CAXX}{\mathrm{d}\Delta C_2}\right|_1 + \left.\frac{\mathrm{d}CAXX}{\mathrm{d}\Delta C_2}\right|_2\right)/2 \tag{57}$$

$$\left.\frac{\mathrm{d}CAXX}{\mathrm{d}\Delta C_2}\right|_1 = \frac{CAXX_{22} - CAXX_{12}}{1 - 0.8}$$

$$\left.\frac{\mathrm{d}CAXX}{\mathrm{d}\Delta C_2}\right|_2 = \frac{CAXX_{32} - CAXX_{22}}{1.2 - 1}$$

K_{12} and K_{22} are the **values of the second derivatives of CAXX with respect to the variation of C_1 and C_2 at the reference point**, respectively. These constant are calculated again from the known values of CAXX for C_1 and C_2 equal to 0.8, 1 and 1.2.

$$K_{12} = \left.\frac{\mathrm{d}CAXX^2}{\mathrm{d}^2\Delta C_1}\right|_{22} = \left(\left.\frac{\mathrm{d}CAXX}{\mathrm{d}\Delta C_1}\right|_1 - \left.\frac{\mathrm{d}CAXX}{\mathrm{d}\Delta C_1}\right|_2\right)/(1.1 - 0.9) \tag{58}$$

$$K_{22} = \left.\frac{\mathrm{d}CAXX^2}{\mathrm{d}^2\Delta C_2}\right|_{22} = \left(\left.\frac{\mathrm{d}CAXX}{\mathrm{d}\Delta C_2}\right|_1 - \left.\frac{\mathrm{d}CAXX}{\mathrm{d}\Delta C_2}\right|_2\right)/(1.1 - 0.9) \tag{59}$$

Once the simplification is complete, in Figure 55 it can be seen that the results from both combustion dispersion models (simplified and not simplified). These results are quite similar, however the **computational calculus time has been reduced**, which will be very useful for the later least-squares adjustment of the variability curves.
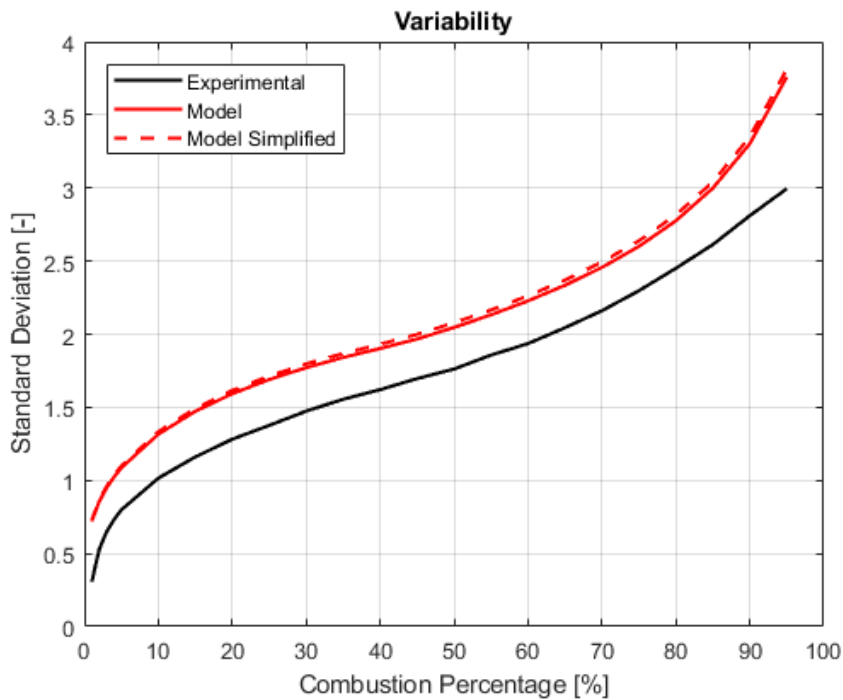

FIGURE 55: Experimental, model and simplified model (0.07 & 0.09 standard deviations on C_1 & C_2) variability curves for set 32.

6.3   Combustion Dispersion Model Adjustment

The **combustion dispersion model fitting is carried out by means of a least-squares adjustment** between the variability experimental data curve and the variability dispersion model curve. These curves represent the crank angle standard deviation values at a certain combustion percentages.

The **parameters to fit are the standard deviation values of the normal distribution that multiplies the constants C_1 and C_2, respectively**. Once the adjustment is complete, it is attempt to **model these standard deviations as a function of the model inputs values** (engine speed, intake pressure, spark advance, lambda or fuel mass).

In Figure 56, the values of the standard deviation from the least-squares adjustment are shown. **It was not found an immediate relation between these values and the inputs parameters**.
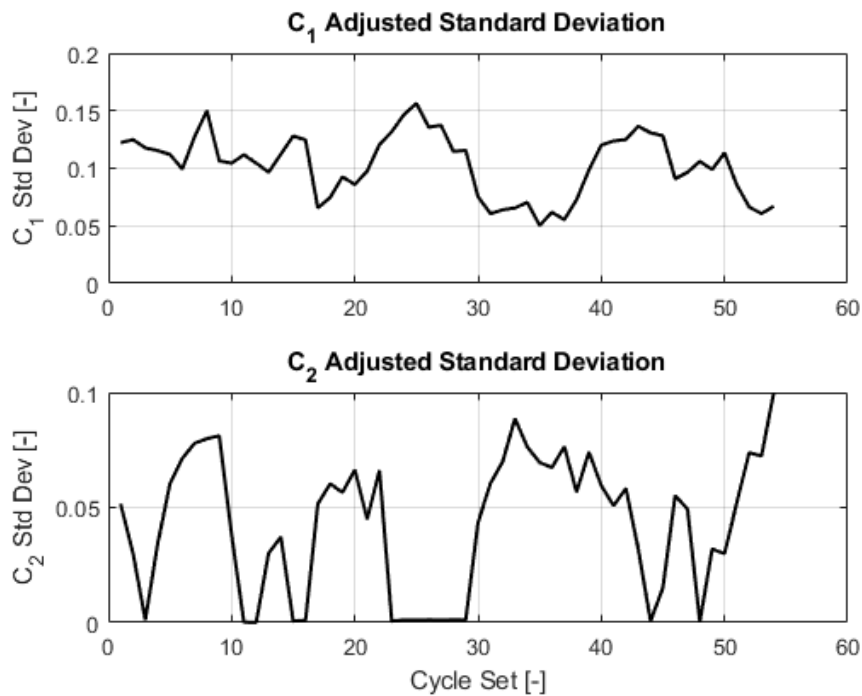
FIGURE 56: C_1 & C_2 standard deviation least squares adjustment.

After a further analysis, it was found reasonable that the variability increases its value as the engine load and speed do. Therefore, it was **decided to model the standard deviations with the engine speed and the intake pressure**. Programmed charts were done for the modelling and the final results are shown in Figure 57.

In **cases where both the engine load and speed combination were not high enough and for high spark advance values**, the variability curve has already a high value when the combustion begins. It was observed that this effect could be cause by the delay between the spark advance and the start of combustion. Therefore, it was **decided to model this behaviour with the spark advance value**. Again, programmed charts were made for the modelling of the initial variability.
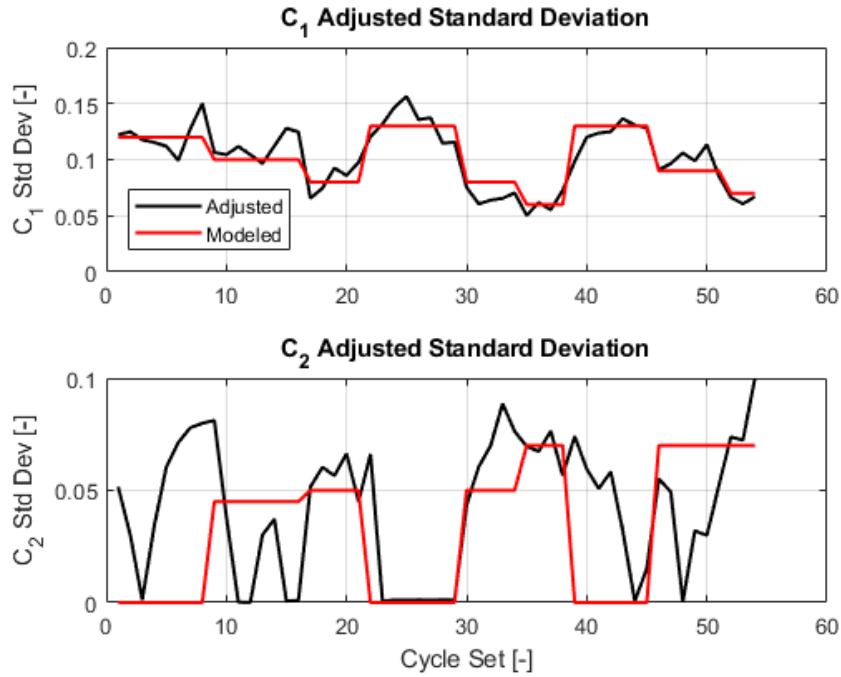
FIGURE 57: Modelled and adjusted modelled C_1 & C_2 standard deviations.

In Figure 58, an **example of this effect is shown**. The MFB curve variability along the combustion results are represented for the experimental data, model and model plus initial variability. The **selected sets were number 15** (left side) **and 16** (right side), **where the engine speed and load are low and the spark advance is high**.
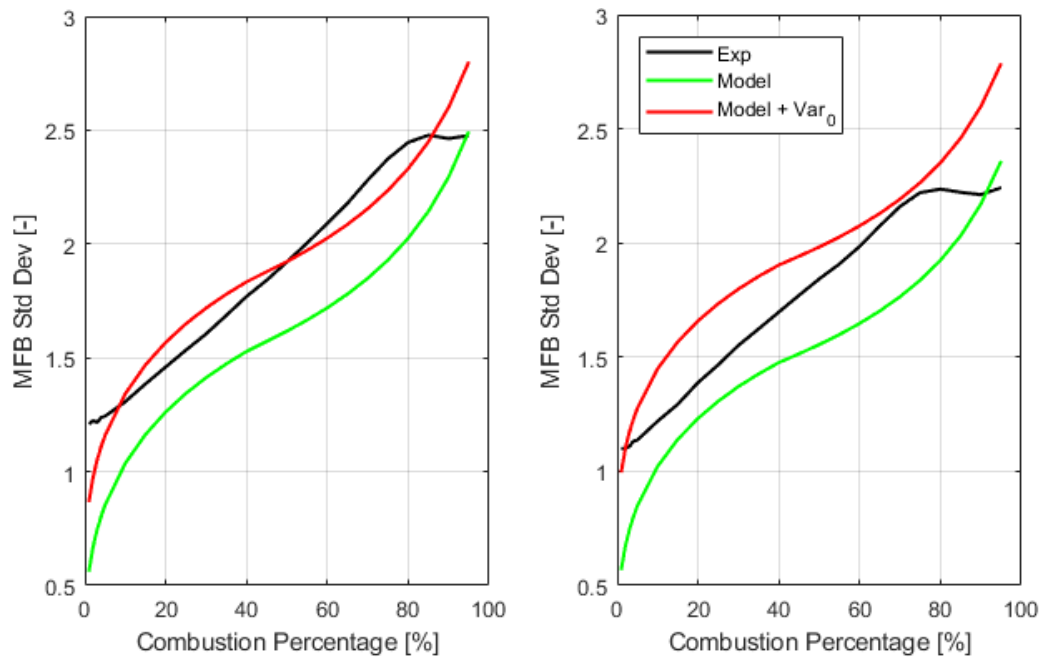

FIGURE 58: Experimental, model and initial variability model curves for sets 15 & 16.

Both the MFB and in-cylinder pressure dispersion results are shown in chapter 7.

7   Result Discussion

In this chapter **the models results will be discussed.** The results will be compare to the ones obtained from the experimental data. This comparison can be divided in **three different sections**. First the **duration of the combustion**. Then, the mean value combustion model results corresponding to the **MFB and the pressure profile**. Finally, the **combustion dispersion model results**.

7.1   SOC, EOC and TOC

Setting appropriated SOC and EOC points for the apparent burning law during the experimental data analysis **is required for a later proper model calibration**.

   The results presented are **the start** (Figure 59), **the end** (Figure 60) **and the total duration of the combustion** (Figure 61). The three parameters are represented for each constant inputs set (54 in total) of the characterization data.

   The crosses reflect the experimental values while the circles are represent the model ones. In blue are plotted the values corresponding to the low engine speed (1000 rpm), in light blue the medium engine speed (2000 rpm) and in yellow the high engine speed (3000 rpm). For each one, the first spark advance sweep was made at low engine load, the second at medium engine load and the third at high engine load. **The 9 spark advance sweeps are easily recognizable on each figure**. The inputs values can be check on Table 4.
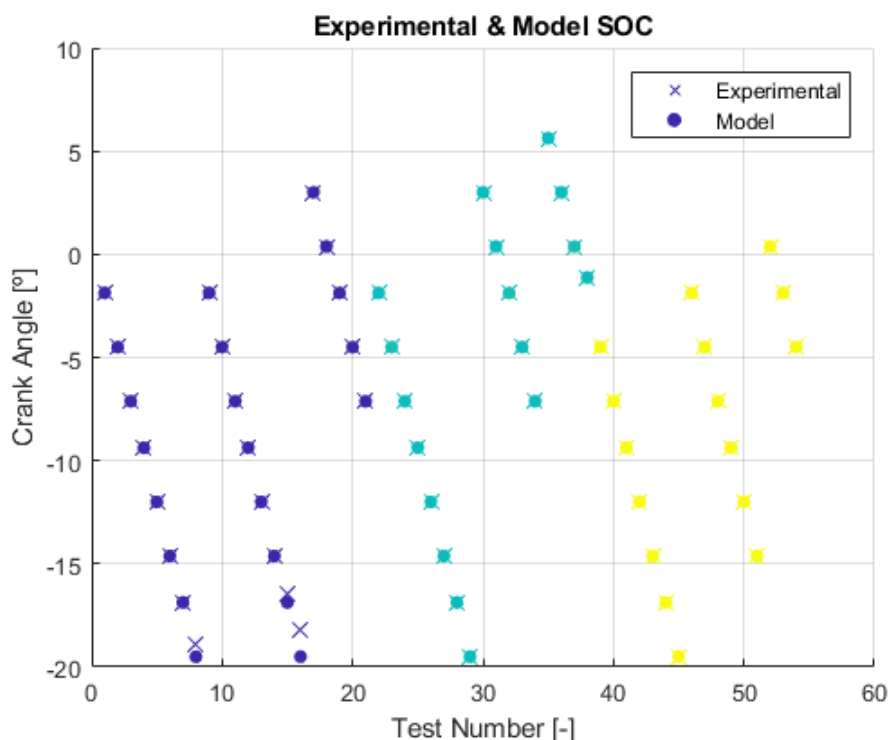

Figure 59: Experimental and modelled SOC.

   As it was explained in chapter 5, **the SOC model value has been taken as the value of the spark advance. The experimental SOC value is an estimation made from**

a least-squares adjustment between a Wiebe's function and the experimental heat released. In Figure 59, it can be seen the cases where exists a delay between the SOC and spark advance due to a high spark advance and not enough engine speed and load.
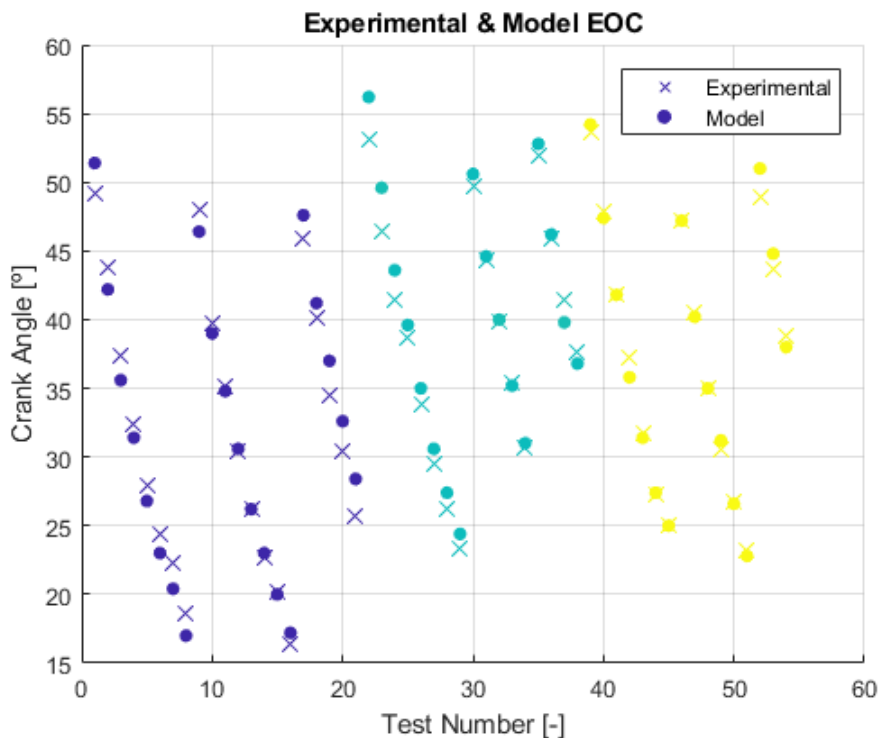

FIGURE 60: Experimental and modelled EOC.

In Figure 60 the experimental and model EOC values are shown. In both cases, it can be seen that **the increase of the EOC angle is higher as the SOC is found later**. This occurs because the **fast burning takes place away of the top dead center**, increasing combustion duration.

The experimental and model **results are accurate for all sets**, finding the biggest differences at low and medium engine speed and low and high engine load. However, these **differences are not greater than 3 crank degrees**.

Finally, the total duration of the combustion is represented in Figure 61. It has been calculated as the difference between the EOC and SOC. It can be seen that the **combustion duration is smaller for the SOC values which lead the fast burning stage closer the top dead center**.

As a common tendency, the **differences between the model and experimental TOC are practically the ones mentioned for the EOC values**. These do **not overcome again the absolute error of 3 crank degrees** in the worst scenarios. The greatest relative errors are found for the smallest SOC values where the combustion is longer. However, these **relative errors are less than 10%**.
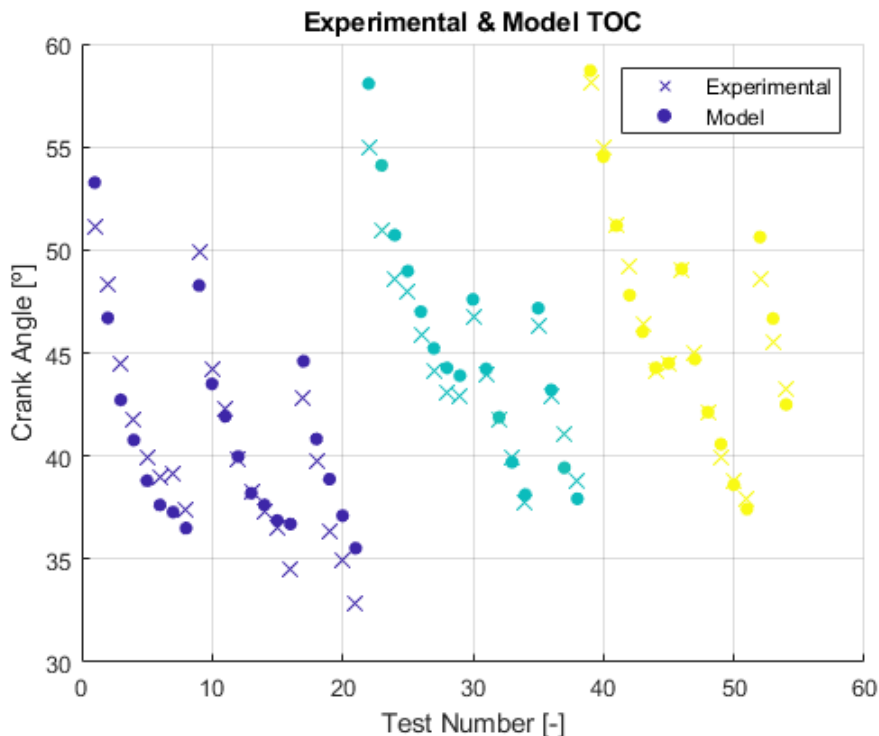
FIGURE 61: Experimental and modelled TOC.

7.2   Mass Fraction Burned and In-Cylinder Pressure Evolution

It could be the case that both the model SOC and EOC were exactly the same as the experimental ones. However, if the model had a very fast burning rate at the beginning of the combustion and then a very slow one at the end compared to the one measured at the experimental facilities (or vice versa), the MFB at each crank angle will not match at all.

The combustion burning rate mainly depends on the constants (C_1, C_2 & C_3) and its calibration. Besides, the combustion correction factor also influences the amount of heat released in the combustion and the peaks of pressure reached at the combustion chamber.

In this section the mean combustion model results are presented. These correspond to the **MFB and the in-cylinder pressure evolution**. They have been divided into **nine different figures**, in which each one collects the results of the sets corresponding to **the nine spark advance sweeps**.

At the **upper part** of each figure are the **plots corresponding to the mass fraction burned**. At the **lower part the in-cylinder pressure evolution plots of the same set** are found. On each plot it can be seen the **experimental values in black and the model values in red**.

Figures 62, 63 and 64 show the **spark advance sweeps made at low engine speed** (1000 rpm) at low, medium and high load level correspondingly.
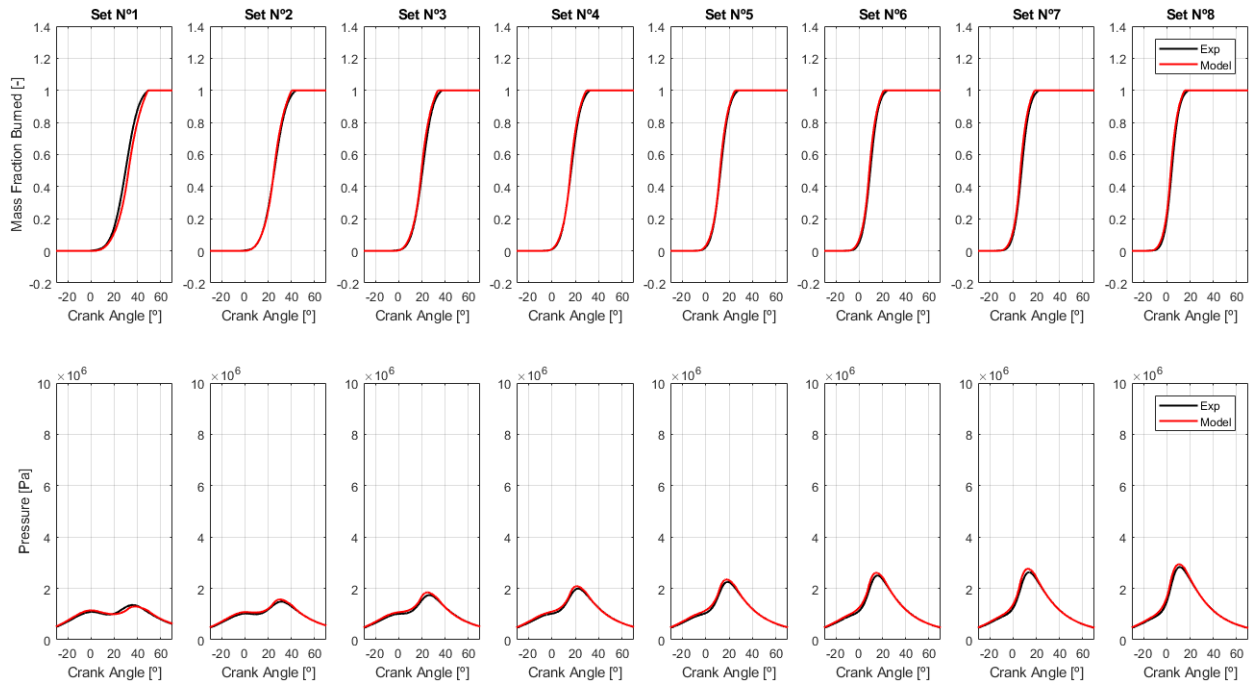
FIGURE 62: MFB and in-cylinder pressure for low engine speed and low load level.

The **cumulative relative errors** of the MFB curves are in a range **between 5% and 12%**, except for the first set (which has the smallest spark advance) where this error reach the 20%.
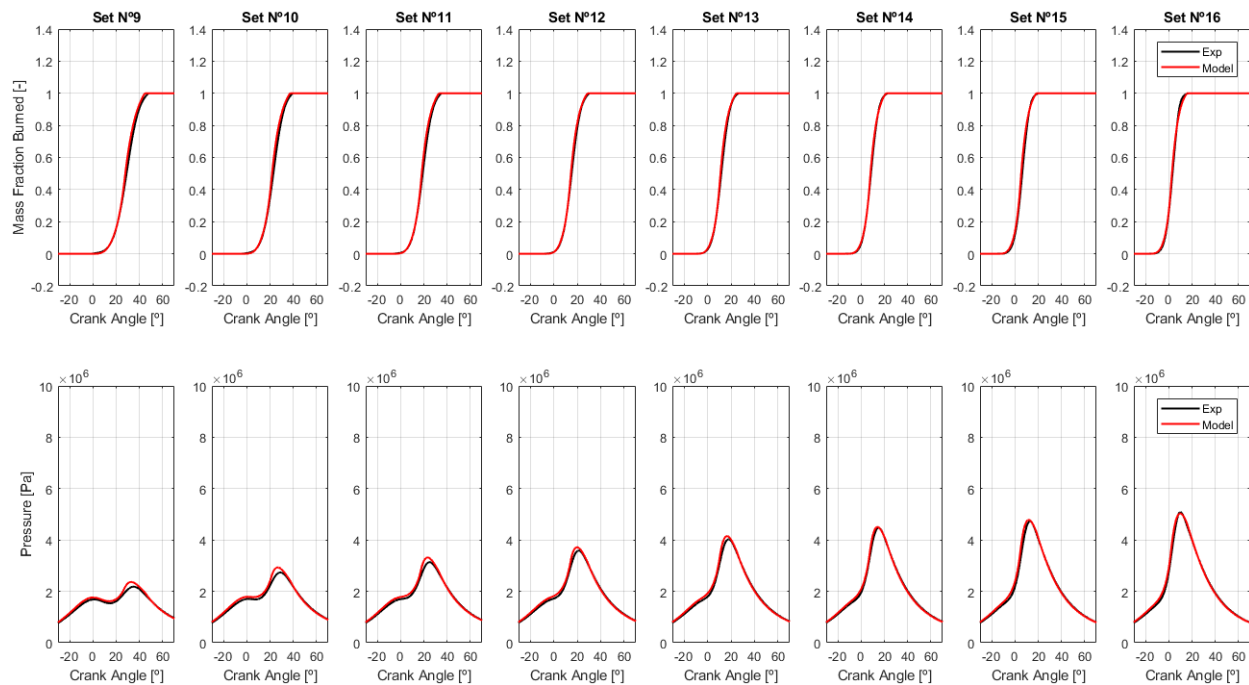

FIGURE 63: MFB and in-cylinder pressure for low engine speed and medium load level.

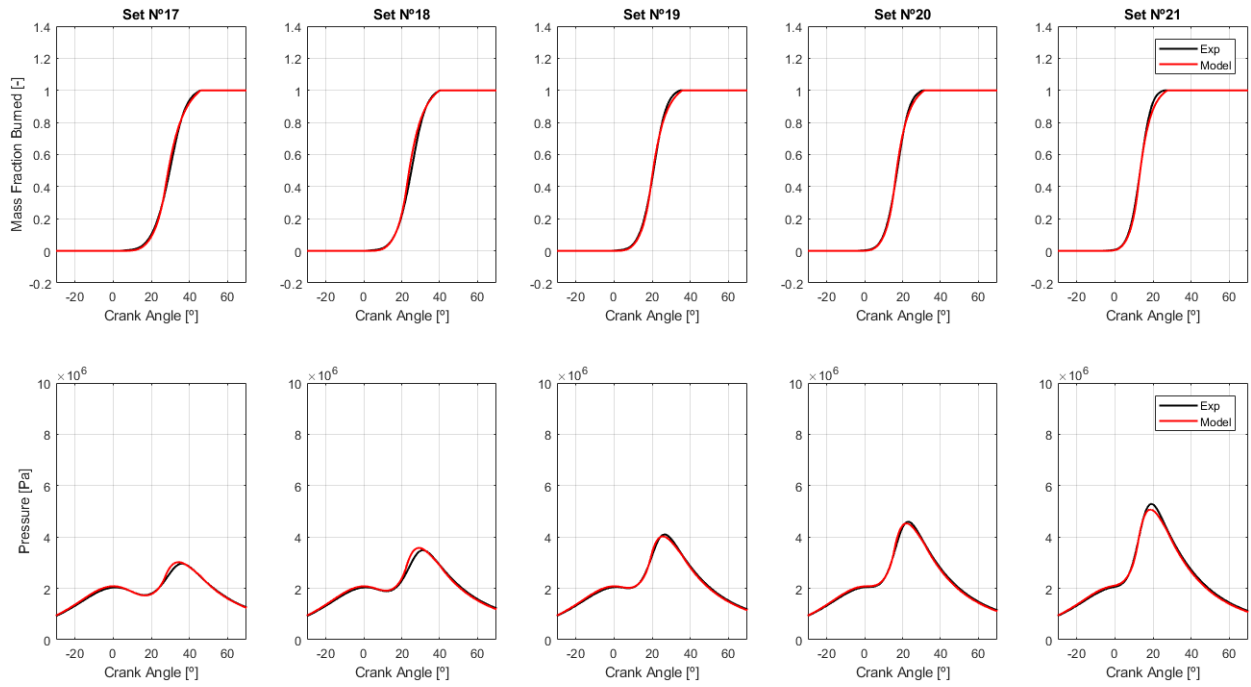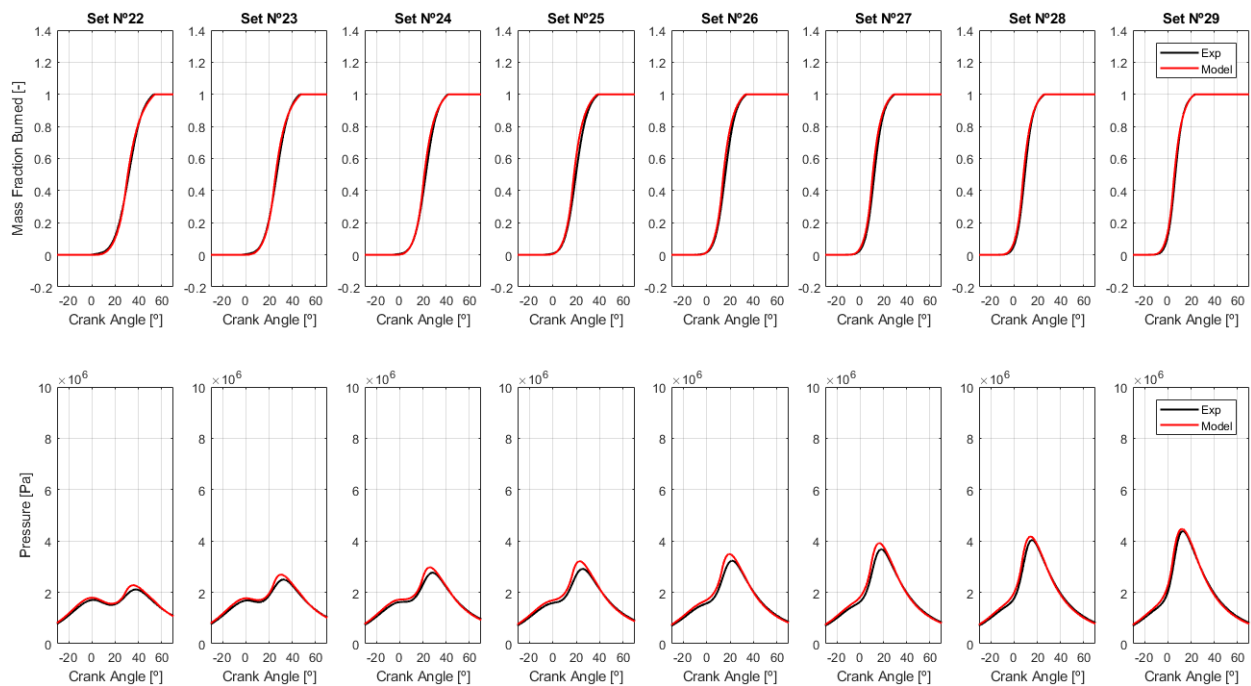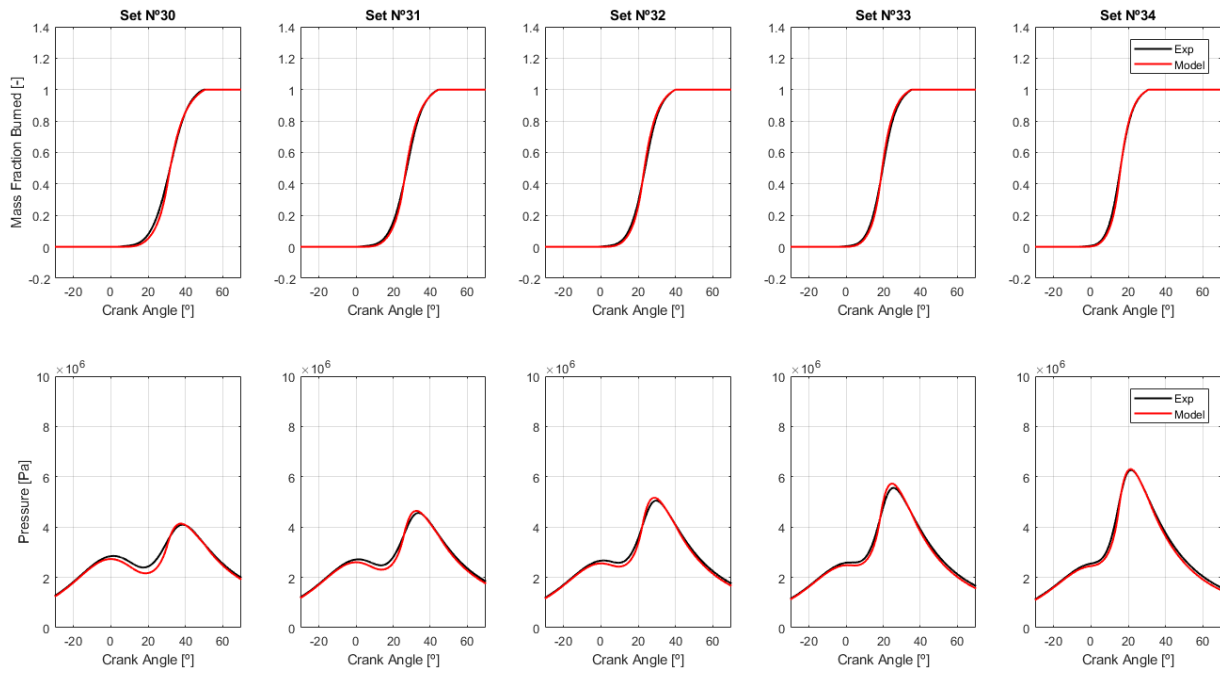The **cumulative relative errors** of the MFB curves are in a range **between 4% and 11%**.

FIGURE 64: MFB and in-cylinder pressure for low engine speed and high load level.

The **cumulative relative errors** of the MFB curves are in a range **between 5% and 8%**.

Figures 65, 66 and 67 show the **spark advance sweeps made at medium engine speed** (2000 rpm) at low, medium and high load level correspondingly.

FIGURE 65: MFB and in-cylinder pressure for medium engine speed and low load level.

The **cumulative relative errors** of the MFB curves are in a range **between 6% and 14%**.

FIGURE 66: MFB and in-cylinder pressure for medium engine speed and medium load level.

The **cumulative relative errors** of the MFB curves are in a range **between 5% and 9%**.
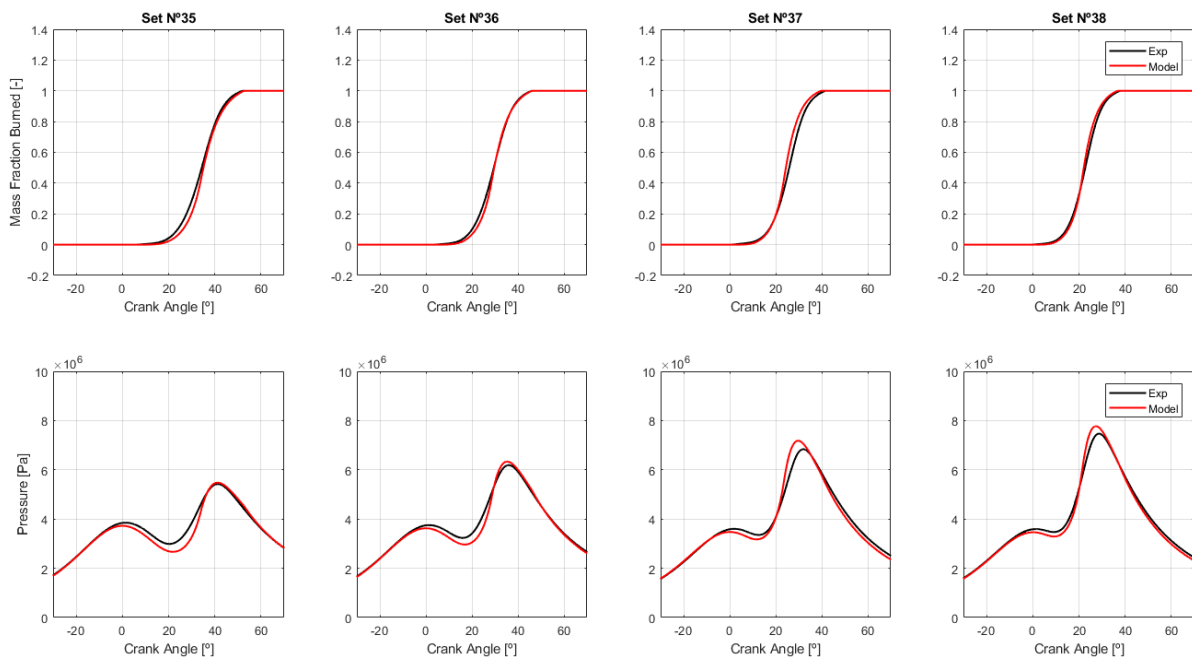

FIGURE 67: MFB and in-cylinder pressure for medium engine speed and high load level.

The **cumulative relative errors** of the MFB curves are in a range **between 8% and 15%**.

Figures 68, 69 and 70 show the spark advance sweeps made at high engine speed (3000 rpm) at low, medium and high load level correspondingly.
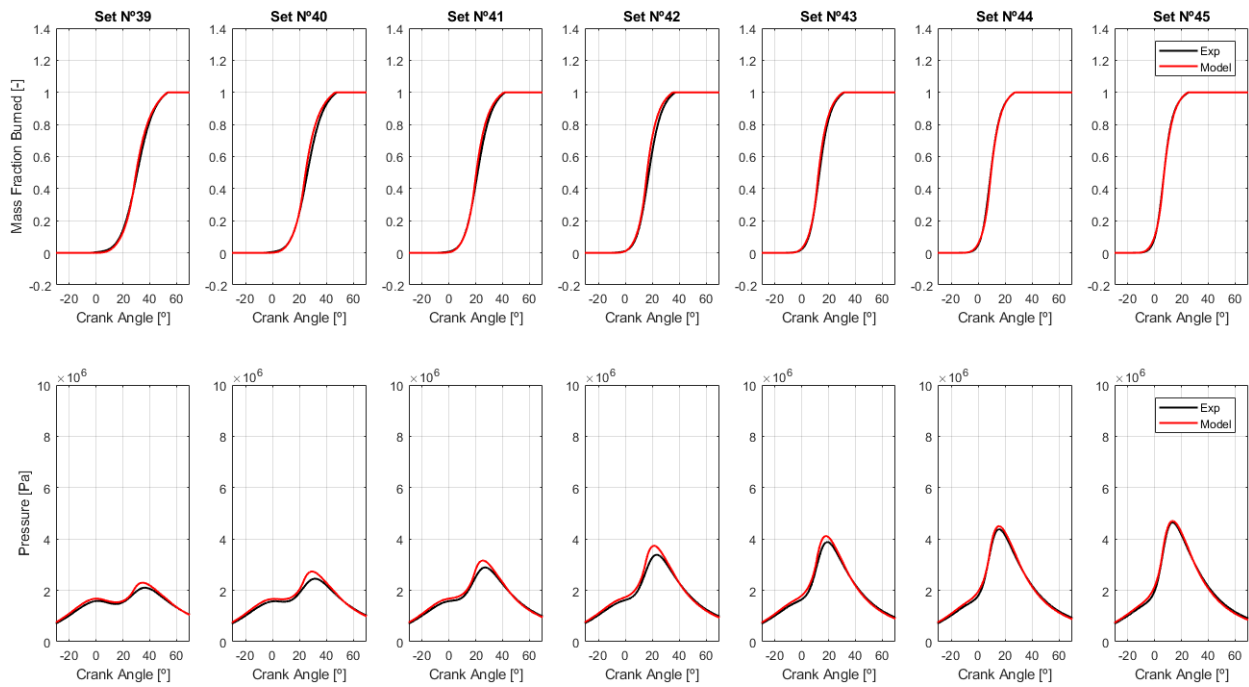

FIGURE 68: MFB and in-cylinder pressure for high engine speed and low load level.

The **cumulative relative errors** of the MFB curves are in a range **between 2% and 13%**.
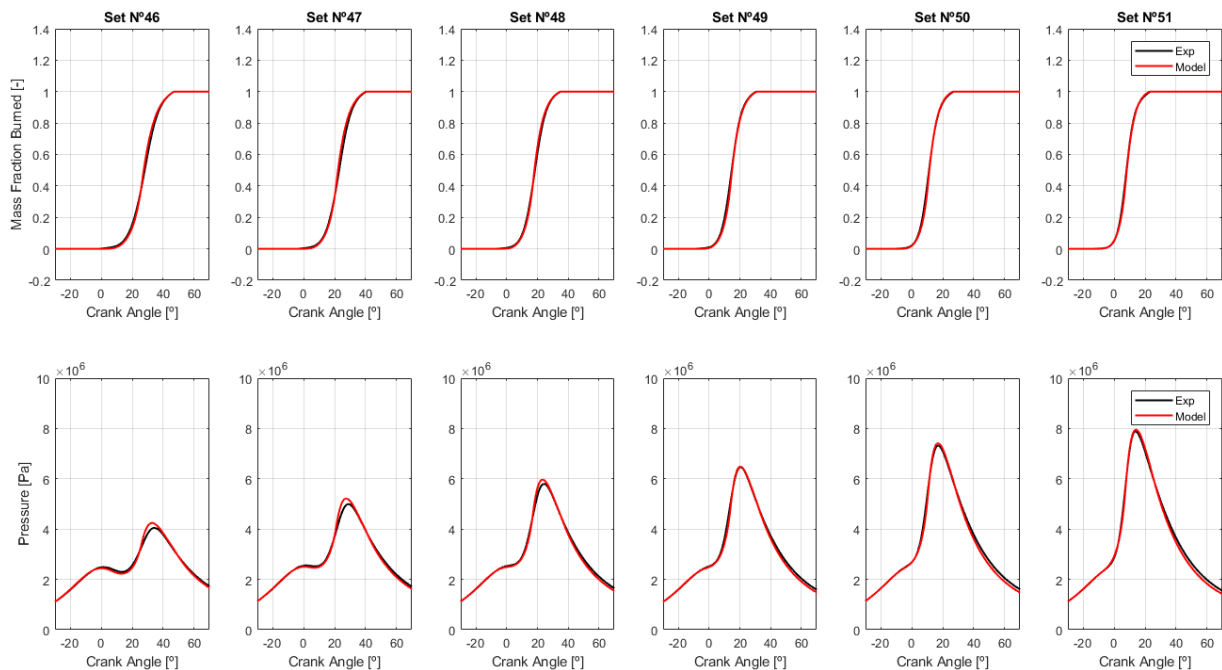

FIGURE 69: MFB and in-cylinder pressure for high engine speed and medium load level.

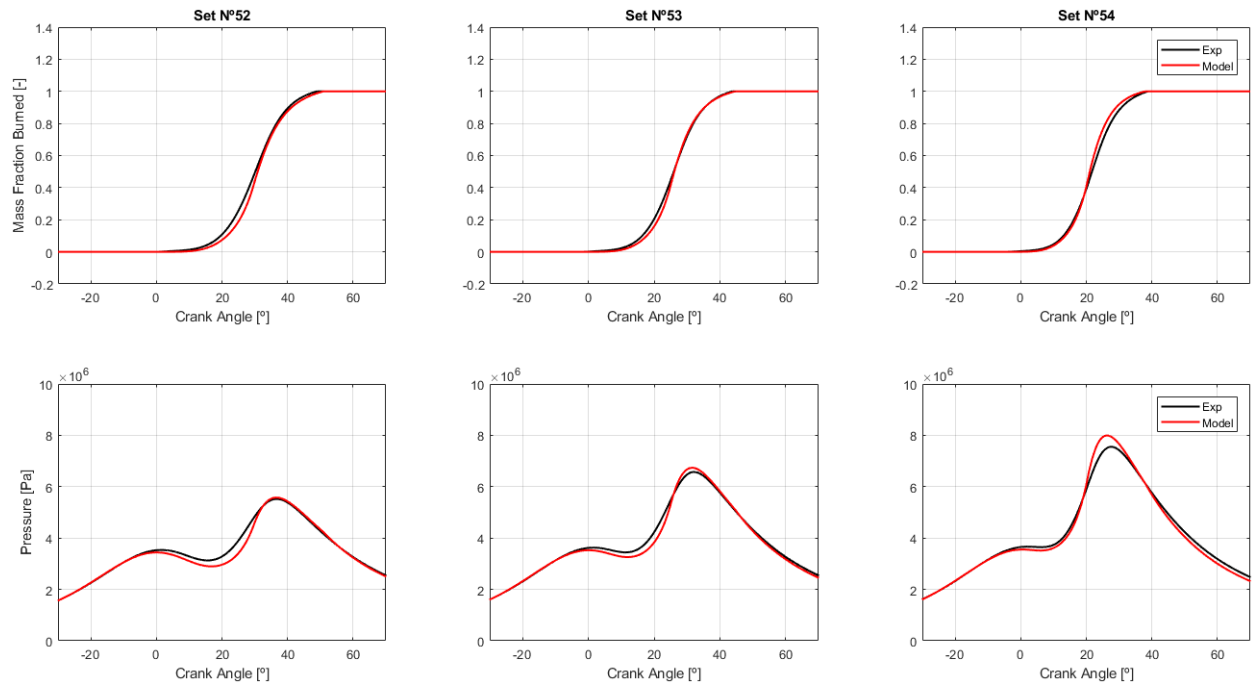The **cumulative relative errors** of the MFB curves are in a range **between 3% and 8%**.

FIGURE 70: MFB and in-cylinder pressure for high engine speed and high load level.

The **cumulative relative errors** of the MFB curves are in a range **between 7% and 12%**.

Except in one case (set 1), the **cumulative relative error between the model and experimental curves is kept lower than 15%**. Moreover, it exists a comment tendency of **higher error values as the spark advance decreases and the engine load and speed increase**.

For the **exceptional case where the error is slightly higher** (set 1), it can be explained by two main factors. In Figure 45, it can be seen that this set has one of the **biggest difference between the adjusted and modelled C_2 constant**. Besides, the **modelled correction factor (Figure 38) has also an error compared to experimental value**. All together lead the MFB curve to an error greater than in the other cases.

However, it is especially **difficult to extract tendencies** about the comparison between both the experimental and model mass fraction burned and in-cylinder pressure evolution. **This is because the effects of the different factors** (constants calibration, the SOC and EOC location and the selected combustion correction factor) **interfere with each other**. It could happens that either these individual errors **give rise to a higher error on the MFB curve** (as in set 1) **or they compensate each other** producing a lower error.

In order to test out the model outside the operating points with which it has been adjusted and calibrated, the **results from the validation data** (Table 5) are also analysed. The mass fraction burned and the in-cylinder pressure evolution curves are shown below in Figures 71, 72 and 73.
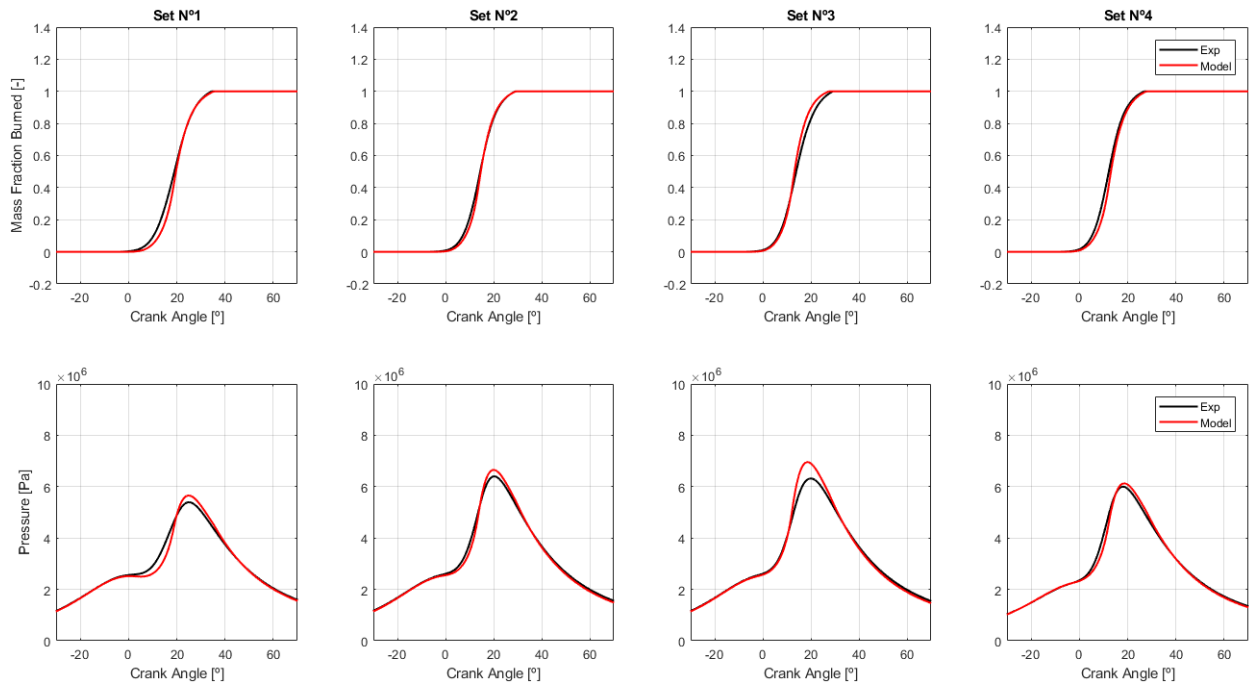
FIGURE 71: MFB and in-cylinder pressure for medium engine speed from validation data.

The **cumulative relative errors** of the MFB curves are in a range **between 7% and 14%**.
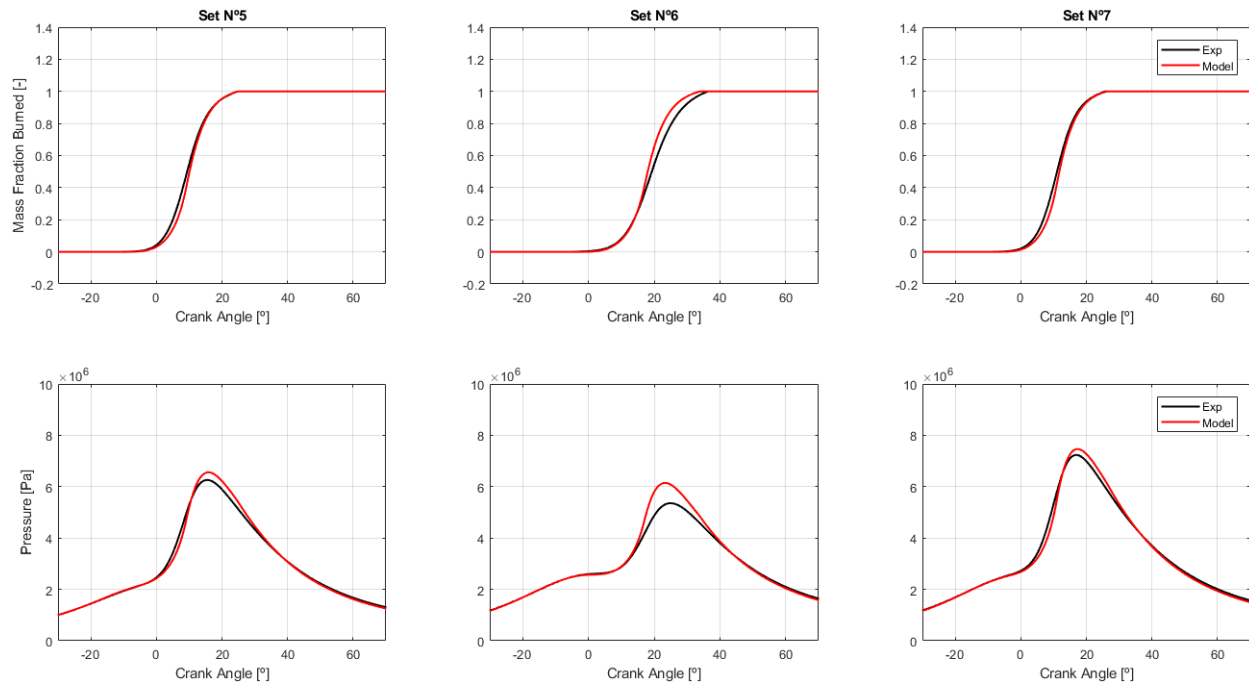

FIGURE 72: MFB and in-cylinder pressure for medium-high engine speed from validation data.

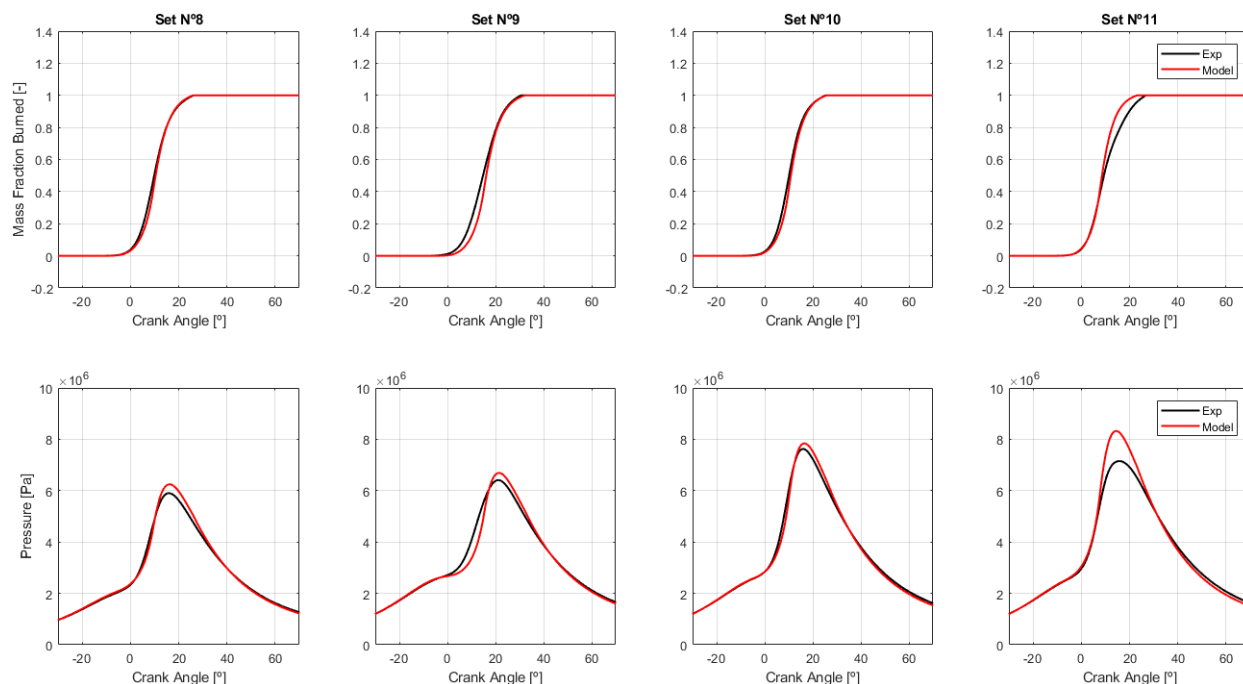The **cumulative relative errors** of the MFB curves are in a range **between 9% and 16%**.

FIGURE 73: MFB and in-cylinder pressure for high engine speed from validation data.

The **cumulative relative errors** of the MFB curves are in a range **between 7% and 19%**.

Again, the tendency of **higher relative error at smaller spark advance and higher engine load and speed** is found. The cumulative relative **errors** from the validation data are **slightly bigger than the ones obtained from the characterization data. However, these are still reasonable** for this mean value combustion model.

7.3   Combustion Dispersion Model Results

In this section the **dispersion model results will be analysed and compared to the experimental ones**. First, for the characterization data (Table 4) and then, for the validation data (Table 5).

The variability **results complements the previous mean combustion model results**. However, the stochastic nature of the dispersion phenomenon introduces a high level of difficulty for the study and modelling, as it has been shown in chapter 6.

The **results have been divided in two parts**. On the one hand, the comparison between both the **experimental and model mass fraction burned variability curves** with its relative errors along the combustion. On the other hand, both the **experimental and model mass fraction burned and in-cylinder pressure curves** with its respective dispersion.

First, the results from the characterization data will be shown and analysed. In Figures 74 to 82, the results for the nine spark advances sweeps at different engine speed and load level are shown. **Top plots correspond to the MFB variability** (standard deviation

along combustion) while **bottom plots show the relative error at each combustion percentage**.
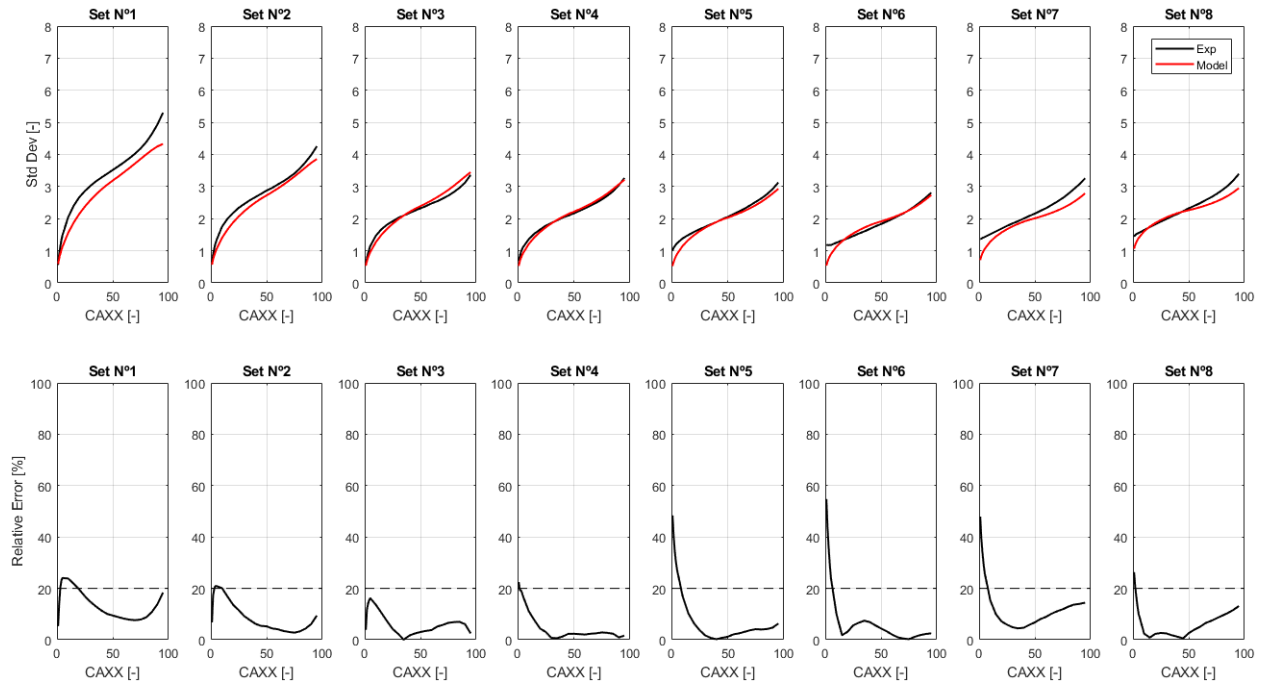

FIGURE 74: Experimental and model variability and its relative error for low engine speed and low engine load level.
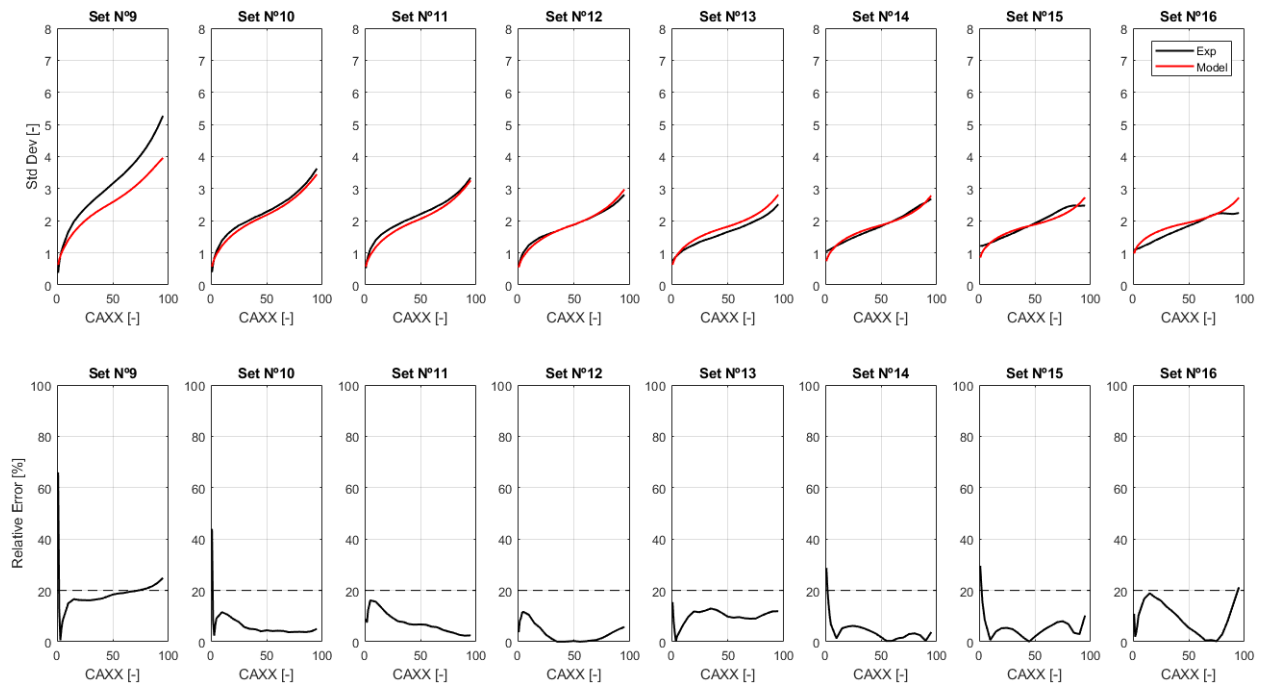

FIGURE 75: Experimental and model variability and its relative error for low engine speed and medium engine load level.
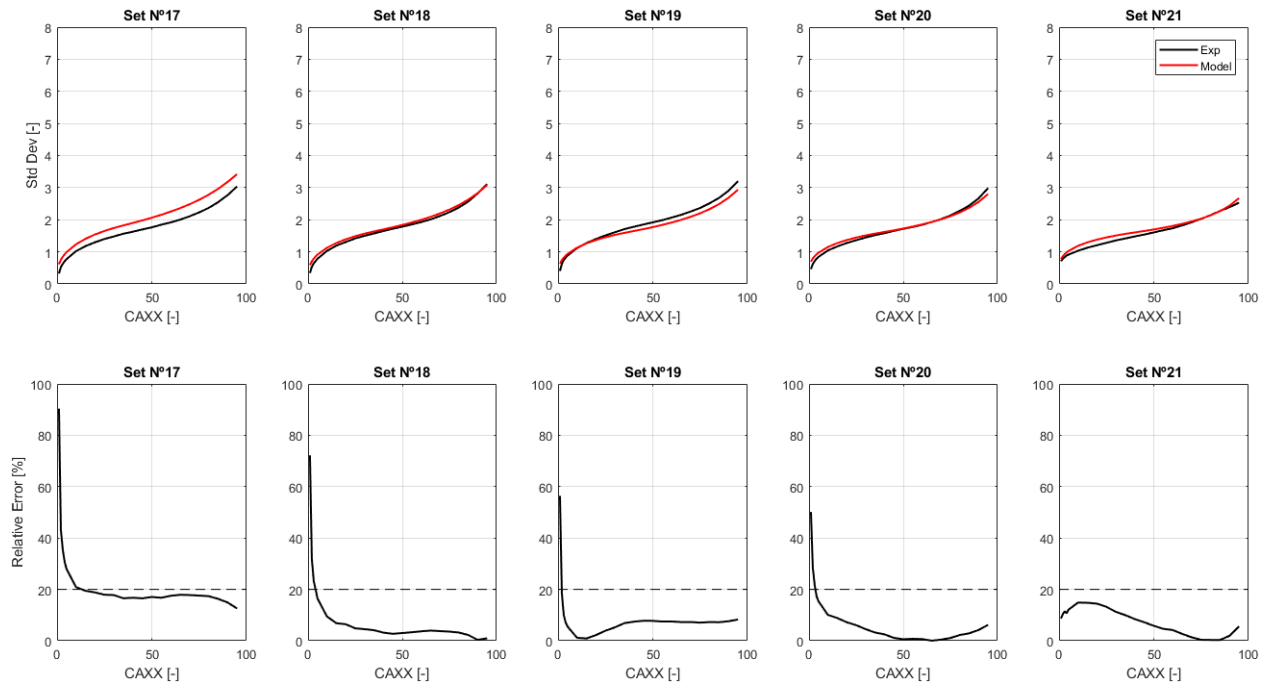
FIGURE 76: Experimental and model variability and its relative error for low engine speed and high engine load level.
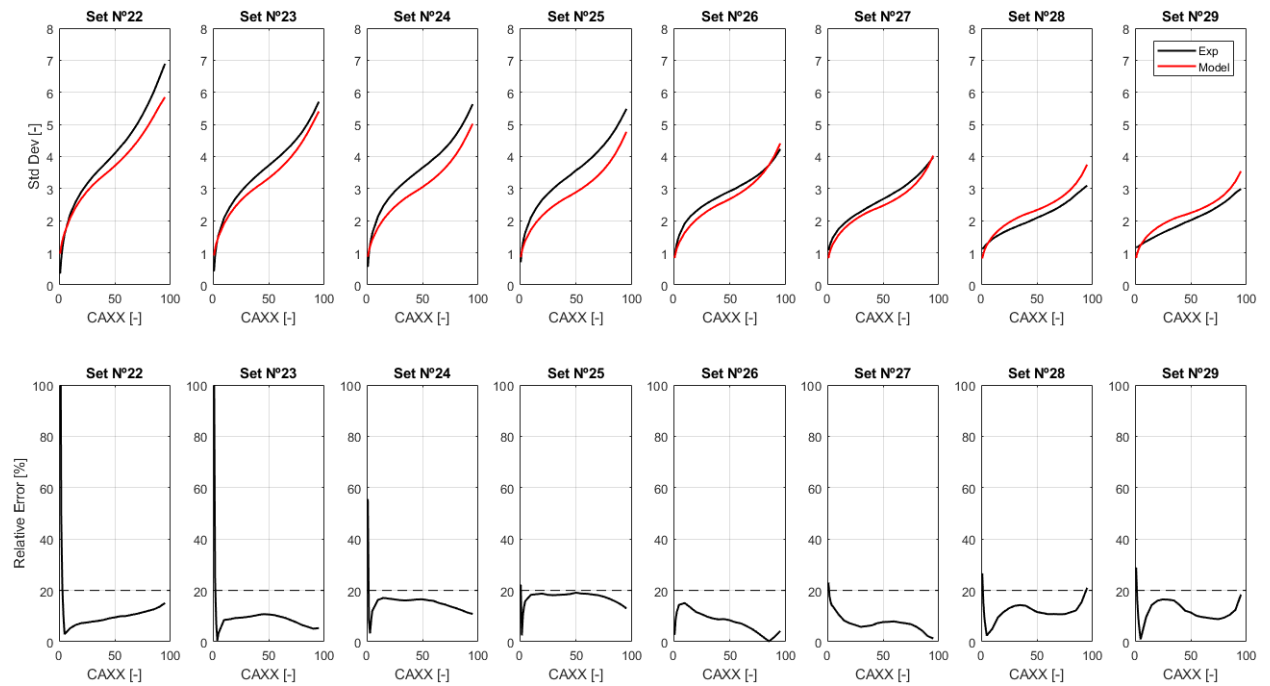

FIGURE 77: Experimental and model variability and its relative error for medium engine speed and low engine load level.
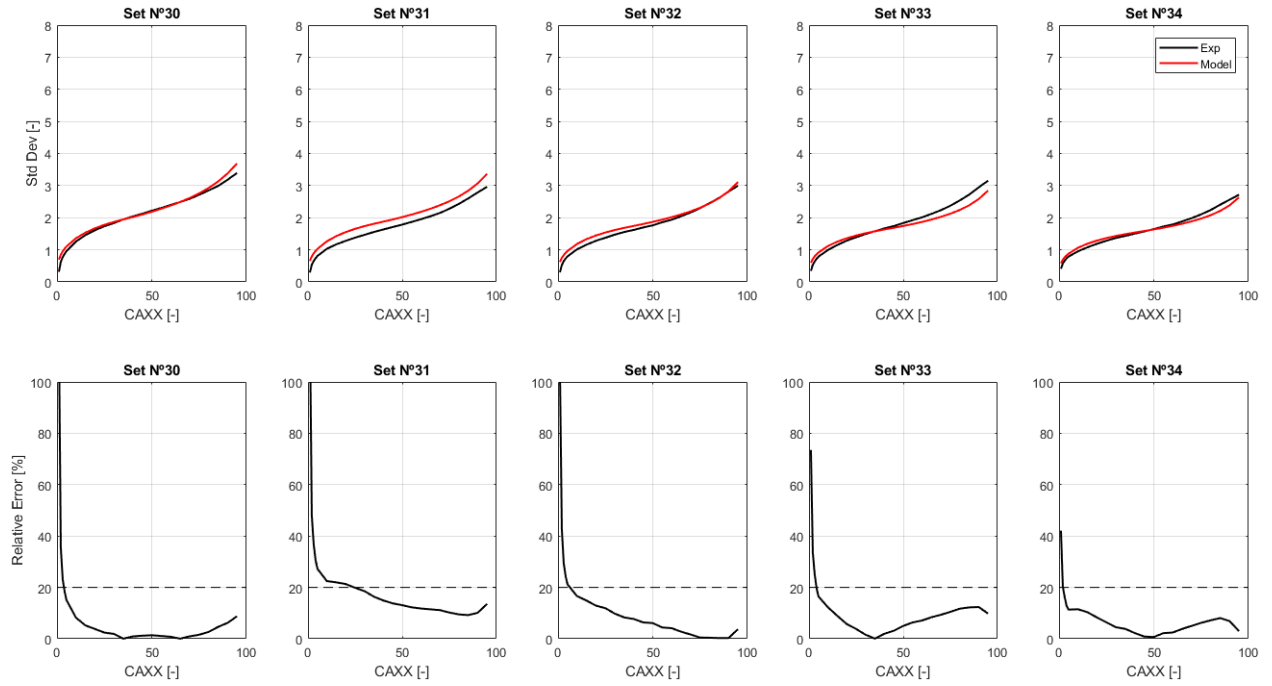
FIGURE 78: Experimental and model variability and its relative error for medium engine speed and medium engine load level.
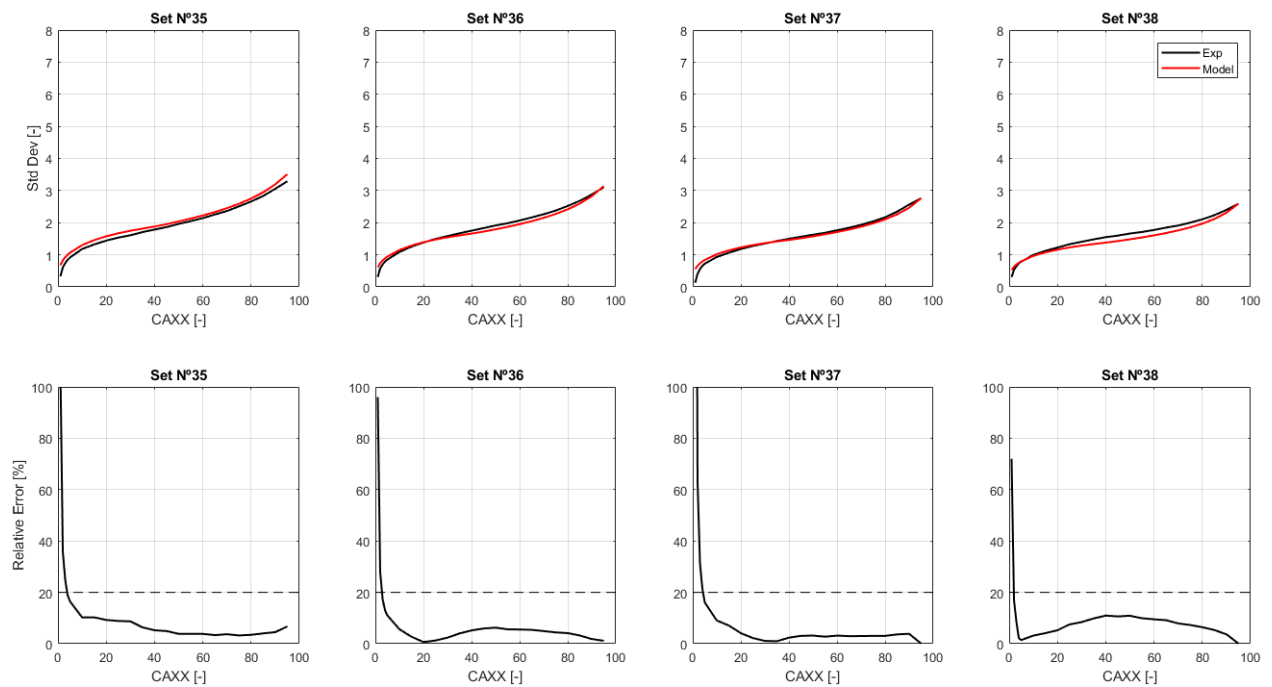

FIGURE 79: Experimental and model variability and its relative error for medium engine speed and high engine load level.
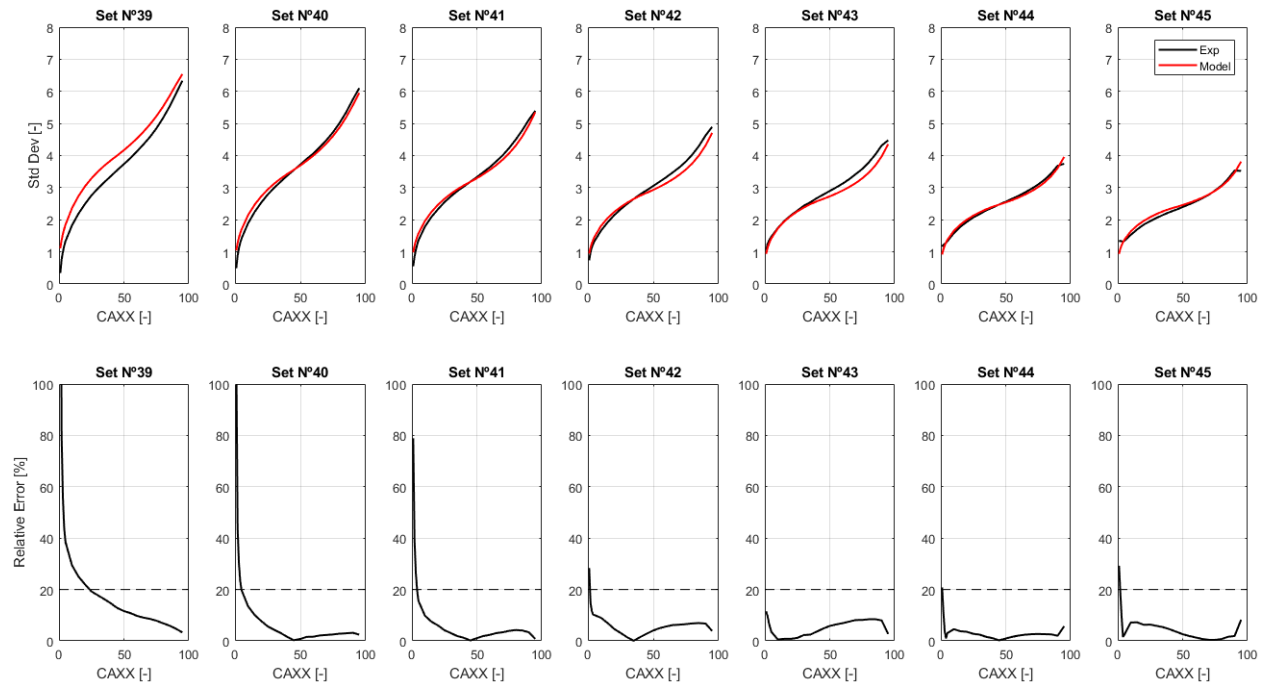
FIGURE 80: Experimental and model variability and its relative error for high engine speed and low engine load level.
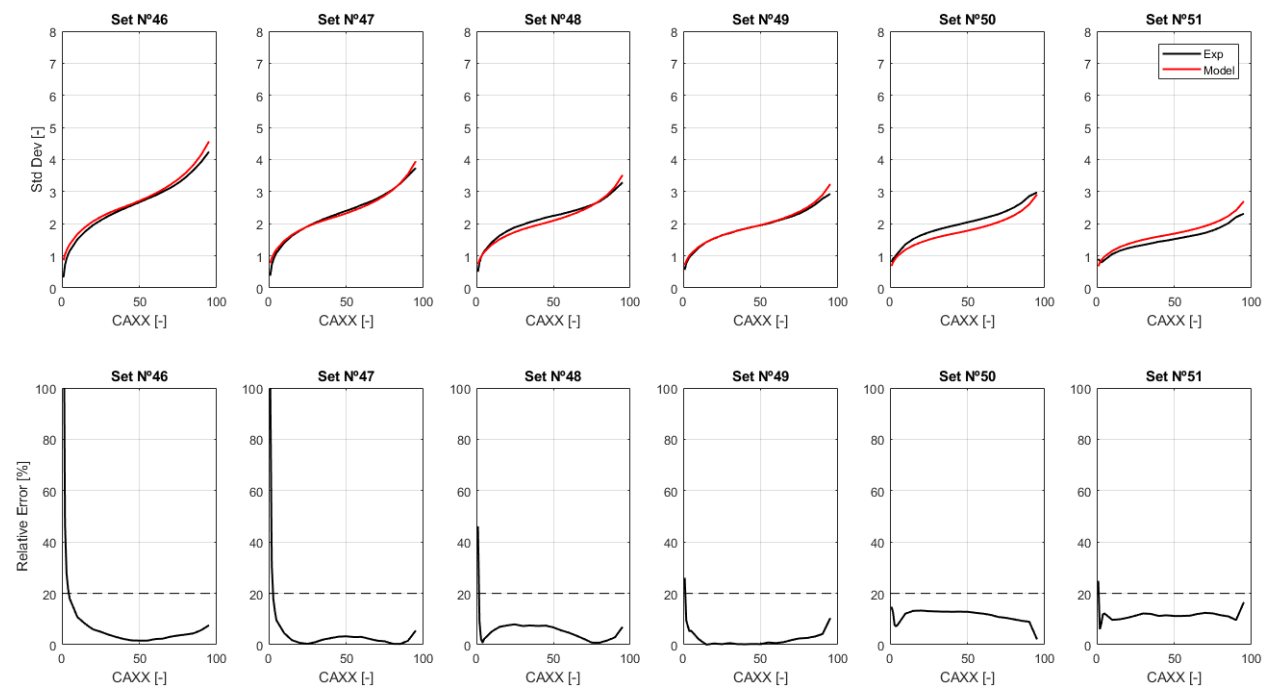

FIGURE 81: Experimental and model variability and its relative error for high engine speed and medium engine load level.
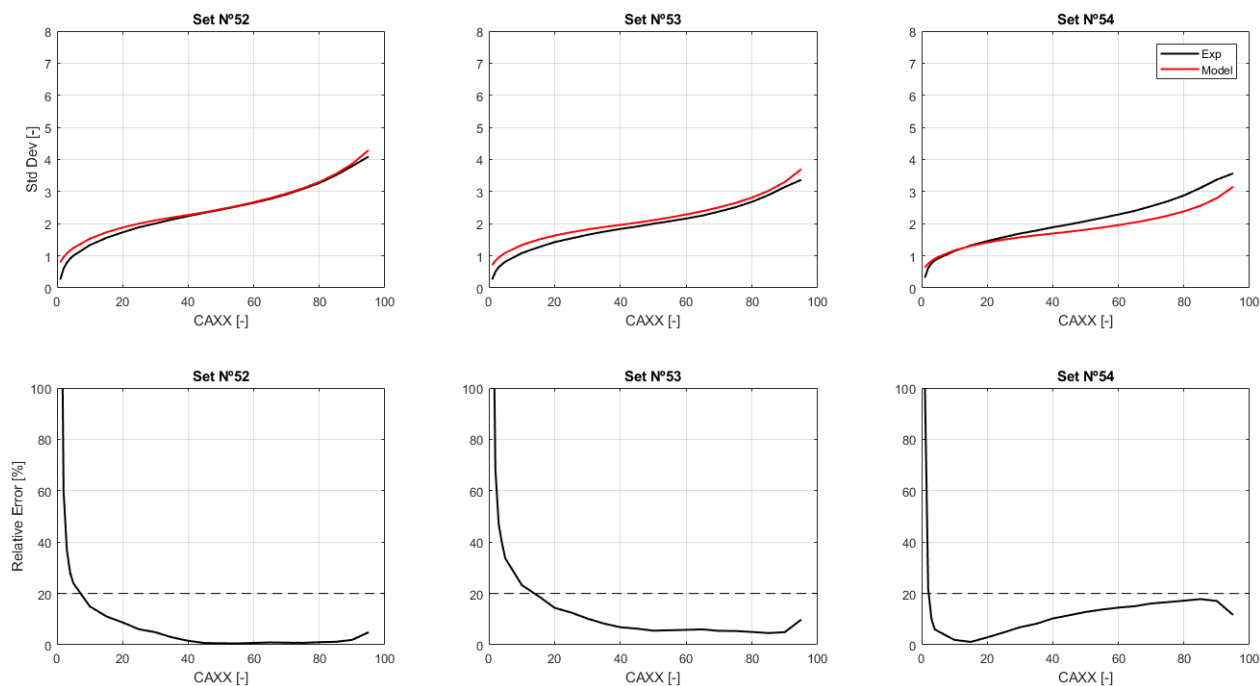
FIGURE 82: Experimental and model variability and its relative error for high engine speed and high engine load level.

From a **qualitative perspective** of the experimental and modelled variability curves (top plots), the **results are close**. There are some exceptions in cases 1, 9, or 25, where higher differences can be appreciated. However, **quantitative errors have been extracted** (bottom plots) in order to quantify these differences and be able to asses the comparison.

Due to the **low values of the experimental MFB variability at the beginning of the combustion, the relative error values go very high until 10/15% of the combustion**. Nevertheless, the absolute errors are not that high. Therefore, this first combustion stage is not taken into account for the results analysis.

From this combustion percentage, it can be seen that the **relative error** from the C_1 and C_2 standard deviation modelling **is reasonable** considering its difficulty. **These relative errors do not exceed the 20% and even in some cases 10%**.

The **maximums of the cumulative relative error** between the 10% and the totality of the combustion **have been found at 6-7%** in sets 1, 9 and 25. These are again more than acceptable results.

Similar results were found after analyzing the validation data results. These can be seen in Figures 83, 84 and 85. The relative errors are below 20% for each combustion percentage between 15% and 100%. The **maximums cumulative relative error have also be found between 6-7%**.
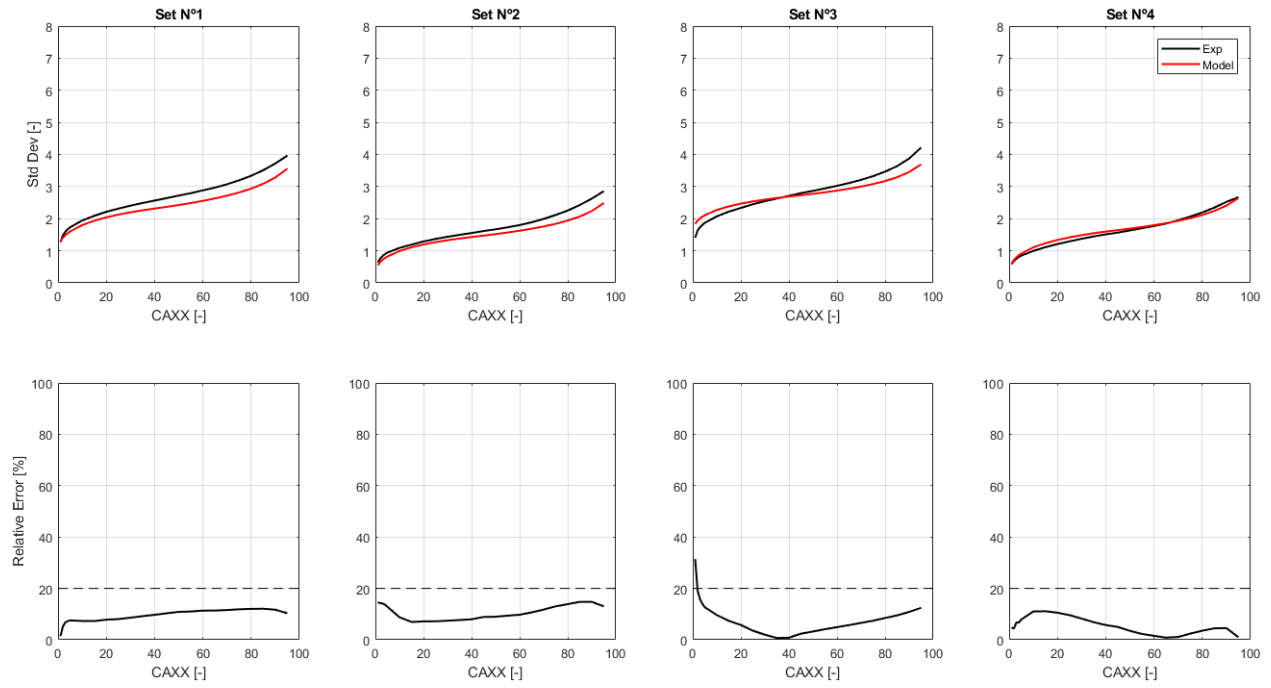
FIGURE 83: Experimental and model variability and its relative error for medium engine speed from validation data.
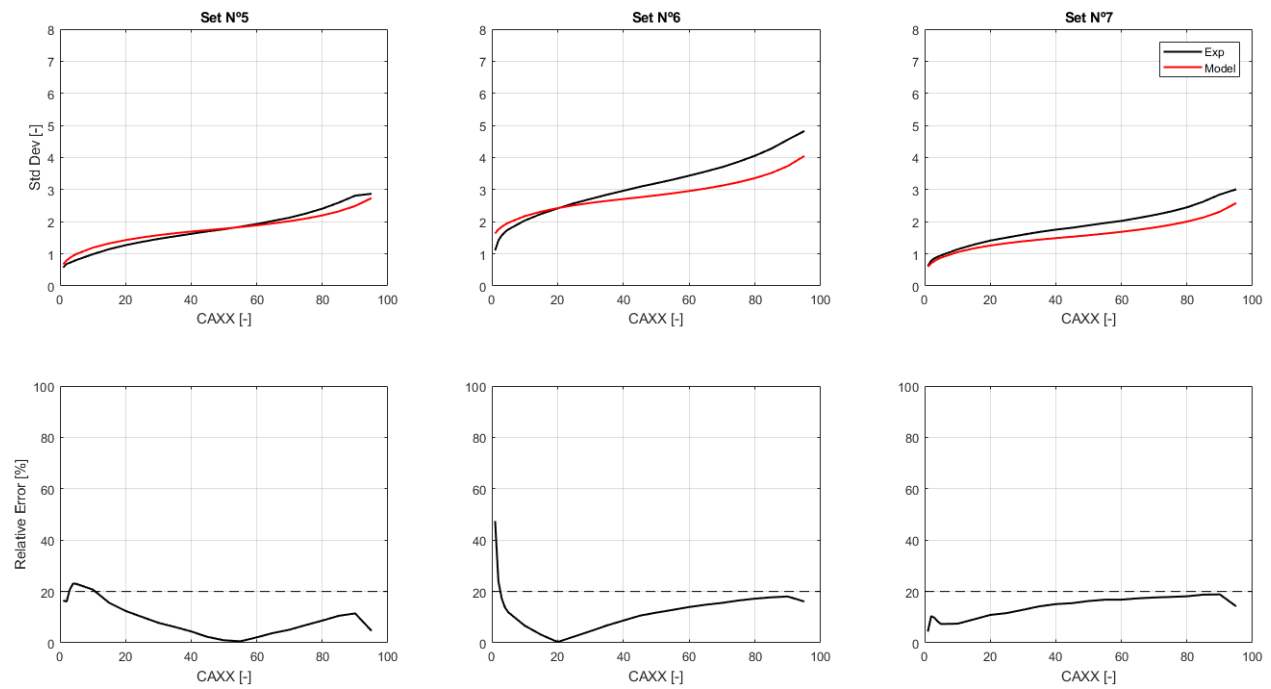
FIGURE 84: Experimental and model variability and its relative error for medium-high engine speed from validation data.
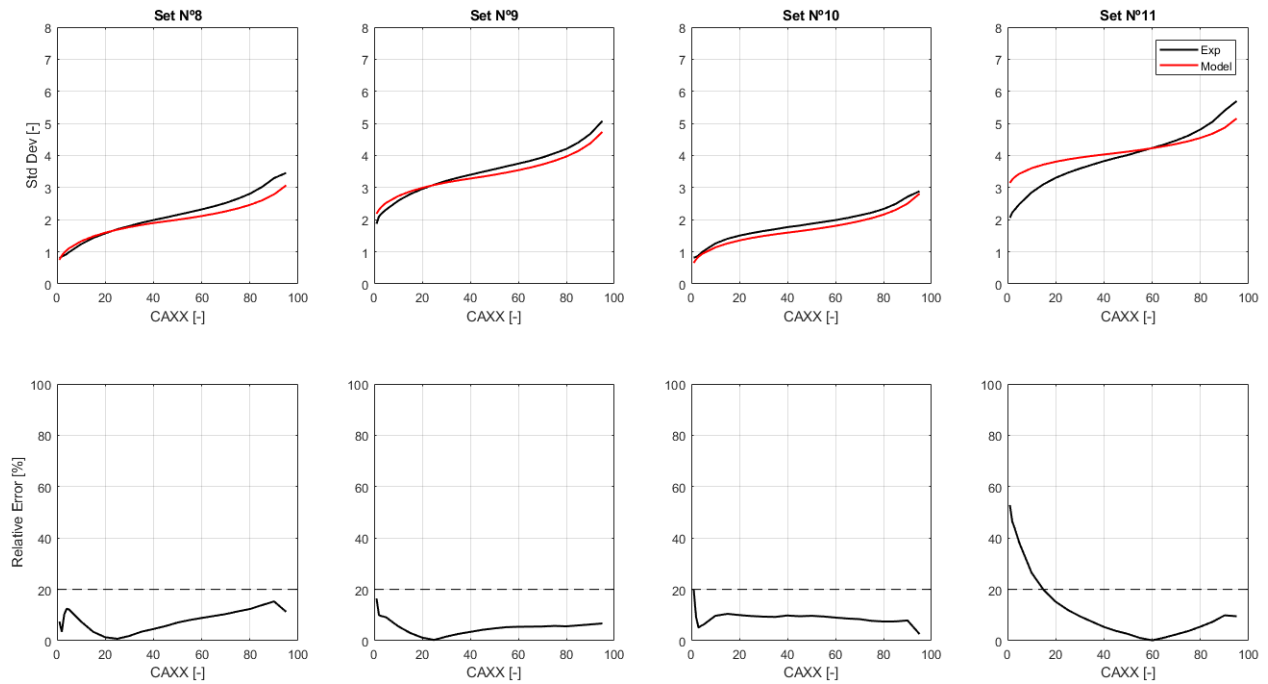
FIGURE 85: Experimental and model variability and its relative error for high engine speed from validation data.

According to these variability results, it has been proceeded to calculate the **mass fraction burned and the in-cylinder pressure evolution along the combustion with its respective dispersion associated**. In Figures 86 to 94, it can be seen the combined effect of the errors introduced by both models (mean combustion value and dispersion).

FIGURE 86: MFB and in-cylinder pressure with its respective dispersion for low engine speed and low load level.

FIGURE 87: MFB and in-cylinder pressure with its respective dispersion for low engine speed and medium load level.

FIGURE 88: MFB and in-cylinder pressure with its respective dispersion for low engine speed and high load level.
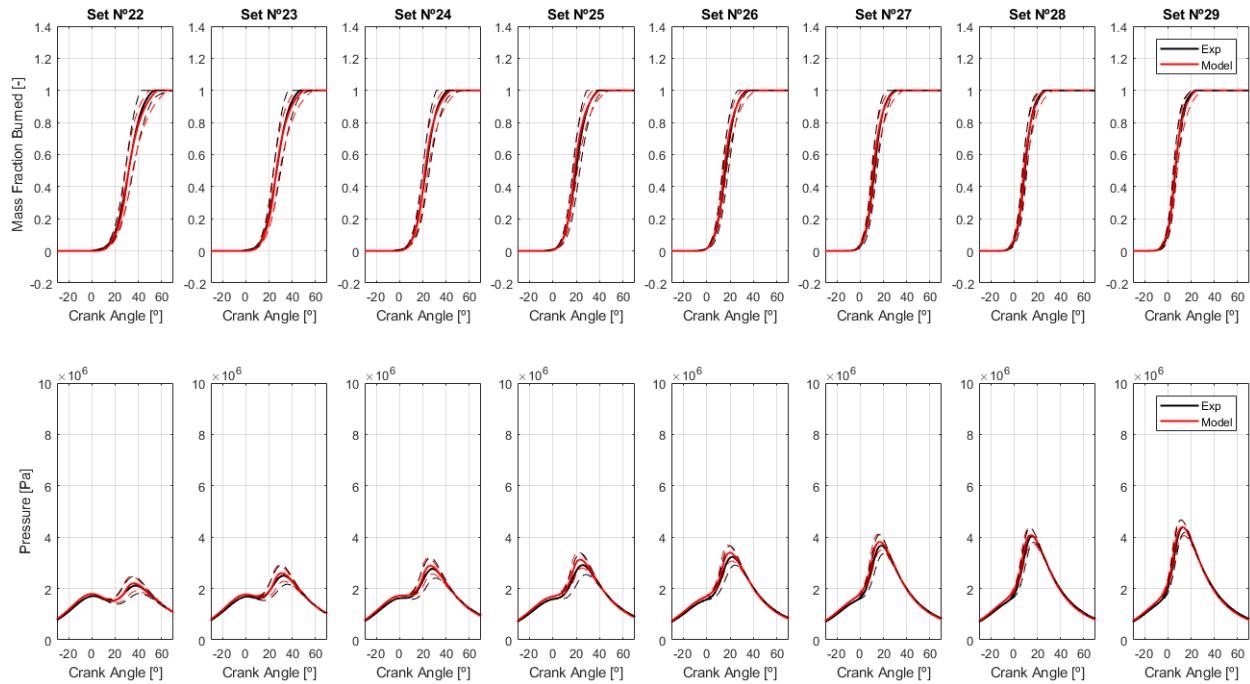
FIGURE 89: MFB and in-cylinder pressure with its respective dispersion for medium engine speed and low load level.

FIGURE 90: MFB and in-cylinder pressure with its respective dispersion for medium engine speed and medium load level.

FIGURE 91: MFB and in-cylinder pressure with its respective dispersion for medium engine speed and high load level.
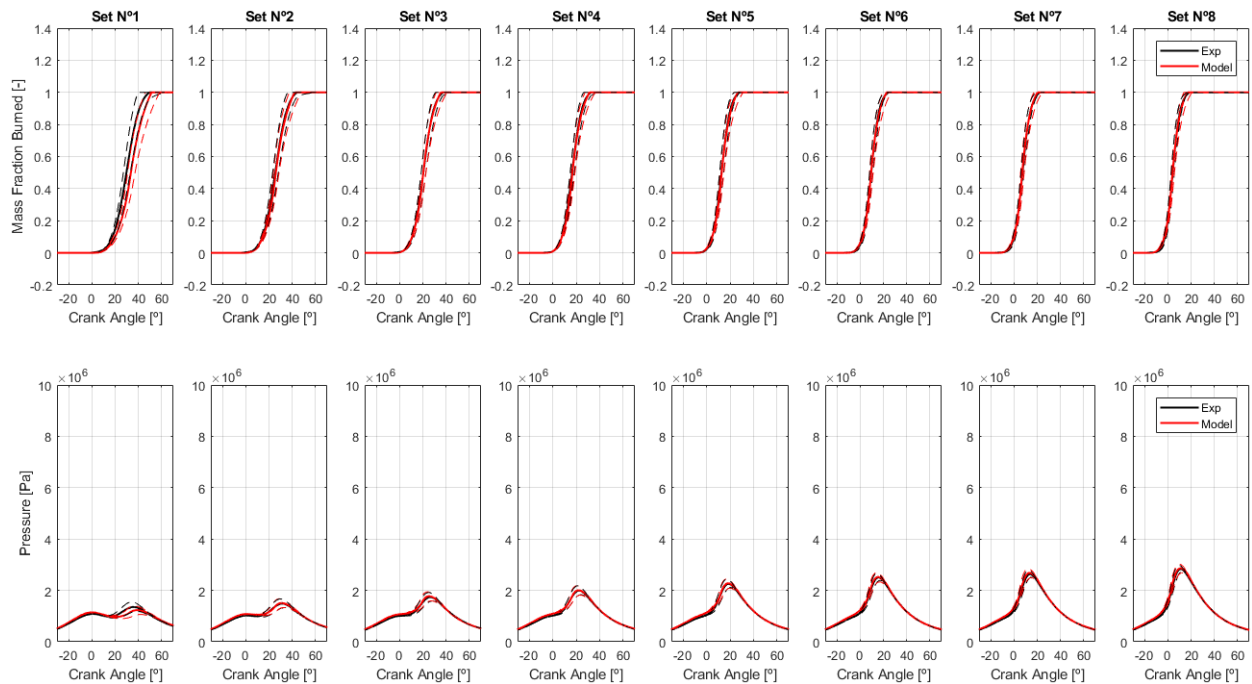

FIGURE 92: MFB and in-cylinder pressure with its respective dispersion for high engine speed and low load level.
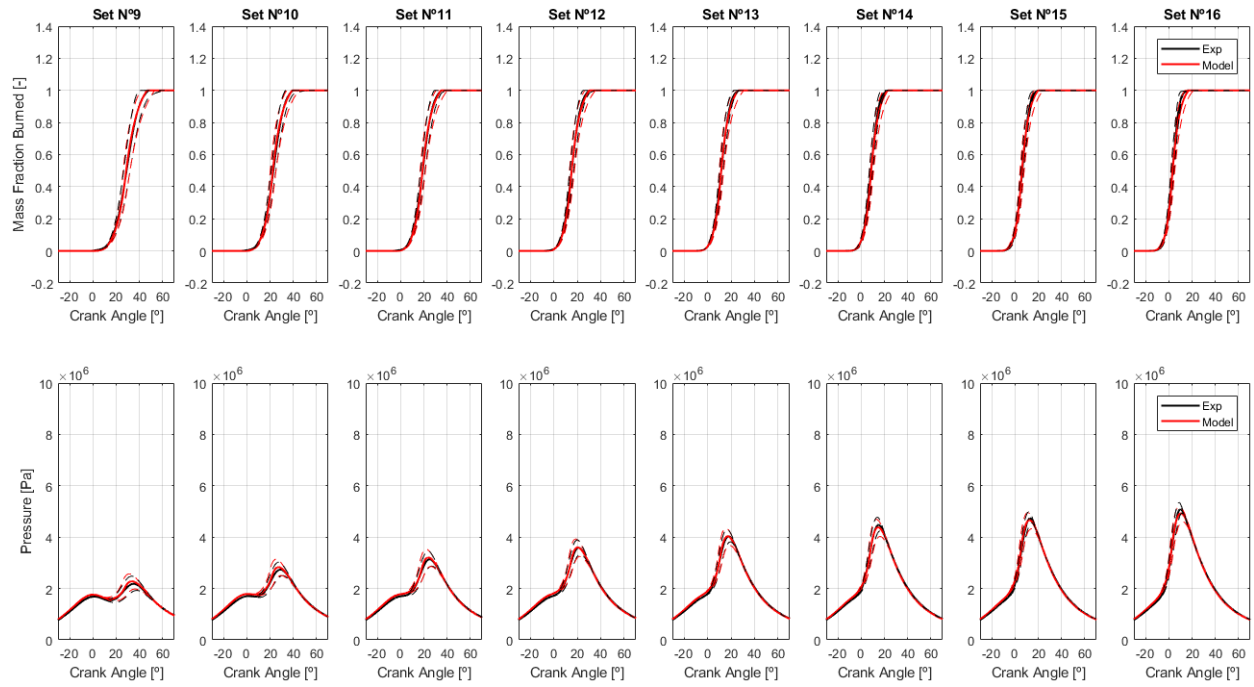
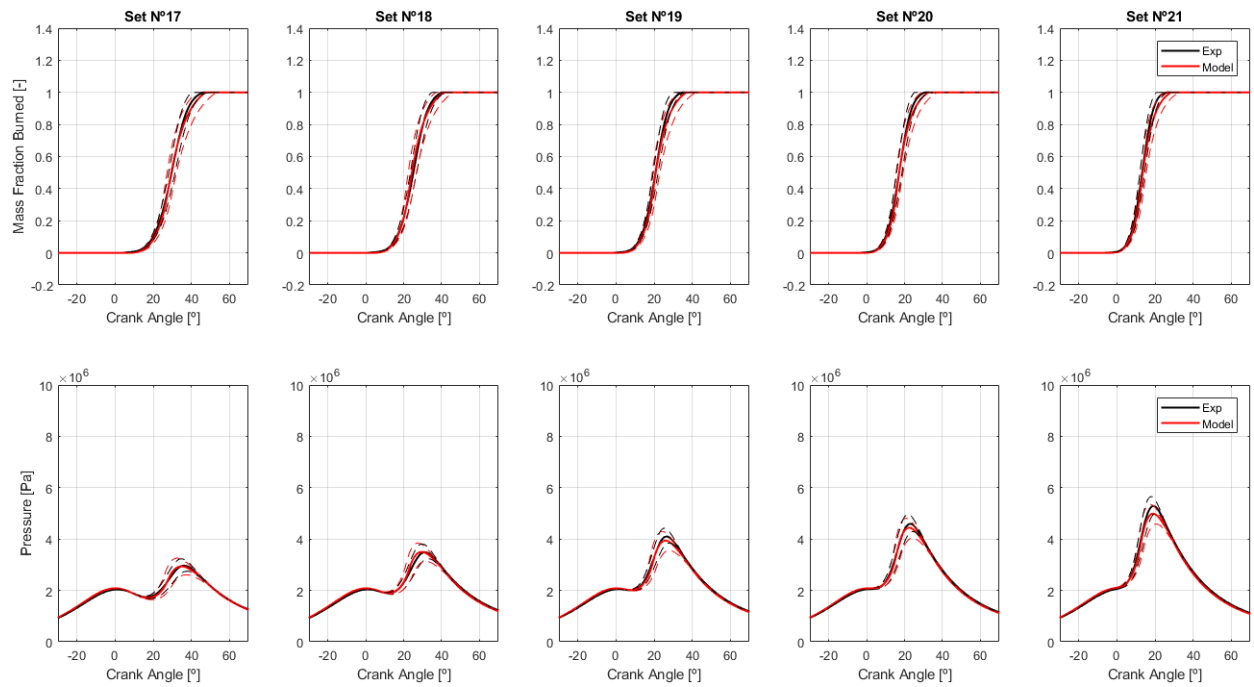FIGURE 93: MFB and in-cylinder pressure with its respective dispersion for high engine speed and medium load level.
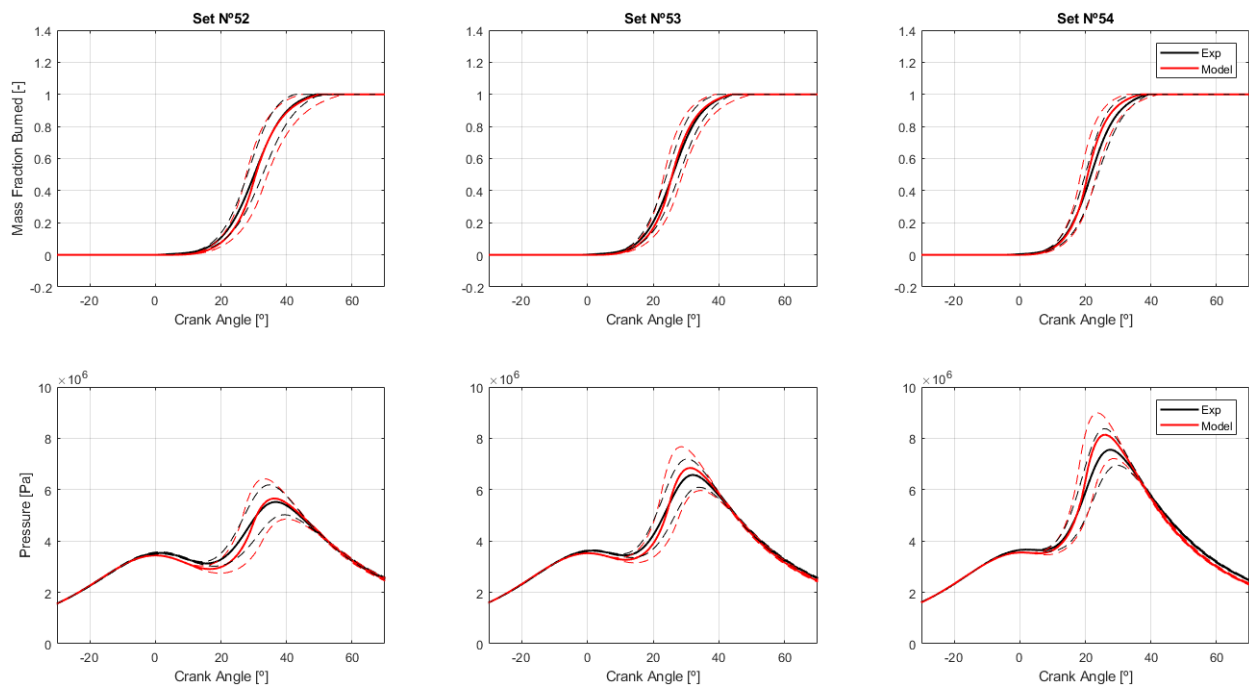
FIGURE 94: MFB and in-cylinder pressure with its respective dispersion for high engine speed and high load level.

Nevertheless, since **this project does not aim to reproduce a cycle-by-cycle behaviour but the behaviour for a representative number of cycles for a concrete operating point**, the maximum errors have not been quantified. **The cumulative relative error of the combustion mean value it is suitable to quantify the error expected from the model** with respect to the experimental data.

Besides, the **results from the validation data can also give information about the accuracy of the model** for in-between values of the operating points used for the calibration and fitting processes. In Figures 95, 96 and 97, these results can be seen which reproduce accurately the experimental data.
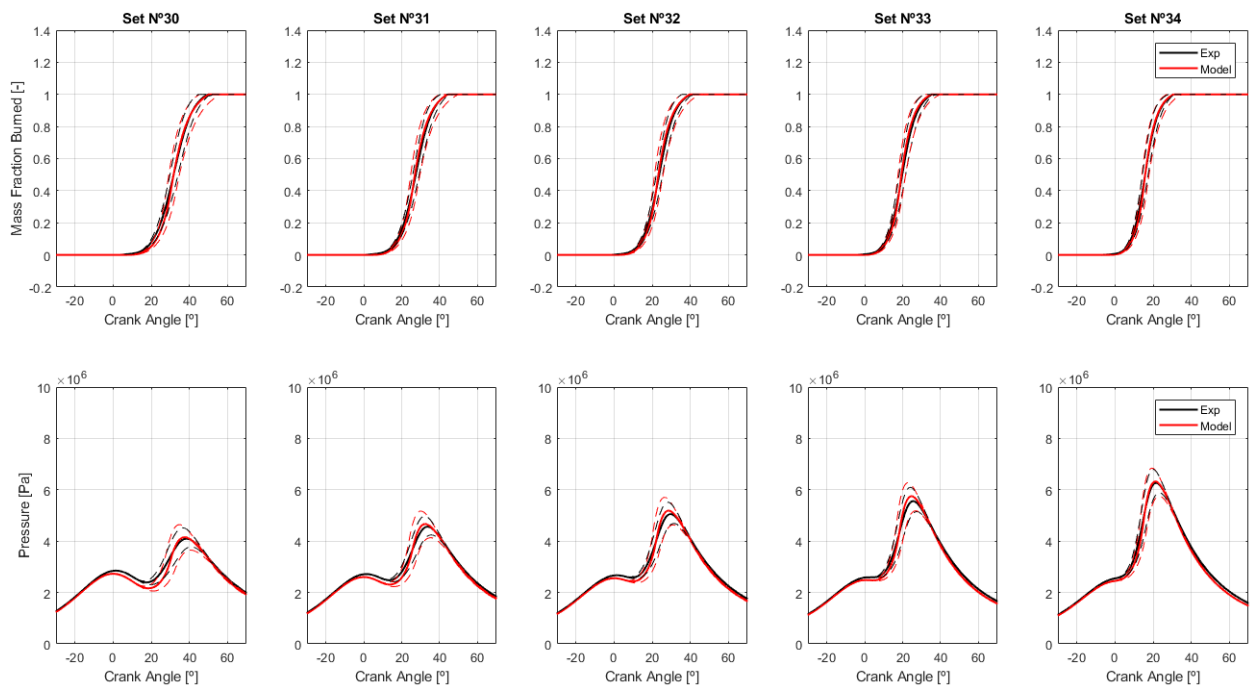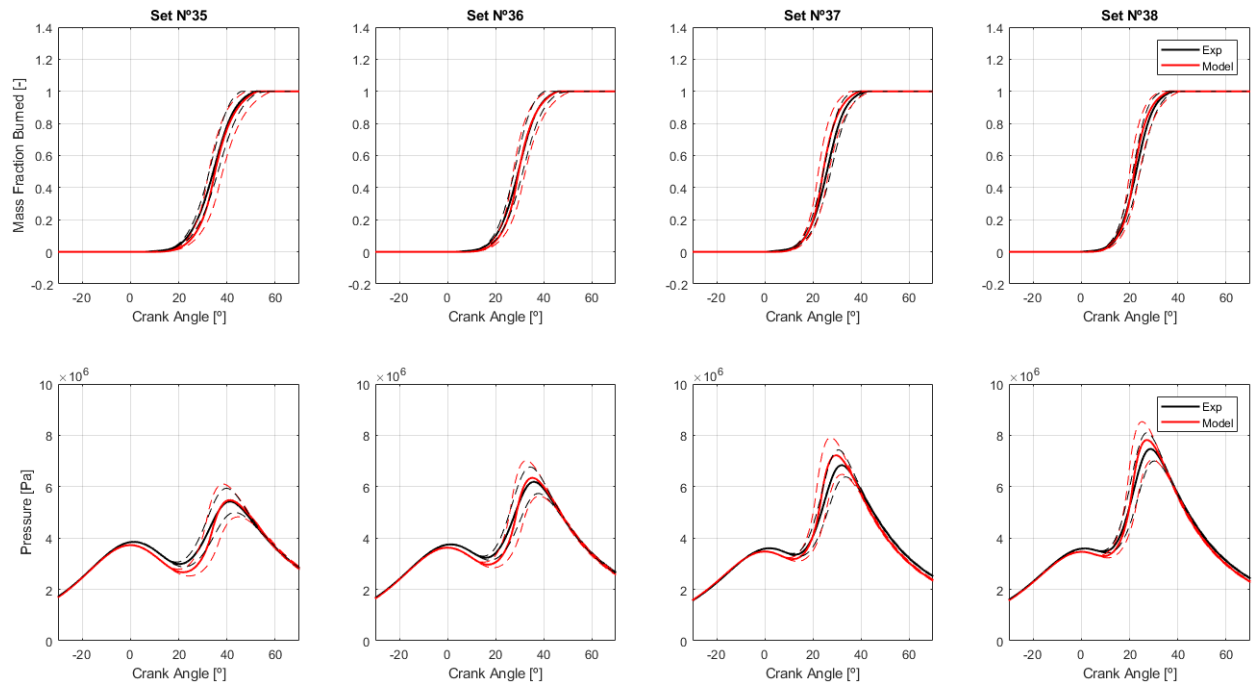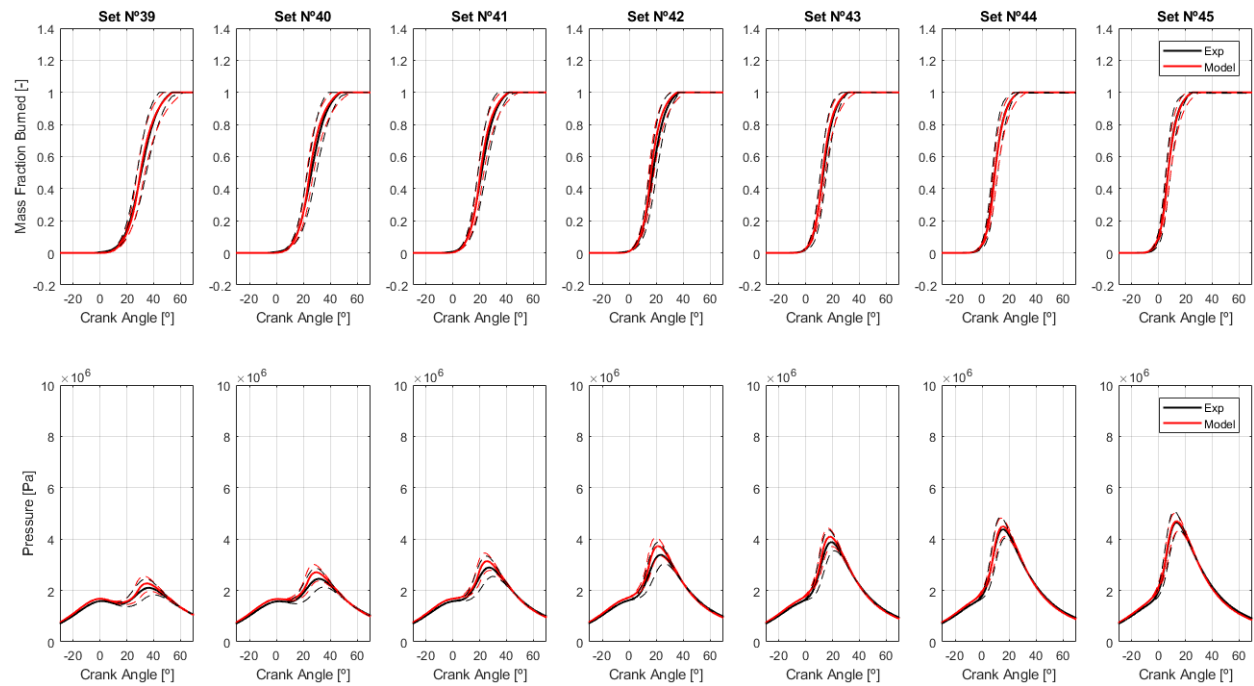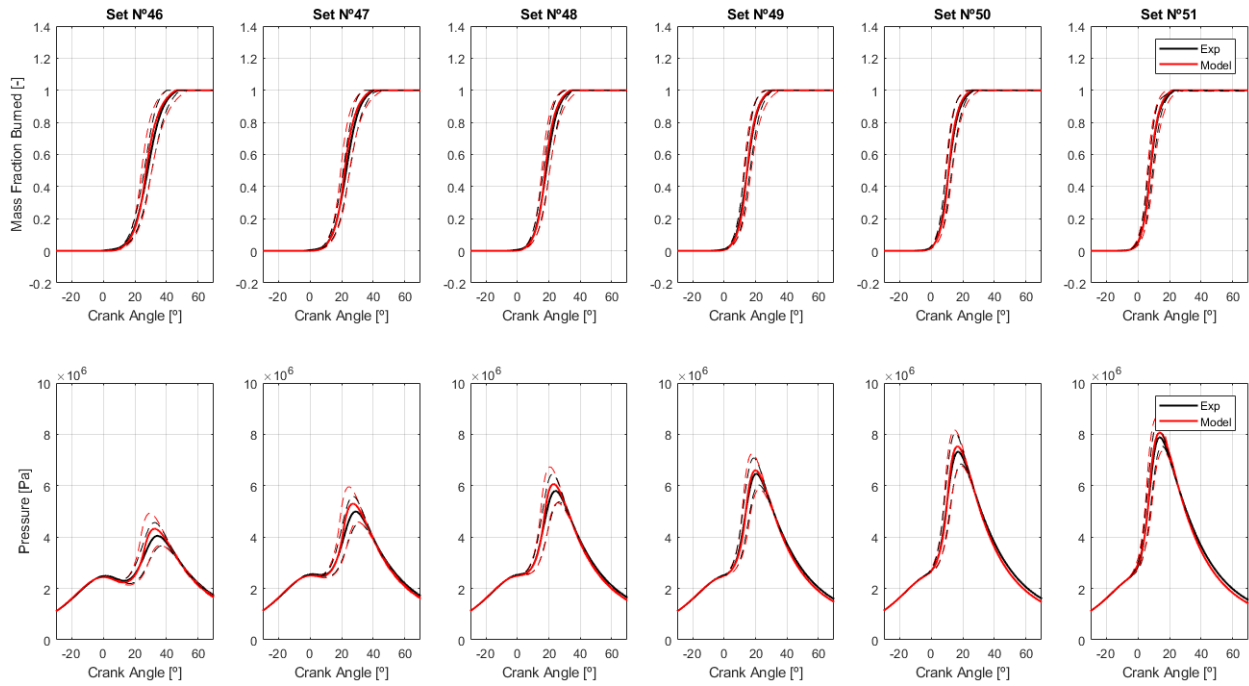

FIGURE 95: MFB and in-cylinder pressure with its respective dispersion for medium engine speed from validation data.

FIGURE 96: MFB and in-cylinder pressure with its respective dispersion for medium-high engine speed from validation data.

FIGURE 97: MFB and in-cylinder pressure with its respective dispersion for high engine speed from validation data.
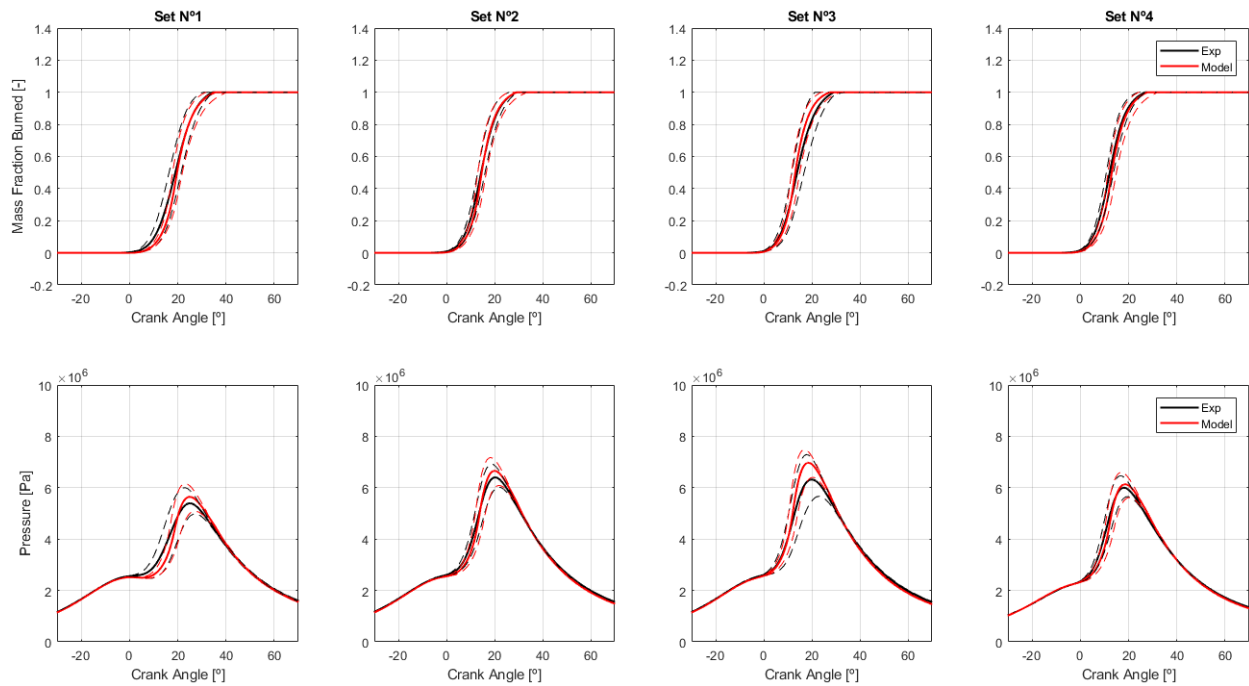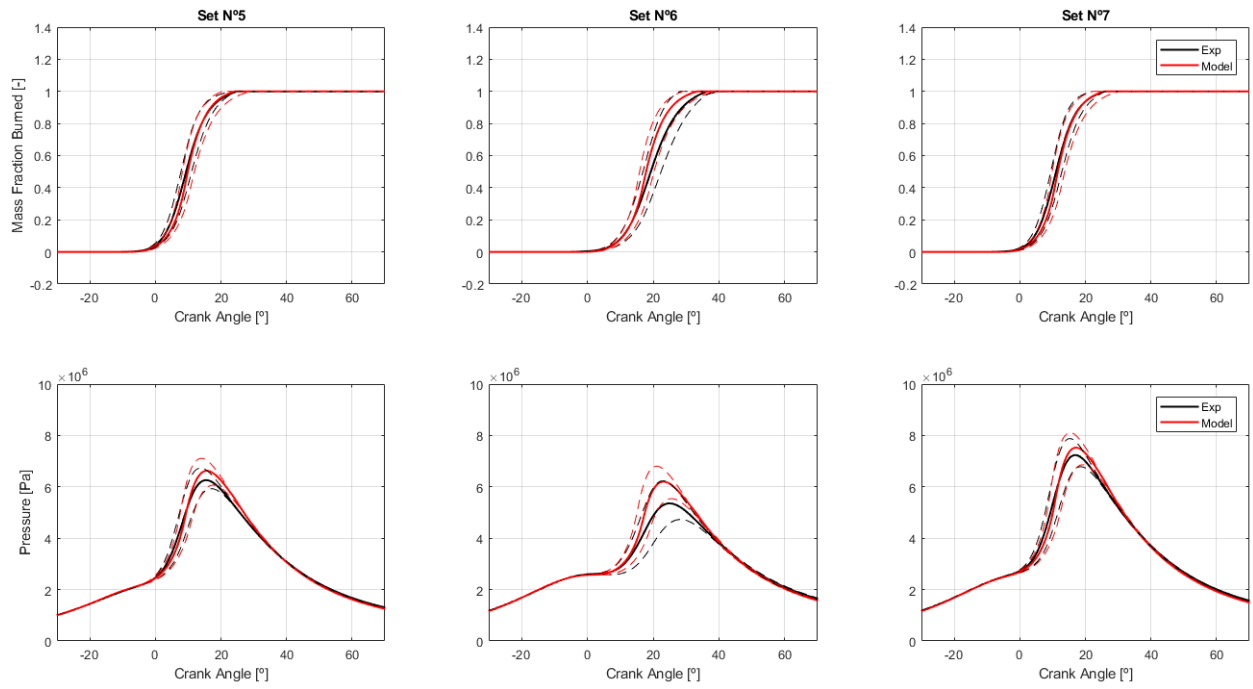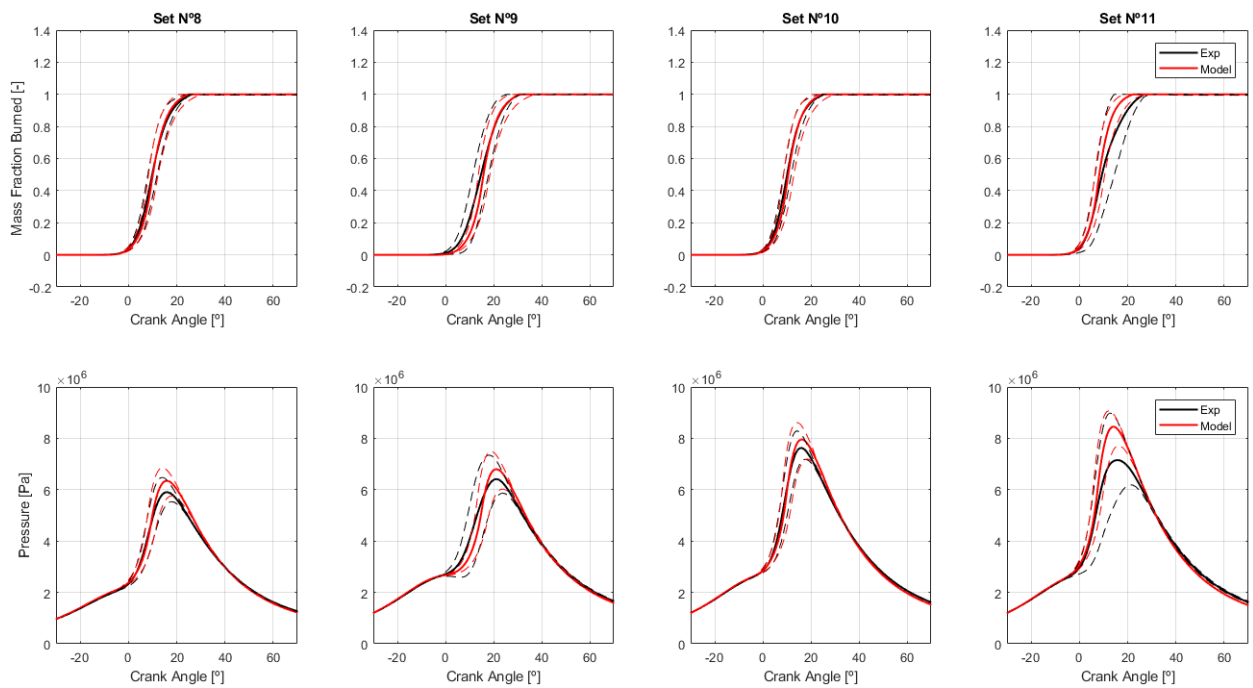
8   Conclusions and Suggested Future Works

Finally, in this chapter all **the processes and computational programs** that make up the project **will be evaluated by both analysing the achievement of the objectives and extracting conclusions from the results obtained**. Besides, **future projects derived from this one will be suggested** and briefly described.

Looking back at the **objectives** settled at the beginning of the project, all of them have been accomplished and reached out with acceptable results:

- First, the **combustion process was analysed from the experimental data extracted** at the test bench. The apparent heat released curve was obtained by applying coherent assumptions to simplify the combustion process.

- **A mean value combustion model was developed and calibrated with the experimental data for a wide operating range**. This model only requires information from a few input parameters (engine speed, intake pressure, spark advance, fuel mass and λ) to return the evolution of both the mass fraction burned and the in-cylinder pressure with a **cumulative relative error lower than 15%**.

- Moreover, for the same data and a representative number of cycles, **the cycle-by-cycle dispersion phenomenon was statistically analysed** due to the turbulent processes involved. Both the mean and standard deviation at each combustion percentage ($CAXX$) were obtained.

- Finally, the **combustion variability was modelled through an error propagation theory**. The variability relative errors at the beginning of the combustion go high due to the variability low values. However, once 10/15% of the combustion is completed, these errors do not exceed 20% or even 10% in some cases. This model was added to the previous **fitted mean value combustion model** in order to fully reproduce the engine combustion process.

All these conclusions merge together in such a way that **both the mean value combustion and the combustion dispersion models are able to reproduce the engine combustion swiftly** (in real operating time) **and accurately** (taking into account reasonable errors) **within a broad operating range**. All codes have been developed in the software Matlab.

Some ideas came up as **future works** during the development of this master thesis. These works may either use this master thesis as a starting point or take it for real applications:

- **Application on combustion optimization** [14]. Accurate combustion models can be very useful when optimizing the engine operating points. Alongside with experimental tests, the combustion model developed in this thesis can contribute to the

ECU mapping in order to optimize the combustion process.

- **Virtual engine for testing performance algorithms**. Testing with real engines is very expensive and only possible in late development stages. These testing tasks can be shifted to earlier phases by using precise simulation engine softwares. The combustion model developed in this project can be complemented with load renewal models (turbocharged flow, exhaust gas recirculation, etc) to give rise to a virtual engine.

- **Improvement of the project with a knock model**. In-cylinder pressure sensors must withstand high temperatures and pressures. Therefore, they are expensive and hard to place and calibrate. However, it would be enough with a knock sensor (an accelerometer placed outside the cylinder) to measure the knock signal. With this signal, the in-cylinder pressure can be predicted. Hence, it is possible to cheapen the test bench equipment and prevent engine detonations.

9   Budget

This chapter is focused on **the study of the cost generated by the realization of the project. Both partial cost and total cost will be shown**, taking into account all the costs from the materials, the employed equipment amortization and the required human resources.

The project budget can be divided in **two different parts. The first one is related to the experimental testing costs and the second one related to the data processing and analysis**.

9.1   Experimental Testing Budget

The experimental testing budget can be split into **three partial costs**: the measure equipment calibration and installation maintenance costs, the conducting tests costs and the employed equipment at the test bench amortization costs.

The **required tests** for this project **were carried out during two months**. Therefore, the **costs associated to conducting the tests** will be calculated for this time gap. Besides, these costs include both the human resources and the required substances for the engine correct functioning such as oil, gasoline, etc. In Table 8 all these costs have been collected.

Concept	Commentary	Units	Unitary Cost	Amount
CMT Direction	2 hours / week	16 h	50.70 €/h	811.20 €
Project Director	1 day / week	64 h	34.60 €/h	2241.40 €
Engineer	3 days / week	192 h	32.00 €/h	6144.00 €
Technician	3 days / week	192 h	22.80 €/h	4377.60 €
Consumables		2 months	750.00 €/month	1500.00 €
			Total:	**15047.20 €**

TABLE 8: Budget associated to conducting the tests at the test bench.

The **installation maintenance** is vital to assure an optimal performance of the equipment and the engine systems. All equipment should be repaired, substituted or fine-tuned before carrying out any test. The estimated costs include the **time and staff required for the installation maintenance and the measure equipment calibration, as well as the materials typically needed in a test bench**. Table 9 gathers all these costs.

Concept	Commentary	Units	Unitary Cost	Amount
Technician	2 days / week	128 h	22.80 €/h	2918.40 €
Consumables		2 months	250.00 €/month	500.00 €
			Total:	**3418.40 €**

TABLE 9: Measure equipment calibration and installation maintenance budget.

In third place, the **employed equipment amortization costs** are shown in Table 10. A full equipment test bench usage causes a big cost. In order to simplify the amortization price of each device, an **annual amortization cost of the full equipment test bench has been estimated in 37200,00 €**.

Concept	Units	Unitary Cost	Amount
Full Equipment Test Bench Amortization	2 months	3100.00 €/h	6200.00 €
		Total:	**6200.00 €**

TABLE 10: Employed equipment amortization budget.

Finally, it has to be taken into account additional costs such as the indirect costs, the industrial profit and the value added tax (VAT). All of them apply to both the maintenance and calibration costs and the conducting testing costs. Besides, the equipment amortization costs has to be added. The total experimental testing budget is shown in Table 11.

Concept	Amount
Calibration and Maintenance Costs	3481.40 €
Conducting Test Costs	15047.20 €
Subtotal 1:	**18465.60 €**
Indirect Costs (10%)	1846.56 €
Industrial Profit (6%)	1107.94 €
Subtotal 2:	**21420.10 €**

VAT (21%)	4498.22 €
Equipment Amortization Costs	6200.00 €
Total Experimental Testing Costs:	**32118.32 €**

Table 11: Total experimental testing budget.

9.2   Data Processing and Analysis Budget

The **data processing and analysis must also be estimated**. These costs are associated to the code development, the later analysis of the obtained results and the computer equipment amortization **made for a 6 months project**.

A code programmed in Matlab has been developed and modified for its computational application to both analyse the experimental data and reproduce them from a model. The **costs associated to the code development** refer to the required human resources (Table 12). The amortization of the computer equipment is presented below.

Concept	Commentary	Units	Unitary Cost	Amount
Engineer	2 days / week	384 h	32.00 €/h	12288.00 €
			Total:	**12288.00 €**

Table 12: Code development budget.

Analogously, to get and analyse the results, only the required human resources will be accounted for. These costs can be seen in Table 13.

Concept	Commentary	Units	Unitary Cost	Amount
CMT Direction	4 hours / week	96 h	50.70 €/h	4867.20 €
Project Director	1 day / week	192 h	34.60 €/h	6643.20 €
Engineer	2 days / week	384 h	32.00 €/h	12288.00 €
			Total:	**23798.40 €**

Table 13: Budget associated to the results obtaining and their analysis.

In third place, the **computer equipment amortization costs** will be computed. These costs account for the MSI computer, the Matlab software and the research facilities usage. The total amortization costs are estimated in Table 14.

Concept	Total Cost	Amortization Period	Amortized Period	Amount
MSI Computer	1000.00 €	5 years	6 months	100.00 €
Matlab Software	2000.00 €	1 year	6 months	1000.00 €
Facilities	60000.00 €	20 years	6 months	1500.00 €
			Total:	**2600.00 €**

Table 14: Computer equipment amortization budget.

Finally, it has to be taken into account additional costs such as the indirect costs, the industrial profit and the value added tax (VAT). All of them apply to both the maintenance and calibration costs and the conducting testing costs. Besides, the equipment amortization costs has to be added. The total experimental testing budget is shown in Table 15.

Concept	Amount
Code Programming Costs	12288.00 €
Results Obtaining and Analysis Costs	23798.40 €
Subtotal 1:	**36086.40 €**
Indirect Costs (10%)	3608.64 €
Industrial Profit (6%)	2165.18 €
Subtotal 2:	**41860.22 €**
VAT (21%)	8790.65 €
Computational Equipment Amortization Costs	2600.00 €
Total Data Processing and Analysis Costs:	**53250.87 €**

Table 15: Total data processing and analysis budget.

9.3 Global Project Budget

In Table 16, the **global project budget** is calculated adding up the experimental testing budget with the data processing and analysis budget.

Concept	Amount
Total Experimental Testing Budget	32118.32 €
Total Data Processing and Analysis Budget	53250.87 €
Global Project Cost:	**85369.19 €**

TABLE 16: Project global budget.

The **global project cost** amounts to **"EIGHTY-FIVE THOUSAND, THREE HUNDRED AND SIXTY-NINE EUROS AND NINETEEN CENTS"**.

References

[1] F. Payri and J. M. Desantes, *Motores de Combustion Interna Alternativos.* Reverté, 2011.

[2] S. Houacine, "A new petrol engine co-developed as part of the collaboration between the Alliance and Daimler," 2018. Available at `https://group.renault.com/en/news/blog-renault/1-3-tce-a-new-petrol-engine-co-developed-as-part-of-the-collaboration-between-the-alliance-and-daimler/`. Visited the 14th April 2019.

[3] CMT, "Engine test cells," 2019. Available at `https://www.cmt.upv.es/EF00.aspx`. Visited the 14th April 2019.

[4] H. Wu, "Study of spark ignition engine combustion model for the analysis of cyclic variation and combustion stability at lean operating conditions," 2015.

[5] R. Mateu Segura *et al.*, *Estudio del impacto de sistemas de admisión en un motor de encendido provocado.* PhD thesis, 2018.

[6] D. Neumann, C. Jörg, N. Peschke, J. Schaub, and T. Schnorbus, "Real-time capable simulation of diesel combustion processes for hil applications," *International Journal of Engine Research*, vol. 19, no. 2, pp. 214–229, 2018.

[7] S. Wang, Q. Zhu, R. Prucka, M. Prucka, and H. Dourra, "Input adaptation for control oriented physics-based si engine combustion models based on cylinder pressure feedback," *SAE International Journal of Engines*, vol. 8, no. 4, 2015.

[8] J. Heywood, *Internal Combustion Engine Fundamentals.* Automotive technology series, McGraw-Hill, 1988.

[9] P. Schiffmann, D. L. Reuss, and V. Sick, "Empirical investigation of spark-ignited flame-initiation cycle-to-cycle variability in a homogeneous charge reciprocating engine," *International Journal of Engine Research*, vol. 19, no. 5, pp. 491–508, 2018.

[10] C. Pera, V. Knop, and J. Reveillon, "Influence of flow and ignition fluctuations on cycle-to-cycle variations in early flame kernel growth," *Proceedings of the Combustion Institute*, vol. 35, no. 3, pp. 2897–2905, 2015.

[11] B. Johansson, "Cycle to cycle variations in s.i. engines-the effects of fluid flow and gas composition in the vicinity of the spark plug on early combustion," *SAE Technical Papers*, 1996.

[12] A. Di Mauro, H. Chen, and V. Sick, "Neural network prediction of cycle-to-cycle power variability in a spark-ignited internal combustion engine," *Proceedings of the Combustion Institute*, vol. 37, no. 4, pp. 4937–4944, 2019.

[13] Q. Zhu, R. Prucka, S. Wang, M. Prucka, and H. Dourra, "Model-based optimal combustion phasing control strategy for spark ignition engines," *SAE International Journal of Engines*, vol. 9, no. 2, 2016.

[14] S. Wang, R. Prucka, Q. Zhu, M. Prucka, and H. Dourra, "A real-time model for spark ignition engine combustion phasing prediction," *SAE International Journal of Engines*, vol. 9, no. 2, 2016.